University of California
Santa Barbara

Ultra-low-loss silicon nitride photonic integrated circuits for highly coherent lasers

A dissertation submitted in partial satisfaction
of the requirements for the degree

Doctor of Philosophy
in
Electrical and Computer Engineering

by

Warren Jin

Committee in charge:

Professor John Bowers, Chair
Professor Nadir Dagli
Professor Jonathan Klamkin
Doctor Paul Morton

March 2022

The Dissertation of Warren Jin is approved.

Professor Nadir Dagli

Professor Jonathan Klamkin

Doctor Paul Morton

Professor John Bowers, Committee Chair

January 2022

Ultra-low-loss silicon nitride photonic integrated circuits for highly coherent lasers

by

Warren Jin

Acknowledgements

First and foremost, I thank my advisor, Professor John Bowers, whose salient advice and patient guidance were key to the completion of this six-and-half-year-long journey. I thank the members of Bowers research group, both past and present, for countless helpful discussions. I thank my collaborators and funding sources at Anello Photonics, CalTech, Keysight, Morton Photonics, Army Research Labs, Radiant Technologies, and DARPA, for generous support. I thank the staff of the UCSB nanofabrication facility, whose vast knowledge and expertise often made the difference between success and failure in the clean-room. I thank the CNSI center for scientific computing whose resources I used to lay the foundation of understanding of this work. Finally, I thank my friends and family for endless encouragement and understanding.

Curriculum Vitæ

Warren Jin

Education

2022	Ph.D. in Electrical and Computer Engineering, University of California, Santa Barbara.
2018	M.S. in Electrical and Computer Engineering, University of California, Santa Barbara.
2012	B.S. in Computer Engineering, Brown University

Selected Journal Publications

B. Li, W. Jin, L. Wu, L. Chang, H. Wang, B. Shen, Z. Yuan, A. Feshali, M. Paniccia, K. J. Vahala, *et. al.*, *Reaching fiber-laser coherence in integrated photonics*, *Optics Letters* **46** (2021), no. 20 5201–5204.

W. Jin, Q.-F. Yang, L. Chang, B. Shen, H. Wang, M. A. Leal, L. Wu, M. Gao, A. Feshali, M. Paniccia, *et. al.*, *Hertz-linewidth semiconductor lasers using CMOS-ready ultra-high-Q microresonators*, *Nature Photonics* **15** (2021), no. 5 346–353.

W. Jin, A. Feshali, M. Paniccia, and J. E. Bowers, *Seamless multi-reticle photonics*, *Optics Letters* **46** (2021), no. 12 2984–2987.

W. Jin, D. D. John, J. F. Bauters, T. Bosch, B. J. Thibeault, and J. E. Bowers, *Deuterated silicon dioxide for heterogeneous integration of ultra-low-loss waveguides*, *Optics Letters* **45** (2020), no. 12 3340–3343.

W. Jin, R. G. Polcawich, P. A. Morton, and J. E. Bowers, *Piezoelectrically tuned silicon nitride ring resonator*, *Optics Express* **26** (2018), no. 3 3174–3187.

Selected Conference Proceedings

W. Jin, Q.-F. Yang, L. Chang, B. Shen, H. Wang, M. A. Leal, L. Wu, M. Gao, A. Feshali, M. Paniccia, *et. al.*, *Hertz-level-linewidth semiconductor laser via injection locking to an ultra-high q silicon nitride microresonator*, in *2021 Conference on Lasers and Electro-Optics (CLEO)*, pp. 1–2, IEEE, 2021.

W. Jin, L. Chang, W. Xie, H. Shu, J. D. Peters, X. Wang, and J. E. Bowers, *Stimulated Brillouin scattering in AlGaAs on insulator waveguides*, in *CLEO: Science and Innovations*, pp. SM4L–7, Optical Society of America, 2020.

W. Jin, E. J. Stanton, N. Volet, R. G. Polcawich, D. Baney, P. A. Morton, and J. E. Bowers, *Piezoelectric tuning of a suspended silicon nitride ring resonator*, in *2017 IEEE Photonics Conference (IPC)*, pp. pp–117, 2017.

Abstract

Ultra-low-loss silicon nitride photonic integrated circuits for highly coherent lasers

by

Warren Jin

The development of integrated photonics has played an important role in the proliferation of high-speed telecommunications, and has the potential to impact numerous applications including precision metrology, sensing, navigation, imaging, and computation. For virtually all such optical systems, optical loss represents a key performance metric. Achieving extremely low optical loss often requires a corresponding increase in the device footprint. This work explores a regime in integrated photonics in which optical loss at parity with the world-record-lowest loss in any integrated platform is achieved, but in a form factor that is planar, fabricated using conventional CMOS processes, and an order of magnitude smaller in footprint. While prior works with comparable loss were been limited by device size and integration limitations to single-device demonstrations, the improved silicon-nitride waveguide platform presented herein enables higher photonic integrated circuit (PIC) complexity than previously explored. These properties are used to create several novel integrated devices, including ultra-high Q and record-high finesse integrated optical resonators, a hybrid-integrated laser with fiber-laser coherence properties, a low-noise microcomb source, a single-mode Raman laser, and a twenty-three meter integrated optical delay line.

While the first part of this thesis thus explores capabilities intrinsic to integrated silicon nitride waveguides, the latter part of the thesis develops novel processing techniques to enable these high performance PICs to interface with other electrical and optical components. A deuterated silicon dioxide thin-film deposition is developed to enable

integration of such silicon nitride PICs with active optical materials, enabling the demonstration of a heterogeneous laser. Piezoelectric tuning of silicon nitride resonators is also explored, which could allow silicon nitride PICs to be reconfigured with dramatically lower power consumption. Finally, a study is presented on extending the benefits and designs of ultra-low loss silicon nitride waveguides to silicon-on-insulator waveguides, which are an attractive platform for many ultra-low loss PICs due to preexisting silicon photonics infrastructure.

Contents

List of Figures

List of Tables

Chapter 1

Introduction

Background

The development of photonic integrated circuits (PICs) began over five decades ago, since pioneering researchers at Bell Laboratories envisioned uniting gain material, modulators, and optical resonators on a single substrate [1, 2]. Compared to the development of electronic integrated circuits however, the development of photonic integrated circuits has progressed at a much slower rate. While integrated photonic parts have long served specialized roles as discrete components in fiber-based systems, such as lithium niobate modulators in fiber-optic communication links [3] or gyroscopes [4], it was not until the 1990's that an appropriate platform emerged for larger scale photonic integration. The availability of both active components (such as lasers and modulators), and passive components (such as splitters, and arrayed waveguide gratings) in a single platform, as well as the growing need for wavelength-division-multiplexing (WDM) in fiber-optic communications systems [5], drove the development of Indium-Phosphide-based photonic integrated circuits [6]. Since the 1990's, the development of InP technology has led to an exponential growth in the scale of photonic integrated circuits, that is, a Moore's Law for Photonics

[6, 7]. However, while InP PICs exceeding thousands devices in a single chip [8] have been demonstrated, any further growth is limited by large size of InP-based components, due to low index contrast available in the platform, and the correspondingly large bend radii [7].

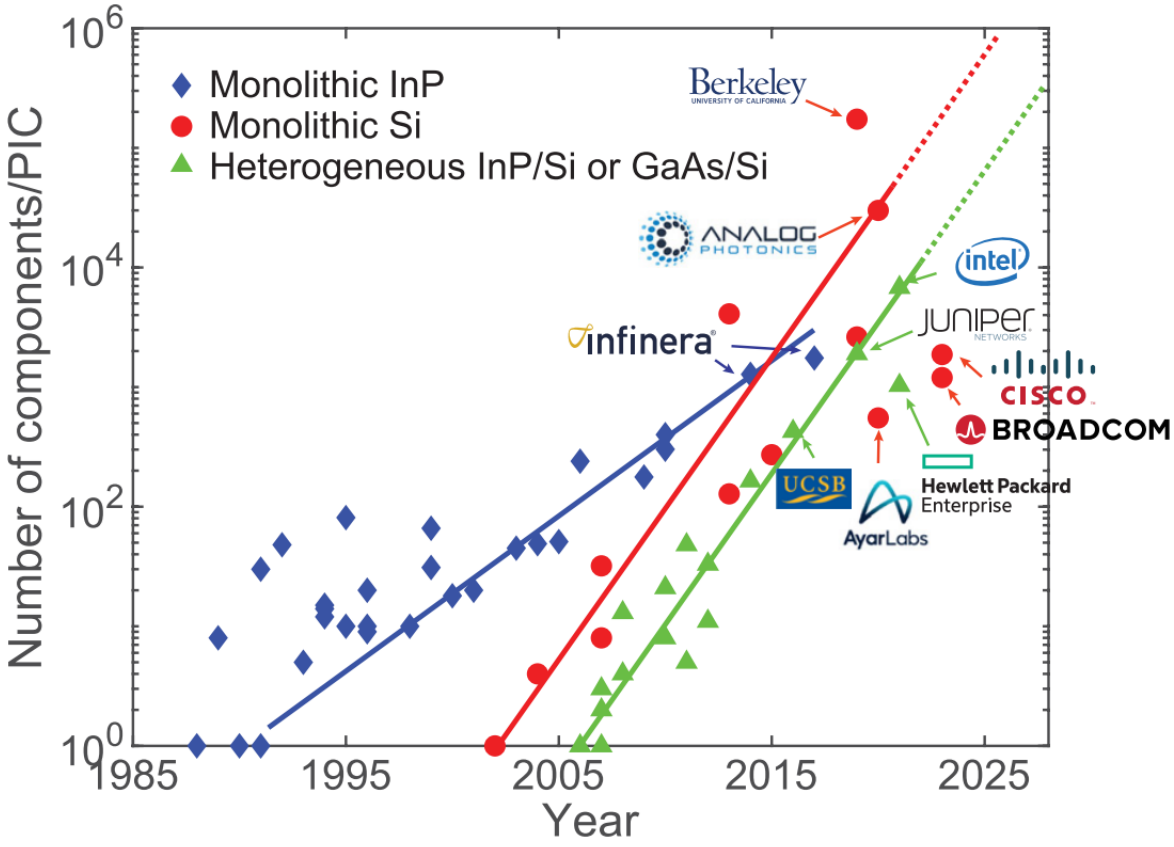

Figure 1.1: **The growth in the number of components in a PIC over time** for three integrated photonic platforms: monolithic indium phosphide, featuring integrated lasers; monolithic silicon photonics, without integrated lasers; and heterogeneous silicon photonics, with integrated lasers. Reproduced from [9].

In the last few decades, a new platform has arisen to overcome the scaling limitations of InP PICs. Driven by demand from telecommunications and datacenter applications, silicon photonics was developed to leverage the advanced fabrication techniques initially developed for the CMOS industry to produce photonic circuits economically and on a large scale [10]. In silicon photonics, silicon nanowires fabricated from silicon-on-insulator

(SOI) wafers feature tight bending radius, low propagation loss, and high yield, enabling PICs exceeding one hundred-thousand elements (Figure 1.1) in size. Additionally, the introduction of III-V materials via wafer bonding [11, 12], known as heterogeneous integration, has enabled integrated lasers to be fabricated alongside modulators, photodetectors, and passive elements to create complete optical systems on a single substrate [9].

The next phase in integrated photonic development may be driven by the rise of ultra-low loss photonic platforms capable of leveraging nonlinear optical phenomena. Such integrated photonic platforms differ from the integrated photonics platforms currently available in InP or CMOS foundries in a few important ways. In contrast to typical silicon photonics processes in which optical components are highly compact and may achieve waveguide losses in dB/cm range, ultra-low loss integrated photonics platforms sacrifice small device footprint in order to reduce propagation loss even further. For example, propagation loss ranging from 1 dB/m [13] to as low as 0.1 dB/m [14] have been demonstrated in silicon nitride waveguides with bend radius ranging from 100 µm to 1 cm. Such low propagation losses enable the fabrication of microresonators with Q factors exceeding 10^7, and have led to demonstrations of nonlinear optical phenomena on integrated photonic chips, such as Brillouin lasing [15], optical parametric oscillation [13], and dissipative Kerr solitons [16, 17]. These nonlinear phenomena help to expand the existing functionalities of integrated photonics as it expands into new application spaces, such as optical atomic clocks [18], LIDAR [19, 20], and optical computation [21].

While promising, ultra-low loss platforms remain at a relatively early stage of research, and must overcome many challenges before becoming available to real-world applications. For example, suspended silica microtoroids [22] and silica wedge resonators [23, 24] feature Q factors exceeding 10^9, however air-cladding, and the use of tapered fibers for evanescent coupling prevents their integration with PICs. Low-loss silicon-nitride-based

photonic circuits [25, 26], generally featuring silica as a cladding material, may achieve high Q factor resonators in the 10^7 to 10^8 range with completely integrated evanescent coupler waveguides, and with greater mechanical stability than air-clad structures, thereby surpassing silica-based platforms in potential for integration, with some sacrifice of Q factor. However, realizing integrated modulators [27, 28], photodetectors[29], and lasers [30, 31] is still much more challenging than in standard silicon photonics, requiring the introduction of other materials to the silicon nitride platform, as the optical phenomena of gain, modulation, and absorption are not endogenous to the silicon nitride and silicon dioxide materials themselves. Recently, lithium niobate on insulator (LNOI) has also arisen as an ultra-low-loss waveguide platform, capable of realizing propagation loss as low as 2.7 dB/m, or equivalently, Q factor up to 10^7 [32], simultaneously with the efficient electro-optic modulation [33], owing to a strong Pockels effect which is endogenous to lithium niobate. However, similarly to the silicon nitride platform, the LNOI platform will also require some form of hybrid or heterogeneous integration [34] to achieve lasers and photodetectors on-chip. Whether ultra-low-loss waveguide platforms can enjoy similar success to silicon photonics in transitioning from research institutes to commercial foundries may depend heavily on how effectively these challenges can be addressed.

Summary

This dissertation is targeted at addressing several challenges to scaling-up ultra-low-loss photonic integrated circuits. Silicon nitride waveguide technology is used as the basis for improving the performance of ultra-low-loss optical waveguides. Chapters 2, 3, 4, and 5 are focused on the platform itself, presenting significant advances in propagation loss, as well as demonstrating novel capabilities of silicon nitride microresonators. The later chapters 6, 7, and 8 focus on overcoming the drawbacks and limitations of this platform

for larger scale photonic integration, such as footprint, process considerations, and power consumption.

Chapter 2 presents the silicon nitride waveguide platform itself. It includes design considerations for selecting the geometry of the silicon nitride waveguide, as well as a the method used for designing the components, such as directional couplers and resonators, presented in the following chapters.

Chapter 3 presents the results of fabrication of high-aspect-ratio silicon nitride waveguides in a commercial CMOS foundry [35]. Q factors exceeding 10^8 are demonstrated in resonators with sub-mm bending radius, and on a foundry platform. This raises the future possibility of ultra-high Q resonators, previously the exclusive domain of specialized academic research, becoming more widely available to real-world applications. The result is particularly notable in that the Q factors achieved approach those previously only attainable by use platforms with significant drawbacks to photonic integration, such as cm-scale bending radius [36, 15], or use of tapered fibers to couple to resonators [22, 23]. Such drawbacks greatly limit the scale of photonic integration to as little as a single device, whereas a sub-mm bending radius and an integrated resonator coupling mechanism enables tens to hundreds of ultra-high Q optical resonators to be linked into higher complexity photonic integrated circuits than previously achieved.

Chapter 4 applies these ultra-high Q factor resonators to the creation of narrow-linewidth lasers, which are an essential component for many potential applications of integrated photonics to metrology and telecommunications. Through self-injection locking of a commercial DFB laser chip to an ultra-high Q factor silicon nitride resonator chip, ultra-narrow linewidth lasing is achieved in a miniature form factor [35]. The chapter culminates in the demonstration of a chip-scale laser with frequency noise spectral density outperforming even that of a commercial, ultra-low-noise fiber laser [37], showing that integrated photonics can even challenge the performance of fiber optics for some

applications.

Chapter 5 leverages the low loss and ultra-high Q factor to explore nonlinear effects. The self-injection-locking configuration in Chapter 4 is shown to also produce a frequency comb laser [35]. The frequency comb is a mode-locked dark soliton, and simultaneously inherits the low frequency noise of the single-mode laser, as well as exhibiting a highly stable repetition rate and extremely low RF phase noise. We also demonstrate that the platform supports other nonlinear phenomena, such as stimulated Brillouin scattering and Raman scattering.

Chapter 6 targets the scalability of large photonic circuits. CMOS technology enabled electronic integrated circuits to simultaneously shrink in size while increasing in both system complexity and performance in accordance with Moore's law. By contrast, in integrated photonics there is a trade-off that must be made between component size and component performance, or equivalently, between bending radius and propagation loss (which is discussed in Chapter 2). Thus, in order to produce increasingly complex integrated photonic circuits at a given level of performance, they must also grow in system footprint. Chapter 6 presents a novel method for stitching waveguides across lithographic reticle boundaries [38]. The technique reduces the insertion loss penalty for crossing a reticle boundary to negligible levels, enabling high-complexity photonic integrated circuits to span multiple reticles.

Chapter 7 turns to the challenge of heterogeneous integration, which will be necessary to incorporate lasers, photodetectors, and modulators onto this this platform. Specifically, since heterogeneous integration by wafer bonding imposes a strict thermal budget on any following process steps, there is a need for low-optical loss top cladding material with low deposition temperature. By contrast, the fabrication process for the ultra-low loss waveguides presented in previous chapters involves thermal annealing at temperatures beyond 1000 °C. Chapter 7 investigates the deposition of deuterated silicon dioxide

by high-density-plasma chemical-vapor deposition (HDPCVD) [39], at temperatures compatible with heterogeneous integration ranging from 100 °C to 250 °C. This material was successfully incorporated into fabrication processes that resulted in a heterogeneously integrated lasers and frequency combs on silicon nitride [30, 40].

Chapter 8 addresses the problem of tuning in silicon nitride waveguides. Thermal tuning is widely used in photonic integrated circuits to align integrated optical components with respect to another, or to reconfigure the system dynamically. However, thermal tuning itself is inefficient, and for larger PICs, the thermal tuning power may greatly exceed the power to operate every other part of the system. The problem is particularly severe in silicon nitride waveguides, which feature an effective thermo optic coefficient an order of magnitude lower than in silicon waveguides, such that thermal phase shifters in silicon nitride waveguides may consume as much as 200 mW to 500 mW [41]. Chapter 8 investigates an alternative approach to tuning, by integrating a piezoelectric material with silicon nitride resonators, to achieve a strain-based tuning mechanism, potentially enabling re-configurable photonic circuits with negligible power consumption.

The appendices to this work focus on parallel efforts in process development to improve on propagation loss and capabilities in silicon-on-insulator (SOI) waveguides, and for which a heterogeneous integration process is already well established [42]. Fabrication process improvements that reduce the propagation loss in silicon waveguides to below 4 dB/m. We also present a design for integrating piezoelectric materials on SOI waveguides to achieve low-power tuning as well as acousto-optic modulation.

Bibliography

[1] S. E. Miller, *Integrated optics: An introduction*, *The Bell System Technical Journal* **48** (1969), no. 7 2059–2069.

[2] P. Tien, R. Ulrich, and R. Martin, *Modes of propagating light waves in thin deposited semiconductor films*, *Applied Physics Letters* **14** (1969), no. 9 291–294.

[3] R. Alferness, *Guided-wave devices for optical communication*, *IEEE Journal of Quantum electronics* **17** (1981), no. 6 946–959.

[4] H. C. Lefevre, *The fiber-optic gyroscope*. Artech house, 2014.

[5] G. P. Agrawal, *Fiber-optic communication systems*, vol. 222. John Wiley & Sons, 2012.

[6] M. Smit, J. Van der Tol, and M. Hill, *Moore's law in photonics*, *Laser & Photonics Reviews* **6** (2012), no. 1 1–13.

[7] M. Smit, K. Williams, and J. van der Tol, *Past, present, and future of InP-based photonic integration*, *APL Photonics* **4** (2019), no. 5 050901.

[8] J. Summers, T. Vallaitis, P. Evans, M. Ziari, P. Studenkov, M. Fisher, J. Sena, A. James, S. Corzine, D. Pavinski, *et. al.*, *Monolithic InP-based coherent transmitter photonic integrated circuit with 2.25 tbit/s capacity*, *Electronics Letters* **50** (2014), no. 16 1150–1152.

[9] N. Margalit, C. Xiang, S. M. Bowers, A. Bjorlin, R. Blum, and J. E. Bowers, *Perspective on the future of silicon photonics and electronics*, *Applied Physics Letters* **118** (2021), no. 22 220501.

[10] A. Rickman, *The commercialization of silicon photonics*, *Nature Photonics* **8** (2014), no. 8 579–582.

[11] A. W. Fang, H. Park, O. Cohen, R. Jones, M. J. Paniccia, and J. E. Bowers, *Electrically pumped hybrid AlGaInAs-silicon evanescent laser*, *Optics Express* **14** (2006), no. 20 9203–9210.

[12] A. Malik, C. Xiang, L. Chang, W. Jin, J. Guo, M. Tran, and J. Bowers, *Low noise, tunable silicon photonic lasers*, *Applied Physics Reviews* **8** (2021), no. 3 031306.

[13] X. Ji, F. A. Barbosa, S. P. Roberts, A. Dutt, J. Cardenas, Y. Okawachi, A. Bryant, A. L. Gaeta, and M. Lipson, *Ultra-low-loss on-chip resonators with sub-milliwatt parametric oscillation threshold*, *Optica* **4** (2017), no. 6 619–624.

[14] J. F. Bauters, M. J. Heck, D. D. John, J. S. Barton, C. M. Bruinink, A. Leinse, R. G. Heideman, D. J. Blumenthal, and J. E. Bowers, *Planar waveguides with less than 0.1 dB/m propagation loss fabricated with wafer bonding*, *Optics Express* **19** (2011), no. 24 24090–24101.

[15] S. Gundavarapu, G. M. Brodnik, M. Puckett, T. Huffman, D. Bose, R. Behunin, J. Wu, T. Qiu, C. Pinho, N. Chauhan, *et. al.*, *Sub-Hertz fundamental linewidth photonic integrated Brillouin laser*, *Nature Photonics* **13** (2019), no. 1 60–67.

[16] T. Herr, V. Brasch, J. D. Jost, C. Y. Wang, N. M. Kondratiev, M. L. Gorodetsky, and T. J. Kippenberg, *Temporal solitons in optical microresonators*, *Nature Photonics* **8** (2014), no. 2 145–152.

[17] A. L. Gaeta, M. Lipson, and T. J. Kippenberg, *Photonic-chip-based frequency combs*, *nature photonics* **13** (2019), no. 3 158–169.

[18] Z. L. Newman, V. Maurice, T. Drake, J. R. Stone, T. C. Briles, D. T. Spencer, C. Fredrick, Q. Li, D. Westly, B. R. Ilic, *et. al.*, *Architecture for the photonic integration of an optical atomic clock*, *Optica* **6** (2019), no. 5 680–685.

[19] J. Riemensberger, A. Lukashchuk, M. Karpov, W. Weng, E. Lucas, J. Liu, and T. J. Kippenberg, *Massively parallel coherent laser ranging using a soliton microcomb*, *Nature* **581** (2020), no. 7807 164–170.

[20] J. Hulme, J. Doylend, M. Heck, J. Peters, M. Davenport, J. Bovington, L. Coldren, and J. Bowers, *Fully integrated hybrid silicon two dimensional beam scanner*, *Optics express* **23** (2015), no. 5 5861–5874.

[21] J. Feldmann, N. Youngblood, M. Karpov, H. Gehring, X. Li, M. Stappers, M. Le Gallo, X. Fu, A. Lukashchuk, A. S. Raja, J. Liu, C. Wright, A. Sebastian, T. Kippenberg, W. Pernice, and H. Bhaskaran, *Parallel convolutional processing using an integrated photonic tensor core*, *Nature* **589** (2021), no. 7840 52–58.

[22] T. Kippenberg, S. Spillane, and K. Vahala, *Demonstration of ultra-high-Q small mode volume toroid microcavities on a chip*, *Applied Physics Letters* **85** (2004), no. 25 6113–6115.

[23] H. Lee, T. Chen, J. Li, K. Y. Yang, S. Jeon, O. Painter, and K. J. Vahala, *Chemically etched ultrahigh-Q wedge-resonator on a silicon chip*, *Nature Photonics* **6** (2012), no. 6 369–373.

[24] L. Wu, H. Wang, Q. Yang, Q.-x. Ji, B. Shen, C. Bao, M. Gao, and K. Vahala, *Greater than one billion Q factor for on-chip microresonators*, *Optics Letters* **45** (2020), no. 18 5129–5131.

[25] D. J. Blumenthal, R. Heideman, D. Geuzebroek, A. Leinse, and C. Roeloffzen, *Silicon nitride in silicon photonics*, *Proceedings of the IEEE* **106** (2018), no. 12 2209–2231.

[26] J. Liu, G. Huang, R. N. Wang, J. He, A. S. Raja, T. Liu, N. J. Engelsen, and T. J. Kippenberg, *High-yield, wafer-scale fabrication of ultralow-loss, dispersion-engineered silicon nitride photonic circuits*, *Nature communications* **12** (2021), no. 1 1–9.

[27] J. Liu, H. Tian, E. Lucas, A. S. Raja, G. Lihachev, R. N. Wang, J. He, T. Liu, M. H. Anderson, W. Weng, *et. al.*, *Monolithic piezoelectric control of soliton microcombs*, *Nature* **583** (2020), no. 7816 385–390.

[28] K. Alexander, J. P. George, J. Verbist, K. Neyts, B. Kuyken, D. Van Thourhout, and J. Beeckman, *Nanophotonic Pockels modulators on a silicon nitride platform*, *Nature communications* **9** (2018), no. 1 1–6.

[29] M. Piels, J. F. Bauters, M. L. Davenport, M. J. Heck, and J. E. Bowers, *Low-loss silicon nitride AWG demultiplexer heterogeneously integrated with hybrid III–V/silicon photodetectors*, *Journal of lightwave technology* **32** (2013), no. 4 817–823.

[30] C. Xiang, W. Jin, J. Guo, J. D. Peters, M. Kennedy, J. Selvidge, P. A. Morton, and J. E. Bowers, *Narrow-linewidth III-V/Si/Si$_3$N$_4$ laser using multilayer heterogeneous integration*, *Optica* **7** (2020), no. 1 20–21.

[31] H. Park, C. Zhang, M. A. Tran, and T. Komljenovic, *Heterogeneous silicon nitride photonics*, *Optica* **7** (2020), no. 4 336–337.

[32] M. Zhang, C. Wang, R. Cheng, A. Shams-Ansari, and M. Lončar, *Monolithic ultra-high-Q lithium niobate microring resonator*, *Optica* **4** (2017), no. 12 1536–1537.

[33] C. Wang, M. Zhang, X. Chen, M. Bertrand, A. Shams-Ansari, S. Chandrasekhar, P. Winzer, and M. Lončar, *Integrated lithium niobate electro-optic modulators operating at CMOS-compatible voltages*, *Nature* **562** (2018), no. 7725 101–104.

[34] A. Shams-Ansari, D. Renaud, R. Cheng, L. Shao, L. He, D. Zhu, M. Yu, H. R. Grant, L. Johansson, M. Zhang, *et. al.*, *Electrically-pumped high-power laser*

transmitter integrated on thin-film lithium niobate, *arXiv preprint arXiv:2111.08473* (2021).

[35] W. Jin, Q.-F. Yang, L. Chang, B. Shen, H. Wang, M. A. Leal, L. Wu, M. Gao, A. Feshali, M. Paniccia, *et. al.*, *Hertz-linewidth semiconductor lasers using CMOS-ready ultra-high-Q microresonators*, *Nature Photonics* **15** (2021), no. 5 346–353.

[36] D. T. Spencer, J. F. Bauters, M. J. Heck, and J. E. Bowers, *Integrated waveguide coupled Si_3N_4 resonators in the ultrahigh-Q regime*, *Optica* **1** (2014), no. 3 153–157.

[37] B. Li, W. Jin, L. Wu, L. Chang, H. Wang, B. Shen, Z. Yuan, A. Feshali, M. Paniccia, K. J. Vahala, *et. al.*, *Reaching fiber-laser coherence in integrated photonics*, *Optics Letters* **46** (2021), no. 20 5201–5204.

[38] W. Jin, A. Feshali, M. Paniccia, and J. E. Bowers, *Seamless multi-reticle photonics*, *Optics Letters* **46** (2021), no. 12 2984–2987.

[39] W. Jin, D. D. John, J. F. Bauters, T. Bosch, B. J. Thibeault, and J. E. Bowers, *Deuterated silicon dioxide for heterogeneous integration of ultra-low-loss waveguides*, *Optics Letters* **45** (2020), no. 12 3340–3343.

[40] C. Xiang, J. Liu, J. Guo, L. Chang, R. N. Wang, W. Weng, J. Peters, W. Xie, Z. Zhang, J. Riemensberger, J. Selvidge, T. J. Kippenberg, and J. E. Bowers, *Laser soliton microcombs heterogeneously integrated on silicon*, *Science* **373** (2021), no. 6550 99–103, [https://science.sciencemag.org/content/373/6550/99.full.pdf].

[41] C. G. Roeloffzen, L. Zhuang, C. Taddei, A. Leinse, R. G. Heideman, P. W. van Dijk, R. M. Oldenbeuving, D. A. Marpaung, M. Burla, and K.-J. Boller, *Silicon nitride microwave photonic circuits*, *Optics Express* **21** (2013), no. 19 22937–22961.

[42] M. A. Tran, D. Huang, and J. E. Bowers, *Tutorial on narrow linewidth tunable semiconductor lasers using Si/III-V heterogeneous integration*, *APL photonics* **4** (2019), no. 11 111101.

Chapter 2

Ultra-low loss silicon nitride platform

This chapter introduces the ultra-low-loss silicon nitride platform which forms the basis of this work. The design considerations for the choice of waveguide geometry are discussed. Subsequently, models and practical considerations for the design of efficient directional couplers are also presented.

2.1 Silicon nitride waveguide design

Waveguides of silicon nitride core and silicon dioxide cladding have become an important technology for creating ultra-low-loss waveguides. Mode profiles of a few selected geometries are shown in Figure 2.1. Using standard CMOS processes, these waveguides may be fabricated at the wafer scale on silicon substrates as large as 300 mm in diameter [1, 2, 3, 4]. Thanks to the high quality of silicon dioxide and silicon nitride available using CMOS processes, the propagation loss is generally dominated by scattering losses, rather than material absorption. The primary component of scattering loss is generally sidewall

roughness of the silicon nitride core, as the top-surface and bottom-surface roughness of the silicon nitride layer are generally well below 1 nm owing to high quality CMP processes and conformal deposition techniques [5, 6]. By contrast, roughness – originating from the line-edge roughness of the lithography process – is transferred to the waveguide sidewall by the dry-etching process, and is generally over 1 nm in magnitude [7, 8]. This sidewall roughness amounts to a perturbation to the waveguide geometry as light propagates along the waveguide, resulting in light being scattered into the the continuum of unguided modes [9], with scattering loss magnitude which is ultimately determined by the overlap between the guided optical mode and the waveguide sidewall. The choice of the thickness of the silicon nitride layer is thus critical, as it determines the degree to which the optical mode is influenced by sidewall roughness. Accordingly, several types of silicon nitride waveguides have emerged to serve various purposes.

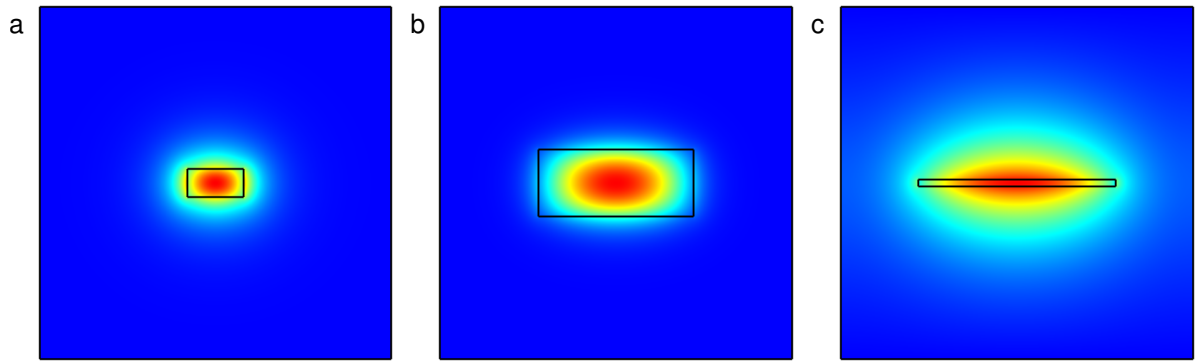

Figure 2.1: **Transverse-electric (TE) cross-sectional mode profiles** of silicon nitride waveguides featuring (a) 400 nm thickness and 800 nm width, (b) 950 nm thickness and 2200 nm width, and (c) 100nm thickness at 2800 nm width.

High-modal-confinement waveguides with thickness of up to 400 nm (shown in Figure 2.1a) have become commonplace in many commercial silicon photonics foundries. These waveguides feature a single transverse electric (TE) mode, a single transverse magnetic (TM) mode, bending radii as low as 20 µm, and propagation losses as low as 20 dB/m. They are frequently used for low-loss routing, or for coupling to fiber at the

edge of a PIC.

For applications in nonlinear optics, there is often a requirement that the waveguide exhibit anomalous group velocity dispersion, such as for bright soliton formation or supercontinuum generation via the Kerr effect [10, 11]. Anomalous dispersion requires a much larger waveguide thickness, generally above 700 nm (Figure 2.1b). These waveguides feature propagation losses as low as 1 dB/m [4, 5], as the optical mode within the larger core exhibits a lower overlap with the waveguide sidewall, as compared to the waveguide shown in Figure 2.1a. However, these waveguides support higher-order transverse modes. While bending radiii as low as 20 µm are possible in this waveguide core geometry as well, care must be taken in routing between straight and bending waveguides to minimize modal cross-talk [12].

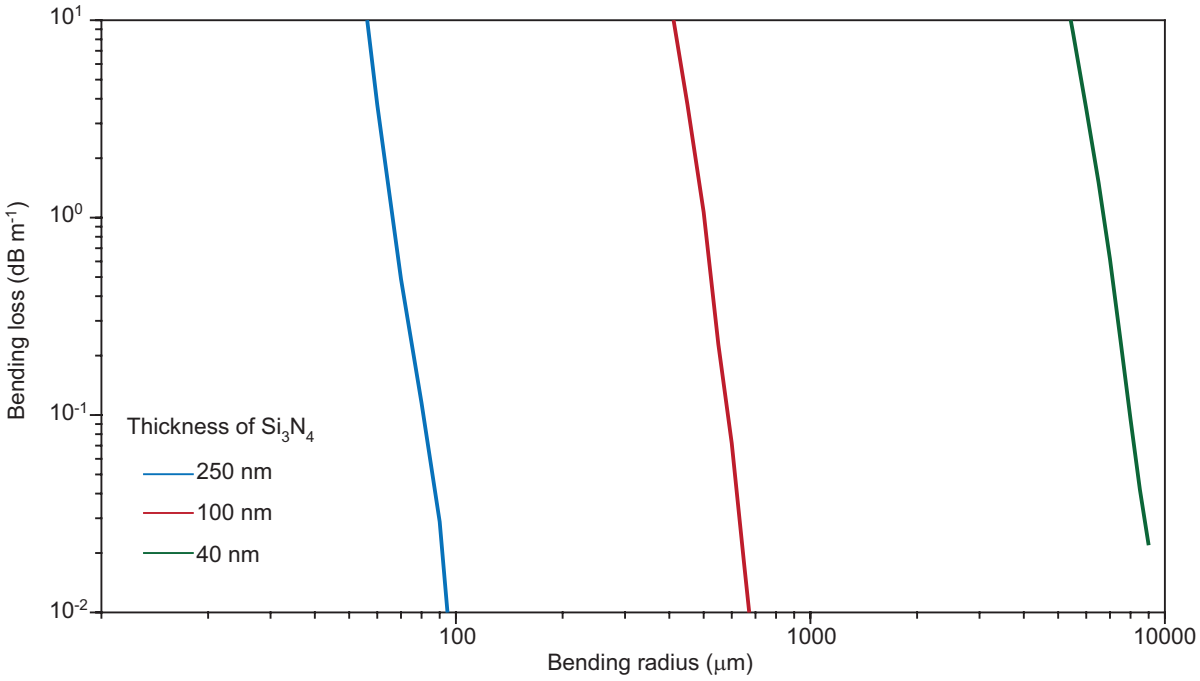

Figure 2.2: **Simulated bending loss** for the fundamental TE mode at $\lambda = 1550\,\text{nm}$ for silicon nitride waveguides of 250 nm, 100 nm, and 40 nm thickness, and 1.4 µm, 2.8 µm, and 5.6 µm width, respectively. The waveguide widths are chosen to support single-mode propagation within the telecommunications C-band. Reproduced from [13].

For applications seeking even lower waveguide loss, the thickness of the silicon nitride layer is a compromise between loss and the acceptable device footprint. Silicon nitride waveguides of thickness 100 nm or below (Figure 2.1c) form high-aspect ratio, low-confinement silicon nitride waveguides with propagation loss potentially below 0.1 dB/m [8, 7]. In this regime, the optical mode resides primarily within the silicon dioxide cladding. For decreasing silicon nitride thickness, the optical mode is increasingly 'squeezed out' of the core, and the mode volume grows [7] while the sidewall height shrinks. As a result, the sidewall overlap with the optical mode decreases, and the sidewall scattering loss is also reduced. However, as the optical mode grows, the minimum feasible bend radius also grows. The dependence of bending loss on bending radius for single-mode waveguide geometries at a selected silicon nitride thickness is shown in Figure 2.2, demonstrating that the selection of thinner waveguide cores to achieve a lower propagation loss comes at the expense of increasing bending radius and thus device footprint. Indeed, a core thickness of 40 nm necessitates a minimum bending radius approaching 1 cm, such that a standard deep-UV lithography reticle of approximately 2 cm by 2 cm dimension may hardly accommodate a single device. For the remainder of this chapter, we will consider silicon nitride waveguides with approximately 100 nm thickness, which enable extremely low propagation loss and bending radius below 1 mm.

A cross-sectional diagram of the waveguide geometry considered is shown in Figure 2.3. The waveguide fabrication follows the general process as detailed in [7, 13]. First, a silicon dioxide layer is formed by thermal oxidation of a silicon wafer with thickness 14.5 µm. A 100 nm layer of silicon nitride is deposited via low-pressure chemical vapor deposition (LPCVD), patterned using deep UV (DUV) stepper lithography, and dry-etched to form the waveguide core. Then, LPCVD silicon dioxide is deposited from a tetra-ethyl ortho-silicate (TEOS) precursor and annealed at 1150 °C to reach a total top cladding thickness of 2 µm and a total annealing time exceeding 20 hours.

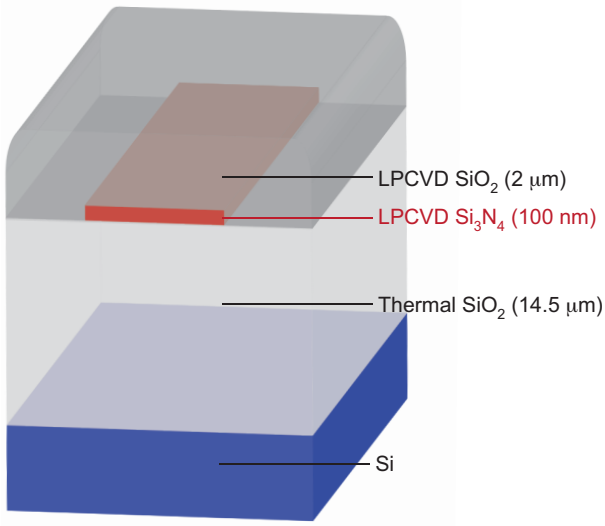

Figure 2.3: **Cross-sectional diagram of the ultra-low-loss waveguide** consisting of silicon nitride as the core material, silica as the cladding and silicon as the substrate (not to scale). Reproduced from [13].

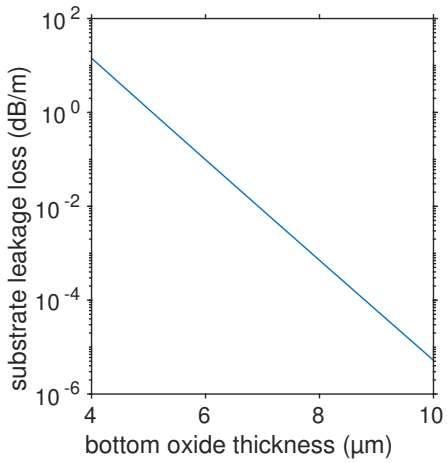

Figure 2.4: **Loss due to radiation into the silicon substrate** as a function of bottom silicon dioxide cladding thickness for a 100 nm thick, 2800 nm wide silicon nitride waveguide with 2 µm top cladding, simulated at 1550 nm wavelength.

The choice of lower cladding thickness is constrained by leakage into the silicon substrate. The dependence of substrate leakage on lower silicon dioxide cladding thickness is shown in Figure 2.4 for a 100 nm thick silicon waveguide at single-mode width of 2800 nm. A lower cladding thickness of 8 µm or greater is sufficient to guarantee a substrate leakage below 0.001 dB/m in this geometry. We select 14.5 µm lower cladding thickness to ensure negligible substrate leakage for a wide range of silicon nitride thickness and waveguide width, and over a wide range of operating wavelengths.

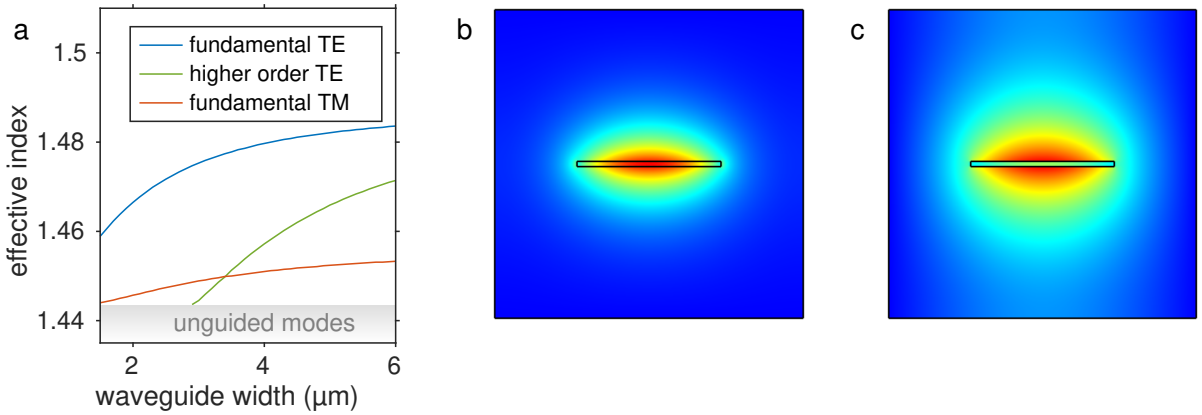

Figure 2.5: **Single mode condition.** (a) Plot of modal index as a function of waveguide width for a 100 nm thick silicon nitride waveguide, simulated at 1550 nm. Below 3 µm waveguide width, only a single TE-polarized mode, and a single TM-polarized mode are supported. The continuum of unguided optical modes within the silicon dioxide cladding are indicated by the shaded region. (b) Electric field magnitude for the fundamental TE mode at 2.8 µm width. (c) Electric field magnitude for the fundamental TM mode at 2.8 µm width.

For a given core material thickness, the single-mode condition can be determined by simulating the effective indices of the guided modes over a range of waveguide widths. Such a study is shown in Figure 2.5a, demonstrating that the higher-order TE-polarized mode is cut off for width below 3 µm. A choice of 2.8 µm width ensures that the waveguide remains single mode over a wide range of operating wavelength, as well as thickness deviations (to account for fabrication process tolerances). The modal profiles of the guided TE and TM modes at this width are shown if Figure 2.5b,c. However, while both

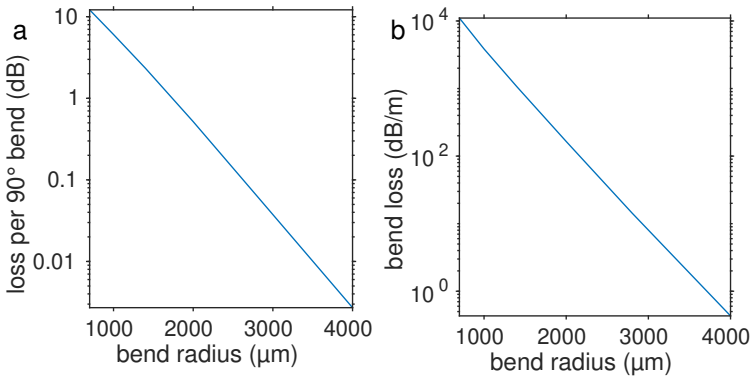

Figure 2.6: **Bending loss modeling.** (a) loss per bend and (b) loss per meter, of the fundamental TM mode for a 100 nm thick, 2.8 µm wide waveguide as a function of bend radius at 1550 nm wavelength.

TE and TM polarizations may be guided in a straight waveguide, the bending waveguide exhibits significant polarization-dependent loss, as shown in Figure 2.6. For bending below 1 mm, the bending loss of the TM mode approaches 10 dB per 90° bend, and may be used as an on-chip polarizer [14]. Due to the high propagation loss of the fundamental TM mode around bends, a waveguide featuring 2.8 µm width and bends at 1 mm bend radius or below may be considered to support only a single mode.

2.2 Resonator modeling

Optical resonators confine light to small volumes by resonant recirculation. Low optical losses provide a dual benefit to these devices. First, by dramatically enhancing light intensity within the resonator, low losses make it possible to access nonlinear effects. Secondly, low losses enable to resonators to exhibit narrow resonant bandwidths, enabling high-quality optical filters [15]. These properties of resonators make them a fundamental building block in many optical systems.

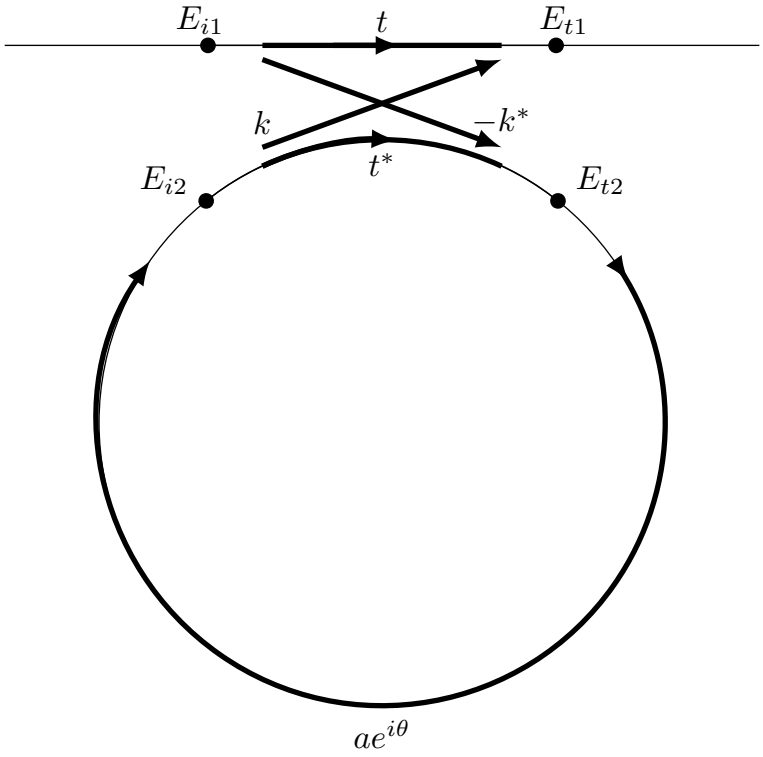

Figure 2.7: **Generic representation of a ring resonator** coupled to a single waveguide, based on [16, 17, 18].

2.2.1 Block element model

A simple way to form a resonator is to route a waveguide in a closed loop, allowing the light to recirculate. In order to excite the resonator, another waveguide, known as the bus waveguide, is brought into close spatial proximity, allowing light to couple across the gap. This basic configuration is depicted in Figure 2.7, and is based on the model presented in [16, 17, 18]. This system can be modeled by a linear system of equations in terms of the complex electric fields within the resonator and bus waveguides. The coupling region may be described by the matrix equation [16]

$$\begin{pmatrix} E_{t1} \\ E_{t2} \end{pmatrix} = \begin{pmatrix} t & k \\ -k^* & t^* \end{pmatrix} \begin{pmatrix} E_{i1} \\ E_{i2} \end{pmatrix} \tag{2.1}$$

Assuming that the coupler is lossless, the coupling matrix is unitary, and the coupling coefficients through and across the coupling region may be written in terms of one another.

$$|k^2| + |t^2| = 1 \tag{2.2}$$

Finally, the self-coupling of the resonator may be described by the following equation, where the phase accumulated propagating around the resonator waveguide is represented by θ, and the attenuation of the resonator waveguide per round-trip is represented by a.

$$E_{i2} = a \cdot e^{i\theta} E_{t2} \tag{2.3}$$

By normalizing the input field, $E_{i1} = 1$, then the system of equations may be solved for the field within the resonator, as well as the output power [18].

$$E_{t2} = \frac{-k^*}{1 - at^* e^{i\theta}} \tag{2.4}$$

$$P_{t1} = |E_{t1}|^2 = \frac{a^2 + |t|^2 - 2a|t|\cos(\theta)}{1 + a^2|t|^2 - 2a|t|\cos(\theta)} \tag{2.5}$$

The coupler region and waveguides may also be expressed as transmission matrices and solved by the transmission matrix method [19], which allows for modeling larger structures, including resonators with two bus waveguides, as well as multi-ring structures.

2.2.2 Rate equation model

Ring resonators may equivalently be described by a simple oscillator model [20]. In this model, A represents the time-varying, complex, electric field within the resonator, S represents the time-varying electric field at the input of the bus waveguide, T is the

transmitted electric field, ω_0 represents the resonance frequency, τ represents the photon lifetime within the resonator, k represents the amount of light coupled through the waveguide coupler in a single pass, and κ represents the coupling rate of the electric field through the coupler.

$$\frac{\mathrm{d}}{\mathrm{d}t}A = \left(i\omega_0 - \frac{1}{2\tau}\right)A + \kappa S \tag{2.6}$$

$$T = -S + kA \tag{2.7}$$

This first-order differential equation may be solved for A, yielding the standard equation for a Lorentzian resonance shape (Equation 2.8).

$$A = \frac{\kappa S}{i(\omega - \omega_0) + \frac{1}{2\tau}} \tag{2.8}$$

Notably, Equation 2.4 may also be written in this form by first-order Taylor expansion of the exponential term in the denominator. The physical parameters described in the previous section may be related to the oscillator model parameters as follows.

$$\kappa = k\frac{c}{n_g L} \tag{2.9}$$

L represents the round-trip length of the resonator; n_g represents the group index of the waveguide.

$$1/\tau = 1/\tau_0 + 1/\tau_{ex} \tag{2.10}$$

As τ represents the effective lifetime of the cavity as a whole, it is comprised of both the intrinsic photon lifetime, τ_0, as well as the coupler lifetime, τ_{ex}. As in the prior section, k denotes the light transferred by the coupler from the bus waveguide to the resonator in a single pass, and a denotes the electric field attenuation per round trip of

the resonator.

$$1/\tau_{ex} = k^2 \frac{c}{n_g L} \tag{2.11}$$

$$1/\tau_0 = (1 - a^2) \frac{c}{n_g L} \tag{2.12}$$

In ultra-high Q factor microresonators, Rayleigh backscattering within the resonator can lead the splitting of a single resonance into a doublet, due to mutual coupling of the forward and backward propagating electric fields. The oscillator model can be expanded to include backscattering as well by including a coupling rate between forward and backward modes [20].

$$\frac{\mathrm{d}}{\mathrm{d}t} \begin{pmatrix} A_{\mathrm{cw}} \\ A_{\mathrm{ccw}} \end{pmatrix} = \begin{pmatrix} i\omega_0 - \frac{1}{2\tau} & i\beta \\ i\beta & i\omega_0 - \frac{1}{2\tau} \end{pmatrix} \begin{pmatrix} A_{\mathrm{cw}} \\ A_{\mathrm{ccw}} \end{pmatrix} + \kappa \begin{pmatrix} S \\ 0 \end{pmatrix} \tag{2.13}$$

A_{cw} represents the forward, clockwise propagating field, A_{ccw} represents the backwards, counter clockwise propagating field, and β is the backscattering-induced coupling rate between the two fields. If the backscattering coefficient per unit length, b, of the waveguide (generally expressed in units of dB/mm) is known [21] , then the two may be related as follows

$$\beta = \sqrt{bL} \frac{c}{n_g L} \tag{2.14}$$

This model is used later in the chapter to model the measured transmission spectra of ultra-high Q resonators exhibiting doublet lineshapes.

2.3 Directional coupler design

2.3.1 Coupled mode theory

The operation of the coupling region discussed in the optical resonator models of the previous sections, and shown in Figure 2.7, can be described using either a two-state coupled mode theory [19] or two-state time-dependent perturbation theory [22], which are equivalent but for the choice of dependent variable: space, in the case of coupled mode theory; time, in the case of time-dependent perturbation theory. For a more complete treatment, refer to [22, 19, 23]. The necessary conclusions are summarized as follows.

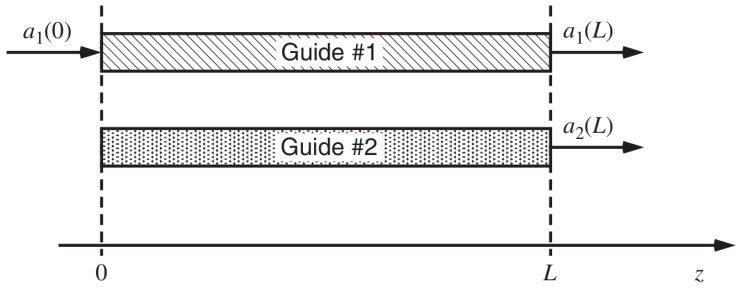

Figure 2.8: **Generic representation of a four-port directional coupler,** reproduced from [19].

A generic four-port directional coupler is shown in Figure 2.8. It is noted that while the figure implies propagation along the z-axis of a Cartesian coordinate system, the following equations work equally well along the azimuth direction of a cylindrical coordinate system, θ, (a concentric directional coupler), and the following equations may be adapted to a cylindrical coordinate system by simply replacing z with *theta*. The electric field at the position z within two parallel waveguides are described by $a_1(z)$ and $a_2(z)$, respectively. The evolution of the fields within the directional coupler are governed by

the following differential equation.

$$i\frac{\mathrm{d}}{\mathrm{d}z}\begin{pmatrix} a_1(z) \\ a_2(z) \end{pmatrix} = \begin{pmatrix} \beta_{11} & \beta_{12} \\ \beta_{21} & \beta_{22} \end{pmatrix} \begin{pmatrix} a_1(z) \\ a_2(z) \end{pmatrix} \tag{2.15}$$

β_{11} represents the propagation constant of the mode propagating in the first waveguide, and β_{22} represents the propagation constant of the mode propagating in the second waveguide. β_{12} and β_{21} represent the coupling strength between the two modes and are generally equal to one another. The differential equation may be solved by making the following substitution.

$$a_n(z) = c_n(z)e^{-i\beta_{nn}z} \tag{2.16}$$

After substitution, the differential equation may be written as follows.

$$i\frac{\mathrm{d}}{\mathrm{d}z}\begin{pmatrix} c_1(z) \\ c_2(z) \end{pmatrix} = \begin{pmatrix} 0 & \beta_{12}e^{-i\delta\beta x} \\ \beta_{21}e^{i\delta\beta x} & 0 \end{pmatrix} \begin{pmatrix} c_1(z) \\ c_2(z) \end{pmatrix} \tag{2.17}$$

The propagation constant mismatch, $\delta\beta$, between the two waveguides is defined as follows.

$$\delta\beta = \beta_{22} - \beta_{11} \tag{2.18}$$

For the initial condition $a_1(0) = 1$, $a_2(0) = 0$, the differential equation may then be solved to obtain a closed-form solution for the evolution of the electric fields within the directional coupler.

$$c_1(z) = \left(\cos Bz + \frac{i\delta\beta}{2B}\sin Bz\right)e^{-i\delta\beta z/2} \tag{2.19}$$

$$c_2(z) = -\frac{i\beta_{21}}{2B}\sin(Bz)e^{+i\delta\beta z/2} \tag{2.20}$$

Where the oscillation frequency describing the transfer of power between the modes, B is given by the following equation.

$$B^2 = |\beta_{21}|^2 + \left(\frac{\delta\beta}{2}\right)^2 \tag{2.21}$$

The total power coupled across the directional coupler, as a function of directional coupler length, is then given by $|c_2(z)|^2$.

$$|c_2(z)|^2 = C^2 \sin^2 Bz \tag{2.22}$$

Where the maximum amount of power transferred between the waveguides is given by the following equation

$$C^2 = \frac{|\beta_{21}|^2}{(\frac{1}{2}\delta\beta)^2 + |\beta_{21}|^2} \tag{2.23}$$

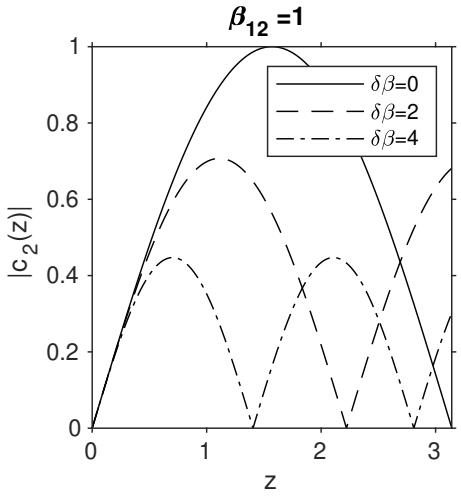

Figure 2.9: **Influence of coupling rate and mismatch on coupling coefficient.** Coupled field amplitude across a directional coupler for various values of propagation constant mismatch, at a fixed coupling rate $\beta_{12} = 1$.

This equation suggests an oscillatory transfer of power between the two waveguides, which is identical to the phenomenon of Rabi oscillations in quantum mechanics. The dependence of coupled electric field on coupler length for a selection of propagation constant mismatch is shown in Figure 2.9.

2.3.2 Calculation of the inter-modal coupling rate

The calculation of β_{21} may be carried out in two ways. It can be calculated from the mode overlap integral [19].

$$\beta_{12} = \frac{k_0^2}{2\beta_1} \frac{\int (\epsilon_1 - \epsilon_c) \mathbf{U_1}^* \cdot \mathbf{U_2}\, dA}{\int |U_1|^2\, dA} \tag{2.24}$$

$$\beta_{21} = \frac{k_0^2}{2\beta_2} \frac{\int (\epsilon_2 - \epsilon_c) \mathbf{U_2}^* \cdot \mathbf{U_1}\, dA}{\int |U_2|^2\, dA} \tag{2.25}$$

Where $\mathbf{U_{1,2}}$ are the normalized electric field distribution of the modes of the individual waveguides, $\epsilon_{1,2}$ are the dielectric constant profiles of each individual waveguide, and ϵ_c is the dielectric constant profile in the absence of both waveguides, and k_0 is the free-space wavenumber. However, the equation 2.21 suggests a straightforward method to infer the coupling rate without calculating an overlap integral. Simulation of the eigenmodes of the directional coupler will result in the coupled super-modes, which are superpositions of the modes of the individual waveguides. If the super-modes of the system have propagation constants β_x and β_y, then their difference represents the Rabi oscillation frequency

$$B = \frac{\beta_x - \beta_y}{2} \tag{2.26}$$

The propagation constant mismatch, $\delta\beta$, can be calculated from the propagation constants of the isolated waveguides (Equation 2.18), which can in turn be used to calculate

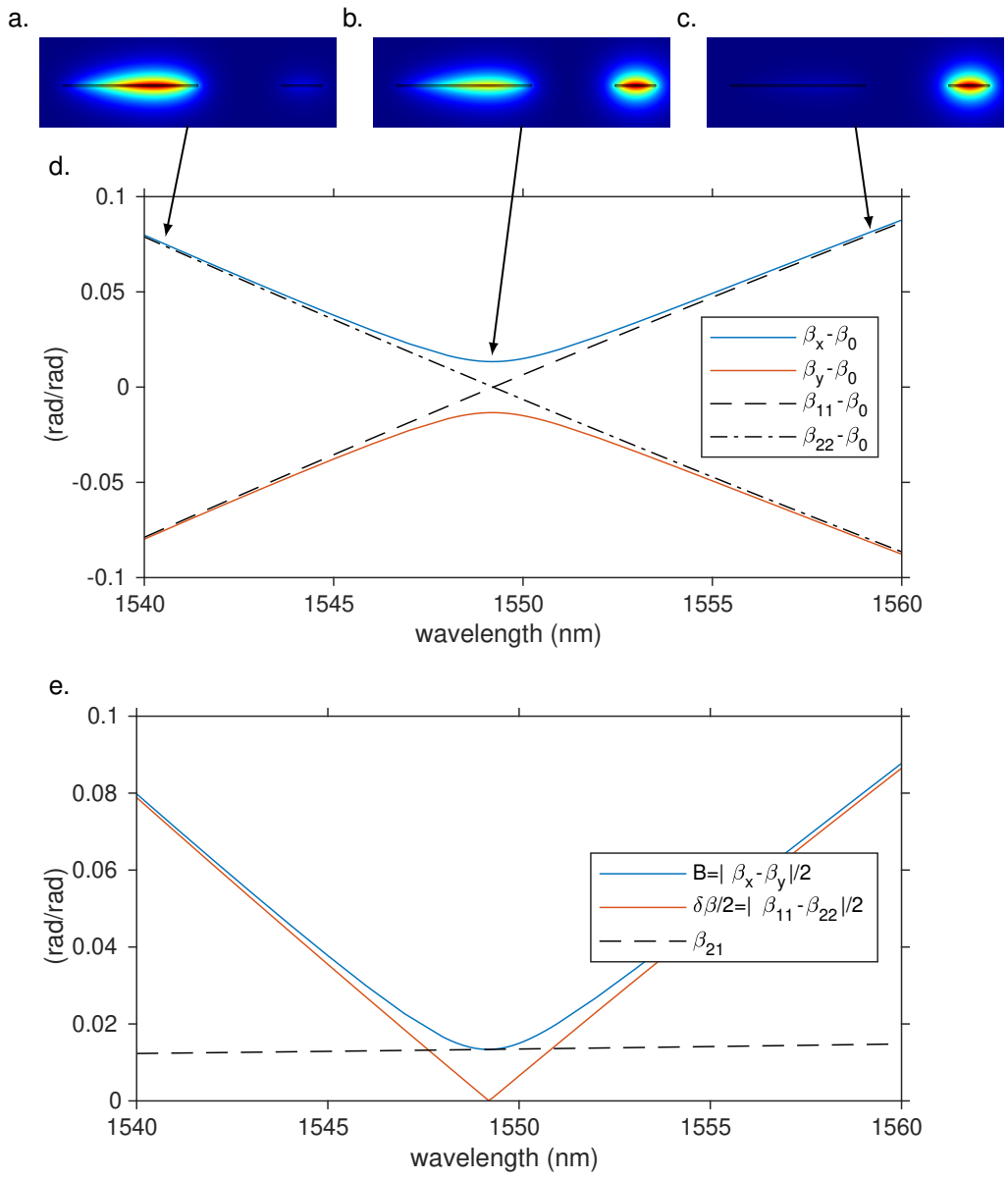

Figure 2.10: **Coupling rate calculation.** Eigenmodes of concentric waveguides propagating in the azimuth direction in a cylindrical geometry, with 5 µm separation, at a radius of 1 mm are shown at (a) 1540 nm, (b) 1549.2 nm, and (c) 1560 nm wavelength. (d) Propagation constants of the eigenmodes (supermodes) of the coupled waveguides, $\beta_{x,y}$, and the eigenmodes of the isolated waveguides, $\beta_{11,22}$, after subtracting the average dispersion, $\beta_0 = (\beta_{11} + \beta_{22})/2$. $\beta_{11,22}$ are matched at 1549.2 nm, leading to an avoided mode crossing for $\beta_{x,y}$. Propagation constants for the modes shown in (a), (b), and (c) are indicated. (e) B, $\delta\beta/2$, and β_{21} are calculated from the respective propagation constants shown in (d). The coupling rate β_{21} is identical to B where the propagation constants mismatch vanishes, $\delta\beta = 0$. The spectral dependence of coupling rate can be observed, which increases with increasing wavelength.

the coupling rate.

$$|\beta_{21}| = \sqrt{\left(\frac{\beta_x - \beta_y}{2}\right)^2 - \left(\frac{\delta\beta}{2}\right)^2} \tag{2.27}$$

This process is shown in Figure 2.10, for the design of a concentric directional coupler [24, 13] in 100 nm thick silicon nitride. In this simulation, the inner waveguide width was chosen as 8 µm, while outer waveguide width was chosen to match its propagation constant with the inner waveguide at approximately 1550 nm wavelength. The distance between the outer sidewall of the inner waveguide and the inner sidewall of the outer waveguide, that is, the distance between waveguides, was chosen to be 5 µm. Since the waveguides differ in geometry, they have different dispersion, and the matching condition, $\delta\beta = 0$ is precisely fulfilled only at a specific wavelength, as shown in Figure 2.10d,e. It is important to note that this situation is very different from that of a directional coupler consisting of parallel, straight waveguides; in which selecting both waveguides to have identical width guarantees the matching condition at all wavelengths due to symmetry. In Figure 2.10e, propagation constant, $\delta\beta$, the oscillation rate, B, and the coupling rate, β_{21} are calculated over the wavelength range 1540 nm to 1560 nm. The coupling rate, β_{21}, increases with increasing wavelength, due to the spectral dependence of modal confinement.

2.3.3 Selection of the coupling rate

For any desired coupling coefficient, $k = c_2(z)$, there is some freedom in the selection of the coupling rate, β_{21}. This is evident in Equation 2.22, in which, assuming that the propagation constants of the waveguides are matched, that is $B = \beta_{21}$, a choice of smaller or larger β_{21} can be compensated by a larger or smaller coupling length, z. Thus, the choice of coupling rate and coupling length merit discussion. This is particularly relevant to designs in which the directional coupler is asymmetric, as is the case in a concentric

directional coupler, because the waveguides will generally exhibit different dispersion, and the propagation constant matching condition is only fulfilled at a single wavelength for any given geometry. Furthermore, any dimensional variability in the fabrication process will likely impact the propagation constants of the respective waveguides differently, further influencing the matching of propagation constants.

From Equation 2.22, the coupling experiences a local maximum at $Bz = \pi/2$, and it is evident from Figure 2.9 that the location of this local maximum, both in coupler length, z, and in coupling amplitude, $|c_2(z)|$, is sensitive to the value of propagation constant mismatch, $\delta\beta$. Thus, if the directional coupler is designed to operate in the regime $Bz \geq \pi/2$, the coupling becomes sensitive to propagation constant mismatch, $\delta\beta$, and will be sensitive to any variability in the fabrication process.

However, it can also be seen in Figure 2.9 that in the regime $Bz < \pi/2$, the coupling amplitude is relatively invariant to propagation constant mismatch. This can be understood if we assume that $Bz \ll 1$, allowing the use of its first-order Taylor expansion to substitute $\sin(Bz) \approx Bz$ in Equation 2.22.

$$|c_2(z)|^2 = C^2 \sin^2(Bz) \approx C^2(Bz)^2 = \frac{|\beta_{21}|^2}{(\frac{1}{2}\delta\beta)^2 + |\beta_{21}|^2} \left(|\beta_{21}|^2 + \left(\frac{\delta\beta}{2}\right)^2 \right) z^2 = |\beta_{21}|^2 z^2 \tag{2.28}$$

Thus, if the requirement $Bz \ll 1$ can be met, the coupling is determined only by the coupling rate, β_{21}, and the coupler length, z; and the propagation constant mismatch $\delta\beta$ does not impact coupling, leading to a more fabrication-tolerant design. As long as the desired coupling, k is small, that is, $k = c_2(z) \ll 1$ (which is generally the case when designing directional couplers for high Q resonators), then a requirement of $Bz \ll 1$ leads to a condition on the tolerable mismatch

$$\frac{\delta\beta}{2} \ll \frac{1}{z} = \frac{\beta_{21}}{k} \tag{2.29}$$

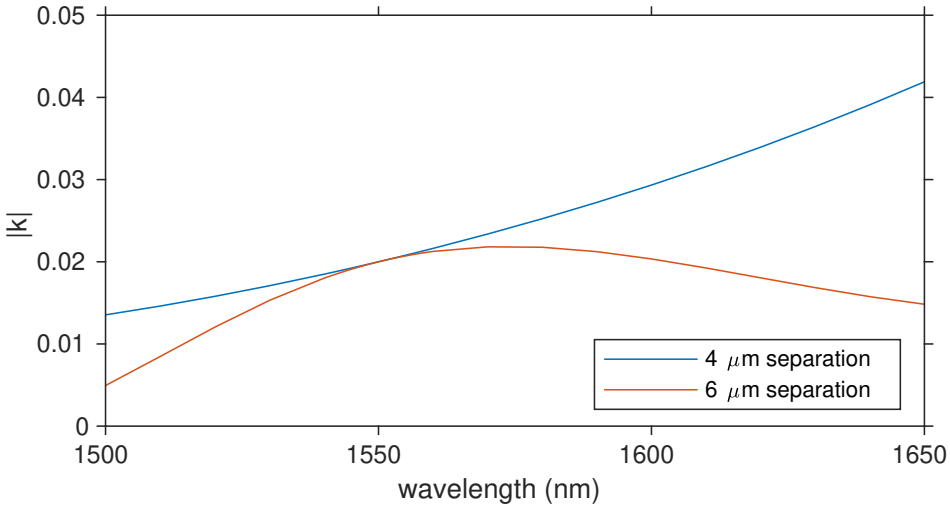

Figure 2.11: **Wavelength dependence of the coupling coefficient.** Coupling coefficient for concentric directional couplers in 100 nm thick silicon nitride at 1 mm radius, and 8 µm inner waveguide width. The couplers are both designed to be propagation-constant-matched at 1550 nm, and to have coupling coefficient of $k = 0.02$ at 1550 nm. In the coupler with smaller, 4 µm separation between waveguides, the coupling coefficient increases monotonically. In the coupler with the larger, 6 µm separation between waveguides, the coupling coefficient exhibits a local maximum.

Thus, for a fixed coupling strength, k, the choice of length of the directional coupler, z, determines the sensitivity to propagation constant mismatch. Longer coupling regions (larger z) with weaker coupling strength (smaller β_{21}) tolerate less mismatch. Shorter coupling regions (smaller z) with stronger coupling strength (larger β_{21}) can tolerate greater mismatch. This is demonstrated in Figure 2.11 for two concentric directional couplers at a radius of 1 mm and with 8 µm inner waveguide width, similar to the directional coupler designed for Figure 2.10. In Figure 2.11, both couplers are designed to be matched at 1550 nm, while their lengths are chosen to achieve a coupling coefficient of $k = 0.02$ at 1550 nm as well. The coupler with 4 µm separation between waveguides (the distance between the outer sidewall of the inner waveguide, and the inner sidewall of the outer waveguide) requires 0.44 rad coupling length to reach the desired coupling, whereas the coupler with 6 µm separation requires 4.8 rad of coupling length. The coupling coefficient, k, of the 4 µm separation directional coupler increases with wavelength because

the coupling rate, β_{21}, increases with wavelength, similar to the the coupler with 5 µm separation in Figure 2.10e. However, the coupling rate is much smaller, and the length much longer, at 6 µm separation. As a result, $|k|$ exhibits a local maximum as increasing coupling rate towards longer wavelength is outweighed by increasing propagation constant mismatch away from the 1550 nm wavelength at which the propagation constants are matched. In applications where the dependence of coupling coefficient on wavelength should be flat, the coupler can be designed to intentionally introduce propagation constant mismatch at the operating wavelength.

While a long coupling region, with a low coupling rate, would seem detrimental due to increased sensitivity to propagation constant mismatch from fabrication tolerances, it does convey benefit in the form of more selective coupling. In a concentric directional coupler, the inner waveguide is generally wider, and may support multiple transverse modes, while the outer waveguide may only support a single mode. If the directional coupler is designed such that the propagation constant of the outer waveguide is matched to the fundamental mode of the inner waveguide, then the parasitic coupling of the outer waveguide to the higher-order modes of the inner waveguide may also be calculated using Equation 2.22. While the propagation constant mismatch to the higher order modes of the inner waveguide ($\delta\beta$) are determined by the geometry of the inner waveguide, reducing the coupling rate of the outer waveguide to the fundamental mode of the inner waveguide also reduces the interaction of the outer waveguide with the higher-order modes of the inner waveguide (β_{21}), which reduces the maximum amount of power that may be transferred to undesired modes via Equation 2.23. Thus, it is possible to design a directional coupler to couple selectively to a particular mode of a waveguide which supports multiple transverse modes by reducing the coupling rate while increasing the coupling length.

2.3.4 Effective coupling length

The calculation and selection of the coupling rate, β_{21} has been addressed. However, for a parallel, straight waveguide directional coupler, as well as for a concentric, curved waveguide directional coupler, accurately determining the coupling length is necessary to calculate the overall coupling coefficient, k, of the directional coupler *a priori*. For a parallel directional coupler, the coupling rate is expressed in units of $\mathrm{rad\,m^{-1}}$, and the coupling length is expressed in meters. For the concentric directional coupler, the coupling rate is expressed in units of $\mathrm{rad\,rad^{-1}}$, and the coupling length is an arc length, in radians. In both cases however, calculating the coupling based on the length over which the directional coupler maintains an invariant cross-section, and the coupling rate within this region, will underestimate the coupling coefficient .

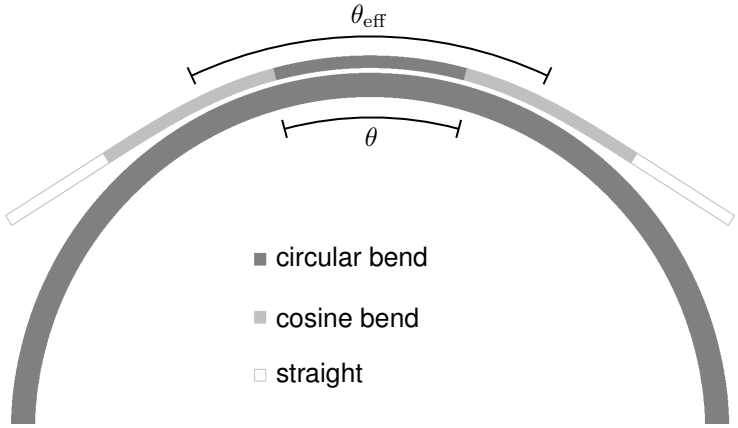

Figure 2.12: **Schematic of a concentric directional coupler.** The lower (inner) waveguide follows a perfectly circular bend, with constant curvature. The upper (outer) waveguide is concentric with the lower (inner) waveguide within the coupling region, over an arc length designated as θ. Adiabatic transitions derived from a cosine curve are used to approach the coupling region gradually, such that the effective coupling arc length spans both the circular bend and parts of the cosine bends, designated as θ_{eff}.

In Figure 2.12, the directional coupler cross-section remains invariant over an arc length, θ. In the pictured schematic, cosine bends are used to adiabatically transition from a straight routing waveguide to a curved waveguide in the vicinity of the directional

coupler. These adiabatic transitions also contribute to the coupling. From a theoretical perspective, Equation 2.15 could accomodate gradual (adiabatic) spatial variation in the coupling matrix β_{nm}, and the coupling could be integrated over the full length to include the impact of the adiabatic transitions to the coupling region. In practice, it is sufficient to empirically estimate an effective coupling arc length, $z = \theta_{\text{eff}}$ that is larger than θ, which, combined with the calculated coupling rate, β_{21}, can be used to calculate the coupling coefficient, k, using Equation 2.22.

The empirical method used in this work was to determine a threshold separation at which the coupling rate, β_{21}, is decreased by a factor of $\sqrt{2}$ from the designed value. For example, in the coupler designed in Figure 2.10, the coupling rate at separation of 5.25 µm is smaller than the coupling rate at 5 µm separation by approximately this factor, and the effective coupler length can be estimated as the arc length of the coupler for which the separation of the two waveguides does not exceed 5.25 µm. The choice of the reduction factor does not need to be precise, as the separation between waveguides within the adiabatic transition increases quadratically with distance beyond the coupling region. Thus, whether the reduction factor is chosen as $\sqrt{2}$ or 2, both result in approximately the same effective coupling length, and the deviation of the fabricated couplers from the desired coupling coefficient designed by this method which was generally observed to be below the variability in the coupling coefficient due to fabrication tolerances.

By this method, it is also possible to model a directional coupler formed between a straight waveguide and a curved waveguide. This is a common configuration for coupling to a perfectly circular ring resonator, as it is a simple structure to specify and draw. In this case the linear propagation constant of the straight waveguide can be approximately converted to the cylindrical coordinate system of the curved waveguide by multiplying by its distance from the center of curvature. The coupling rate may be approximated for the waveguide separation where the straight waveguide reaches minimum separation with

the curved waveguide. The effective coupling length may be estimated by the method described above. In this case, the straight waveguide to curved waveguide directional coupler can be considered a special case of a short, concentric directional coupler. From the prior discussion on the selection of coupling rate, a few properties of the straight-to-curved coupler can be inferred. Due to short coupling length, straight-to-curved couplers will require narrower space between the coupled waveguides to achieve a high coupling rate. If a particularly high coupling coefficient ($k \approx 1$) is required, then this may lead to excess loss in the directional coupler, as it becomes less adiabatic. In turn, if either straight or curved waveguide is multimode, the large coupling rate reduces the selectivity of the propagation-constant-matching condition. This makes the coupler more susceptible to coupling to undesired modes.

2.3.5 Sine bend adiabatic transition

In order to connect between straight waveguides and curved waveguides, a transition was developed based on sine bends with an adiabatic transition of the curvature. Such transitions were used throughout this work in order to draw racetrack resonators, as well as to transition the the curvature of the bus waveguide for concentric directional couplers. The adiabatic sine bends used in this work were defined by the following parametric curve,

$$t = [0, 1] \tag{2.30}$$

$$x(t) = \frac{\pi}{2} t R \sqrt{c} \tag{2.31}$$

$$y(t) = cR \sin \frac{\pi}{2} t \tag{2.32}$$

in which t is the parametric variable, and $x(t)$ and $y(t)$ are the parametric functions determining the coordinates of the bend. At $t = 1$, the curvature of the bend is $-1/R$, such that it may be connected to a circular bend of radius R. At $t = 0$, the curvature is zero, such that it may be connected to a straight waveguide. The parameter c allows the adiabaticity of the bend to be adjusted, such that larger values of c correspond to longer adiabatic transitions, while smaller values of c correspond to shorter adiabatic transitions. The value of c was generally chosen such that $c < 1$.

Summary

Proper design is a key ingredient for successfully achieving low-loss photonic integrated circuits. This chapter has presented the design considerations underpinning the choice of waveguide geometry, to minimize propagation loss caused by the waveguide sidewall, to ensure a single mode waveuguide, as well as to ensure that losses dependent on the waveguide geometry, such as bending loss and substrate leakage, were negligible. At the device level, the resonator, a key building-block device, was introduced, and two models for its operation were presented. Finally, a coupled mode theory was applied to model the operation of a directional coupler, applicable to designs with both Cartesian and cylindrical symmetry. Practical considerations for the design, such as selection of the coupling strength, the effective coupling length, and sine-bend transitions for adiabatic change in curvature, were also discussed. The contents of this chapter formed the basis for the design of the photonic integrated circuits presented in the following chapters.

Bibliography

[1] C. G. Roeloffzen, L. Zhuang, C. Taddei, A. Leinse, R. G. Heideman, P. W. van Dijk, R. M. Oldenbeuving, D. A. Marpaung, M. Burla, and K.-J. Boller, *Silicon nitride microwave photonic circuits*, *Optics Express* **21** (2013), no. 19 22937–22961.

[2] K. Wörhoff, R. G. Heideman, A. Leinse, and M. Hoekman, *TriPleX: a versatile dielectric photonic platform*, *Advanced Optical Technologies* **4** (2015), no. 2 189–207.

[3] D. J. Blumenthal, R. Heideman, D. Geuzebroek, A. Leinse, and C. Roeloffzen, *Silicon nitride in silicon photonics*, *Proceedings of the IEEE* **106** (2018), no. 12 2209–2231.

[4] J. Liu, G. Huang, R. N. Wang, J. He, A. S. Raja, T. Liu, N. J. Engelsen, and T. J. Kippenberg, *High-yield, wafer-scale fabrication of ultralow-loss, dispersion-engineered silicon nitride photonic circuits*, *Nature communications* **12** (2021), no. 1 1–9.

[5] X. Ji, F. A. Barbosa, S. P. Roberts, A. Dutt, J. Cardenas, Y. Okawachi, A. Bryant, A. L. Gaeta, and M. Lipson, *Ultra-low-loss on-chip resonators with sub-milliwatt parametric oscillation threshold*, *Optica* **4** (2017), no. 6 619–624.

[6] M. H. Pfeiffer, J. Liu, A. S. Raja, T. Morais, B. Ghadiani, and T. J. Kippenberg, *Ultra-smooth silicon nitride waveguides based on the Damascene reflow process: fabrication and loss origins*, *Optica* **5** (2018), no. 7 884–892.

[7] J. F. Bauters, M. J. Heck, D. D. John, J. S. Barton, C. M. Bruinink, A. Leinse, R. G. Heideman, D. J. Blumenthal, and J. E. Bowers, *Planar waveguides with less*

than 0.1 dB/m propagation loss fabricated with wafer bonding, *Optics Express* **19** (2011), no. 24 24090–24101.

[8] J. F. Bauters, M. J. Heck, D. John, D. Dai, M.-C. Tien, J. S. Barton, A. Leinse, R. G. Heideman, D. J. Blumenthal, and J. E. Bowers, *Ultra-low-loss high-aspect-ratio Si_3N_4 waveguides*, *Optics Express* **19** (2011), no. 4 3163–3174.

[9] T. Barwicz and H. A. Haus, *Three-dimensional analysis of scattering losses due to sidewall roughness in microphotonic waveguides*, *Journal of Lightwave Technology* **23** (2005), no. 9 2719.

[10] T. Herr, V. Brasch, J. D. Jost, C. Y. Wang, N. M. Kondratiev, M. L. Gorodetsky, and T. J. Kippenberg, *Temporal solitons in optical microresonators*, *Nature Photonics* **8** (2014), no. 2 145–152.

[11] A. L. Gaeta, M. Lipson, and T. J. Kippenberg, *Photonic-chip-based frequency combs*, *nature photonics* **13** (2019), no. 3 158–169.

[12] X. Ji, J. Liu, J. He, R. N. Wang, Z. Qiu, J. Riemensberger, and T. J. Kippenberg, *Compact, spatial-mode-interaction-free, ultralow-loss, nonlinear photonic integrated circuits*, *arXiv preprint arXiv:2109.06764* (2021).

[13] W. Jin, Q.-F. Yang, L. Chang, B. Shen, H. Wang, M. A. Leal, L. Wu, M. Gao, A. Feshali, M. Paniccia, *et. al.*, *Hertz-linewidth semiconductor lasers using CMOS-ready ultra-high-Q microresonators*, *Nature Photonics* **15** (2021), no. 5 346–353.

[14] J. F. Bauters, M. Heck, D. Dai, J. Barton, D. Blumenthal, and J. Bowers, *Ultralow-loss planar Si_3N_4 waveguide polarizers*, *IEEE Photonics Journal* **5** (2012), no. 1 6600207–6600207.

[15] K. J. Vahala, *Optical microcavities*, *Nature* **424** (2003), no. 6950 839–846.

[16] A. Yariv, *Universal relations for coupling of optical power between microresonators and dielectric waveguides*, *Electronics letters* **36** (2000), no. 4 321–322.

[17] A. Yariv, *Critical coupling and its control in optical waveguide-ring resonator systems*, *IEEE Photonics Technology Letters* **14** (2002), no. 4 483–485.

[18] D. G. Rabus, *Integrated ring resonators*. Springer, 2007.

[19] L. A. Coldren, S. W. Corzine, and M. L. Mashanovitch, *Diode lasers and photonic integrated circuits*, vol. 218. John Wiley & Sons, 2012.

[20] M. L. Gorodetsky, A. D. Pryamikov, and V. S. Ilchenko, *Rayleigh scattering in high-Q microspheres*, *JOSA B* **17** (2000), no. 6 1051–1057.

[21] F. Morichetti, A. Canciamilla, and A. Melloni, *Statistics of backscattering in optical waveguides*, *Optics letters* **35** (2010), no. 11 1777–1779.

[22] H. Kroemer, *Quantum mechanics: For engineering, materials science, and applied physics*. Pearson, 1994.

[23] R. v. Schmidt and R. Alferness, *Directional coupler switches, modulators, and filters using alternating $\delta\beta$ techniques*, *IEEE Transactions on Circuits and Systems* **26** (1979), no. 12 1099–1108.

[24] D. T. Spencer, J. F. Bauters, M. J. Heck, and J. E. Bowers, *Integrated waveguide coupled Si_3N_4 resonators in the ultrahigh-Q regime*, *Optica* **1** (2014), no. 3 153–157.

Chapter 3

CMOS-ready, ultra high Q microresonators

This section presents experimental results in fabricated silicon nitride waveguides and resonators, fabricated in a high-volume complementary metal-oxide-semiconductor (CMOS) foundry. The primary achievement presented is the fabrication of resonators featuring Q factors over 260 million at bend radius of 1 mm. Furthermore, comparable Q factor is replicated across the entirety of a 200 mm wafer, showing great promise for future large-scale production of ultra-high Q photonic integrated circuits. These results were originally published in [1].

3.1 Device characterization

The samples are fabricated in a high-volume CMOS foundry on 200 mm wafers following the process of Bauters et al. [2] that was discussed earlier in Chapter 2. A photograph of a singulated 200 mm wafer is shown in Figure 3.1. Compared to [2, 3, 4, 5], the thickness of the Si_3N_4 core was increased from 40 nm to 100 nm, which enabled a bending

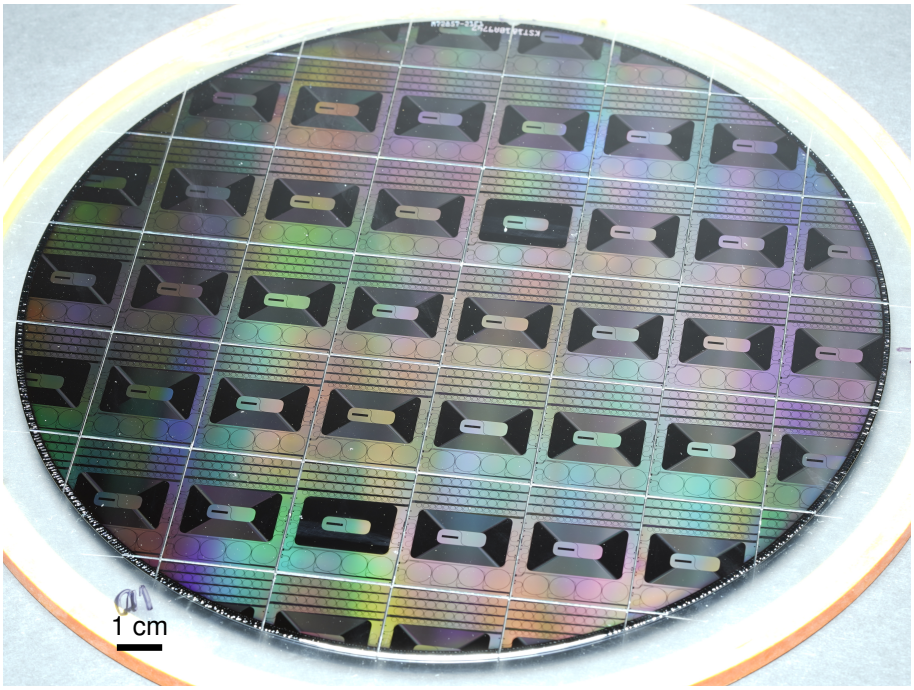

Figure 3.1: **Photograph of a 200mm wafer,** featuring ultra-high Q factor microresonators and spiraled waveguide delay lines. The wafer has been mounted on adhesive tape for the purpose of die singulation using a dicing saw. Reproduced from [1].

radius below 1 mm, and allowed higher integration density. Furthermore, a top cladding thickness of 2 µm was sufficient, which obviated the need for chemical-mechanical polishing and bonding of additional thermal SiO_2 on top [2, 3]. To minimize the residual hydrogen content of the deposited Si_3N_4 and SiO_2 films, extended thermal treatment totaling over 20 hours of annealing was applied at 1150 °C.

Microresonators having three different free spectral ranges (FSR) were fabricated. Those resonators having 30 GHz FSR were in a whispering-gallery-mode ring geometry. Single-mode waveguides were used to form resonators with 5 GHz and 10 GHz FSR, and were laid out as racetracks to reduce footprint. A photograph featuring 30 GHz resonators and a 5 GHz resonator is shown in Figure 3.2.

To characterize the resonators, the chips were coupled to fiber, and a tunable laser was used to interrogate the transmission spectra of the resonances. As the tunable laser was

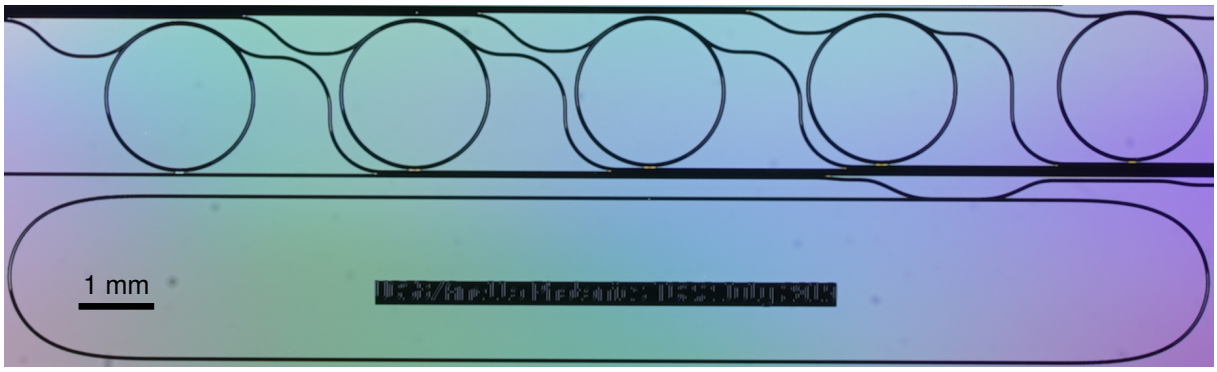

Figure 3.2: **Photograph of resonators.** Whispering-gallery-mode ring resonators with 1 mm bending radius and 30 GHz FSR, alongside a single-transverse-mode racetrack resonator with 1 mm minimum bending radius and 5 GHz FSR. Reproduced from [1].

swept, the transmitted power was measured using a photodetector to collect to resonator transmission spectra. Simultaneously, the transmission through a separate unbalanced fiber Mach-Zehnder interferometer was measured and used to calibrate the laser tuning rate. A measured resonance spectrum is presented in Figure 3.3a. The ring resonator models presented in chapter 2 were used to extract the resonator linewidth, and to infer loaded, coupled, and intrinsic optical Q factors. Cavity ring down was also performed as a separate check of these Q measurements, shown in Figure 3.3b. Spectra were observed to occur in doublets on account of both the ultra-high-Q and the presence of waveguide backscattering (Figure 3.3a) [6, 7]. By fitting the doublet line shape of the 30 GHz ring resonator, intrinsic Q of 220 M and loaded Q of 150 M are extracted at 1560 nm, which are further confirmed by the ring-down trace of the resonance in Figure 3.3b.

The spectral dependences of Q-factors in ring- and racetrack-resonators are shown in Figure 3.4, and provide insight into the origins of loss. A reduction in the value of Q for both resonators around 1510 nm is due to absorptive N-H bonds in the Si_3N_4 core. Beyond this wavelength, the intrinsic Q factor increases monotonically versus wavelength, likely limited by Rayleigh scattering. The highest Q factor is obtained using a 30 GHz FSR

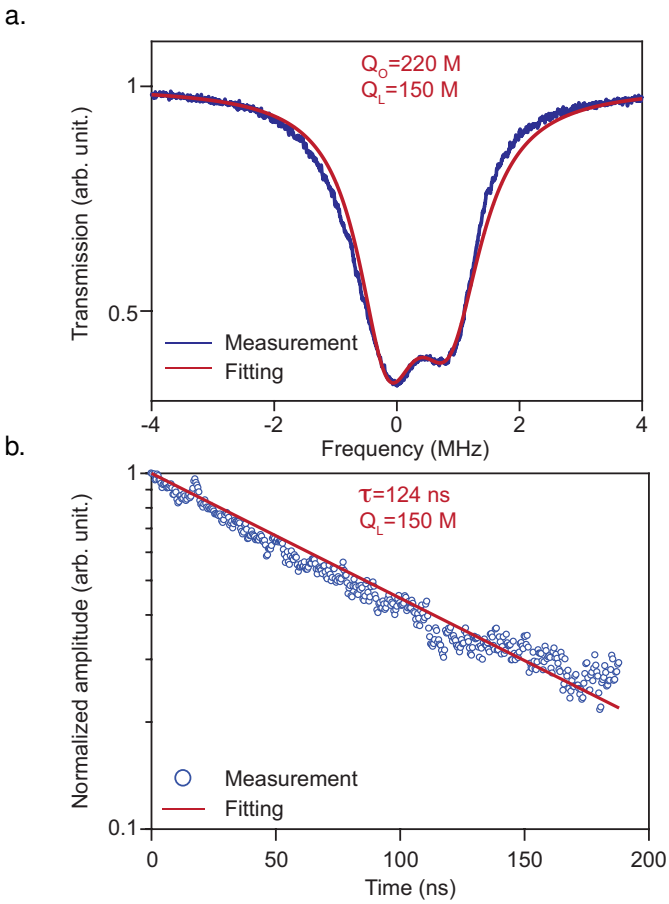

Figure 3.3: Q **factor measurement.** (a) Transmission spectrum of a high-Q mode at 1560 nm in a 30 GHz ring resonator. Interfacial and volumetric inhomogeneities induce Rayleigh scattering, causing resonances to appear as doublets due to coupling between counter-propagating modes. Intrinsic Q of 220 M and loaded Q of 150 M are extracted by fitting the asymmetric mode doublet. (b) The ring-down trace of the mode shows 124 ns photon lifetime, corresponding to a 150 M loaded Q. Reproduced from [1].

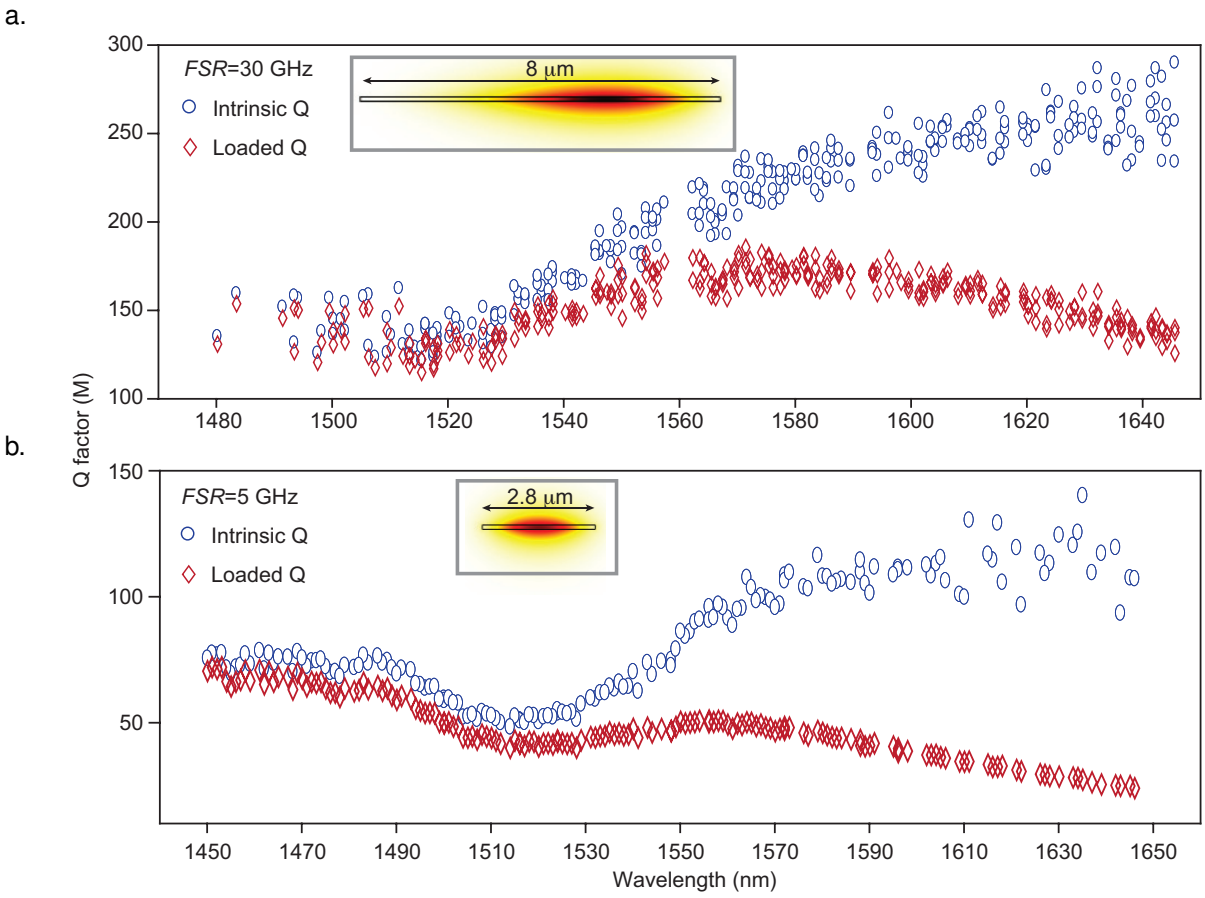

Figure 3.4: **Intrinsic and loaded Q factors of the fundamental TE mode plotted versus wavelength** for (a) a 30 GHz FSR whispering-gallery-mode ring resonator and (b) a 5 GHz FSR single-transverse-mode racetrack resonator. The transverse mode profiles are shown as insets. Reproduced from [1].

resonator (mean value of 260 M and standard deviation of 13.5 M over 34 modes) and observed in the 1630 nm to 1650 nm wavelength range, shown in Figure 3.4a. The overall lower Q factor of the 5 GHz racetrack resonator, shown in Figure 3.4b, suggests excess propagation loss in the single mode waveguides. This is likely caused by greater influence of sidewall scattering loss due to increased modal overlap with the waveguide sidewall in the single mode waveguide as compared to the whispering-gallery mode waveguide.

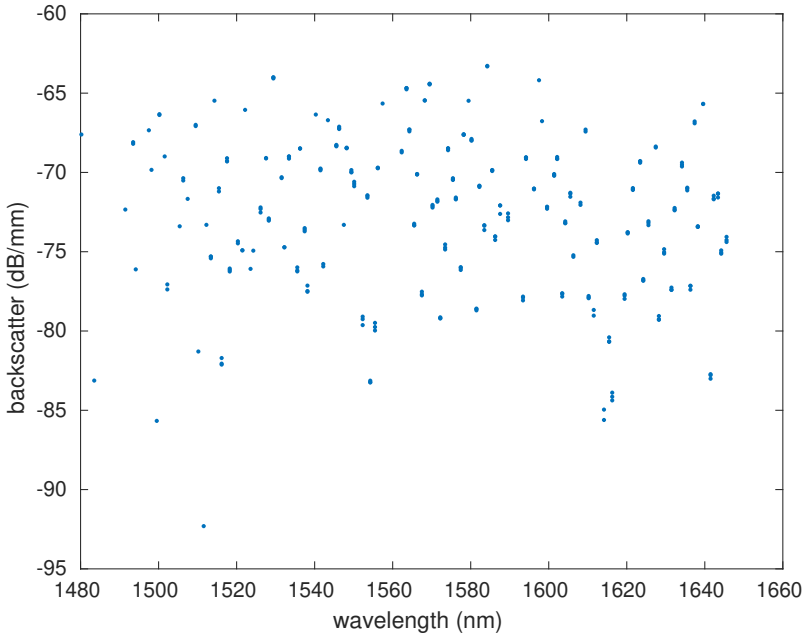

Figure 3.5: **Backscatter rate within the 30 GHz FSR ring resonator.** The backscatter coefficient was extracted from the fitted resonator transmission spectra, from the same data set as Figure 3.4a.

The backscatter coefficient coefficient per unit length, related to the backscatter rate through Equation 2.14, is plotted in Figure 3.5 for the same 30 GHz FSR, whispering-gallery-mode resonator as presented in Figure 3.4a. The backscatter is extracted by fitting each resonance shape, simultaneously with fitting the loss parameters. The backscatter within individual resonances is observed to have substantial variability about a mean value of -70.6 dB/mm, though no overall dependence on the wavelength is observed.

3.2 Wafer-level yield

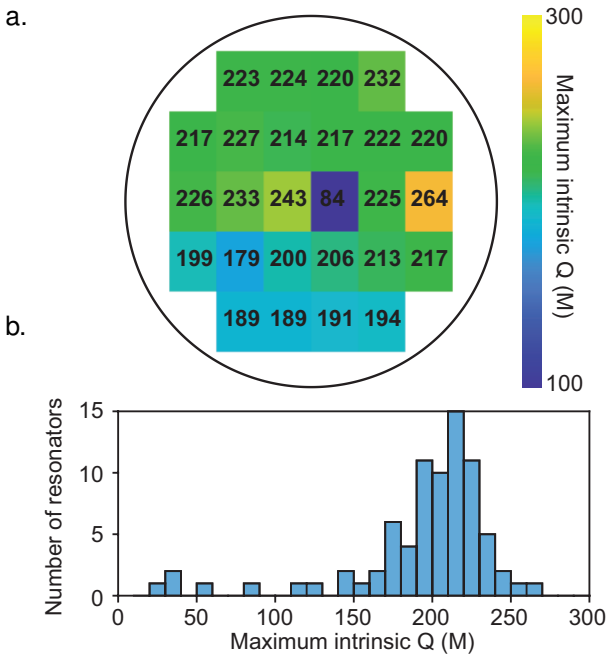

Figure 3.6: **Wafer-scale Q factor measurement.** The Q factor for each of three 30 GHZ FSR ring resonators on each of the 26 dies of the wafer shown in Figure 3.1 was calculated as the average Q factor in the 1620 nm to 1650 nm range. (a) A wafer map of the highest Q factor on each die and (b) histogram of Q factors of those 78 resonators demonstrate that ultra-high Q is achieved across the wafer. Reproduced from [1].

The capability of CMOS-foundry fabrication to produce ultra-high Q factor at the wafer scale is exhibited in Fig 3.6b, wherein the intrinsic Q factors of 30 GHz FSR ring resonators measured throughout the wafer were observed to be clustered in the 170 M to 270 M range. Moreover, a die map (Fig 3.6a) reveals that an intrinsic Q factor in the vicinity of 200 M is observed on each die, with the exception of a single die at the center subjected to handling error after fabrication.

As a further indication of the high yield possible in this platform, an optical frequency domain reflectometry measurement [8] is presented in Figure 3.7. The consistency of the backscattered signal over the length of the 1.73 m long spiraled waveguide indicates a

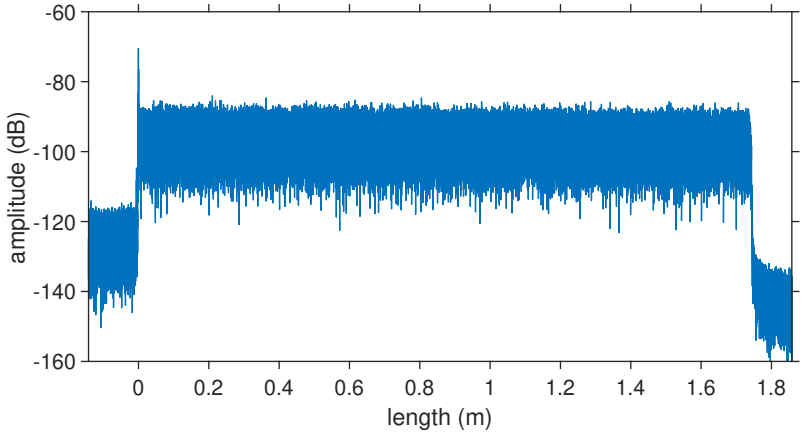

Figure 3.7: **Optical frequency domain reflectometry measurement** of a 1.73 m long, single-mode silicon nitride waveguide with 100 nm thickness and 2.8 µm width.

highly uniform waveguide that is free of point defects.

3.3 O-band Q measurement

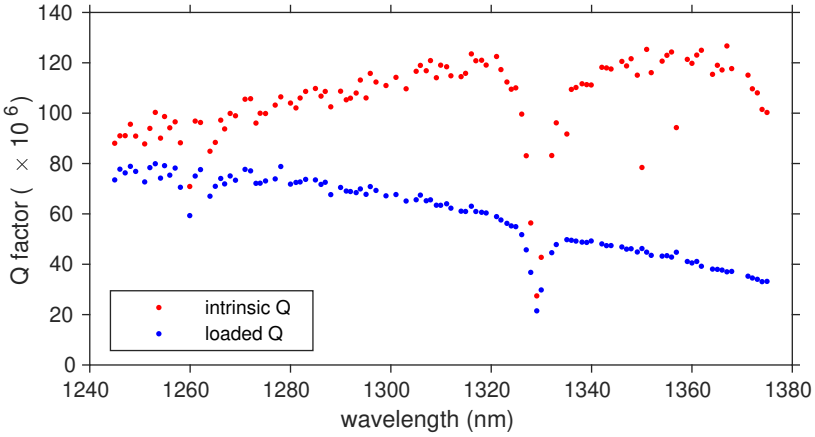

Figure 3.8: **Q measurement of a resonator designed to operate at 1310 nm.**

Figure 3.8 presents measured Q factors for a whispering-gallery resonator in this platform designed to operate in the telecommunications O-band. The core thickness is 100 nm, while the width of the ring waveguide is 12 µm such that it operates as a whispering-gallery mode resonator. The ring radius is approximately 580 µm, corre-

sponding to FSR of approximately 50 GHz

The dips in measured Q factor evident at 1260 nm and 1330 nm is likely due to higher-order mode crossings. The Q factor reduction at wavelength approaching 1380 nm is likely due to first harmonic of an infrared SiO-H absorption (see Chapter 7). An intrinsic Q factor of 120 M is observed at 1310 nm.

3.4 Performance Comparison

Finally, these results are compared with state-of-the-art integrated microresonators in other integrated photonic platforms. For devices with both integrated waveguide coupler and resonator, a few platforms have emerged as able to provide ultra-high Q ($Q > 10$ M). In silica ridge resonators, a Q factor of 205 M has been demonstrated [9], while in low-confinement silicon nitride, a Q factor of 216 M has been demonstrated [5]. However, these platforms pose challenges to photonic integration with large scale and high density, e.g. the use of suspended structures [9] or the requirement for centimeter-level bending radius [5]. While these limitations are not present in high-confinement silicon nitride resonators, the highest demonstrated Q factor is lower, 67 M [10]. In addition to record-high Q factor, owing to their compact footprint, the current resonators stand out among ultra-high Q resonators for having the highest finesse as well. Figure 3.9 provides a comparison as a plot of the Q and finesse of the current work with the state-of-the-art.

Summary

In this chapter, high-yield, ultra-low loss fabrication of silicon nitride photonic devices was presented. Careful device design (outlined in chapter 2), and better process control due to the use of a commercial CMOS foundry, achieved a unique combination of mm-

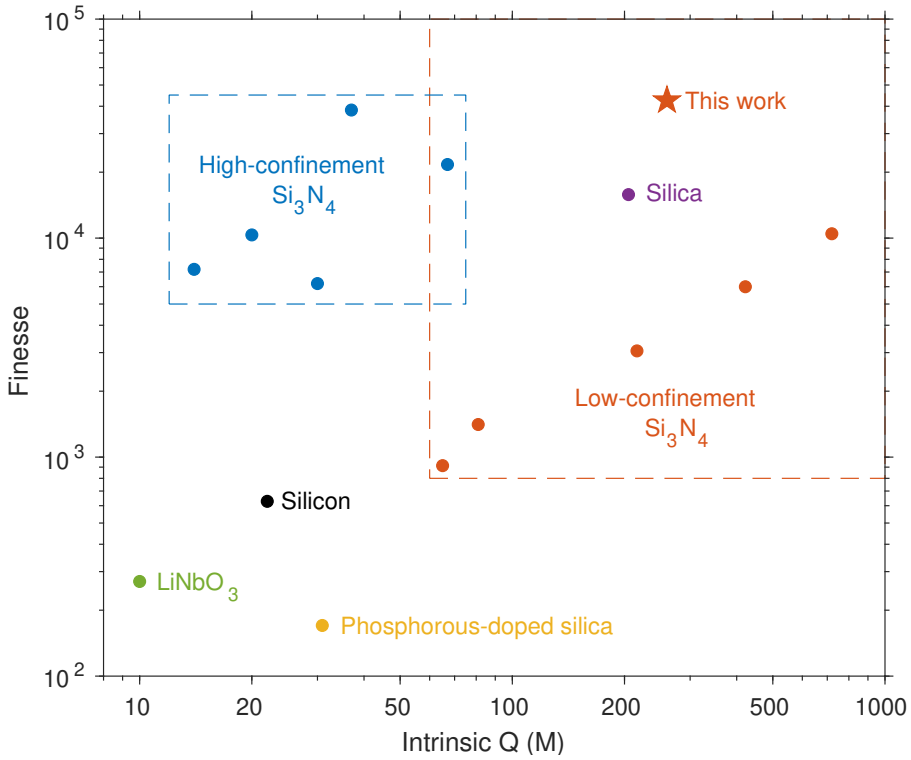

Figure 3.9: **Comparison of finesse and intrinsic Q factors** of state-of-the-art integrated microresonators. Referenced works for low-confinement Si_3N_4 are [1, 5, 3, 4, 11, 12]. Referenced works for high-confinement Si_3N_4 are [10, 13, 14, 15]. Referenced work for silica is [9]. Referenced work for silicon is [16]. Referenced work for $LiNbO_3$ is [17]. Referenced work for phosphorous-doped silica is [18]. Based on a similar figure from [1].

scale device geometry, record-high finesse, and extremely high Q factor for integrated devices. These results unveil a new regime of scalable, high-performance integrated photonic circuits that was relatively unexplored in prior work. The following chapters seek to leverage this capability to demonstrate novel photonic devices with superior performance, and with the potential for future large-scale manufacturing.

With the goal of further reduction of the propagation loss in this platform, we expect future work to identify the specific sources of propagation loss. Though the predominant source of propagation loss appears to be scattering, to what degree this scattering originates from the interface of silicon nitride and silicon dioxide, or from the bulk is not certain. Such sources of loss could be probed indirectly by fabricating waveguides with varying cross-sectional geometry, and interrogating waveguide modes with different geometry and confinement factors. Finally, for photonic integrated circuits for which the utmost performance is critical, we expect that selecting an operating wavelength further into the infra-red may yield further reduction in propagation loss. The use of 1550 nm wavelength in fiber is governed by its location at the minimum of the loss as limited by Rayleigh scattering and the Urbach tail of the SiO_2 atomic absorption [19]. For integrated photonics, in which scattering losses are many orders of magnitude higher than in fiber, the optimal wavelength to minimize propagation loss is likely at 2000 nm or beyond. The potential availability of III-V light sources in this regime, with the further possibility of heterogeneous integration [20, 21], make this a potentially fruitful direction.

Bibliography

[1] W. Jin, Q.-F. Yang, L. Chang, B. Shen, H. Wang, M. A. Leal, L. Wu, M. Gao, A. Feshali, M. Paniccia, *et. al.*, *Hertz-linewidth semiconductor lasers using*

CMOS-ready ultra-high-Q microresonators, *Nature Photonics* **15** (2021), no. 5 346–353.

[2] J. F. Bauters, M. J. Heck, D. D. John, J. S. Barton, C. M. Bruinink, A. Leinse, R. G. Heideman, D. J. Blumenthal, and J. E. Bowers, *Planar waveguides with less than 0.1 dB/m propagation loss fabricated with wafer bonding*, *Optics Express* **19** (2011), no. 24 24090–24101.

[3] D. T. Spencer, J. F. Bauters, M. J. Heck, and J. E. Bowers, *Integrated waveguide coupled Si_3N_4 resonators in the ultrahigh-Q regime*, *Optica* **1** (2014), no. 3 153–157.

[4] S. Gundavarapu, G. M. Brodnik, M. Puckett, T. Huffman, D. Bose, R. Behunin, J. Wu, T. Qiu, C. Pinho, N. Chauhan, *et. al.*, *Sub-Hertz fundamental linewidth photonic integrated Brillouin laser*, *Nature Photonics* **13** (2019), no. 1 60–67.

[5] M. W. Puckett, J. Wang, D. Bose, G. M. Brodnik, J. Wu, K. Nelson, and D. J. Blumenthal, *Silicon nitride ring resonators with 0.123 dB/m loss and Q-factors of 216 million for nonlinear optical applications*, in *Proc. CLEO/Europe'19*, p. ce_11_3, OSA, 2019.

[6] T. Kippenberg, S. Spillane, and K. Vahala, *Modal coupling in traveling-wave resonators*, *Optics letters* **27** (2002), no. 19 1669–1671.

[7] M. L. Gorodetsky, A. D. Pryamikov, and V. S. Ilchenko, *Rayleigh scattering in high-Q microspheres*, *JOSA B* **17** (2000), no. 6 1051–1057.

[8] B. J. Soller, D. K. Gifford, M. S. Wolfe, and M. E. Froggatt, *High resolution optical frequency domain reflectometry for characterization of components and assemblies*, *Optics express* **13** (2005), no. 2 666–674.

[9] K. Y. Yang, D. Y. Oh, S. H. Lee, Q.-F. Yang, X. Yi, B. Shen, H. Wang, and K. Vahala, *Bridging ultrahigh-Q devices and photonic circuits*, *Nature Photonics* **12** (2018), no. 5 297–302.

[10] X. Ji, F. A. Barbosa, S. P. Roberts, A. Dutt, J. Cardenas, Y. Okawachi, A. Bryant, A. L. Gaeta, and M. Lipson, *Ultra-low-loss on-chip resonators with sub-milliwatt parametric oscillation threshold*, *Optica* **4** (2017), no. 6 619–624.

[11] M. W. Puckett, K. Liu, N. Chauhan, Q. Zhao, N. Jin, H. Cheng, J. Wu, R. O. Behunin, P. T. Rakich, K. D. Nelson, *et. al.*, *422 million intrinsic quality factor planar integrated all-waveguide resonator with sub-MHz linewidth*, *Nature communications* **12** (2021), no. 1 1–8.

[12] K. Liu, N. Jin, H. Cheng, M. W. Puckett, R. O. Behunin, K. D. Nelson, P. T. Rakich, and D. J. Blumenthal, *720 million quality factor integrated all-waveguide photonic resonator*, in *2021 Device Research Conference (DRC)*, pp. 1–2, IEEE, 2021.

[13] J. Liu, G. Huang, R. N. Wang, J. He, A. S. Raja, T. Liu, N. J. Engelsen, and T. J. Kippenberg, *High-yield, wafer-scale fabrication of ultralow-loss, dispersion-engineered silicon nitride photonic circuits*, *Nature communications* **12** (2021), no. 1 1–9.

[14] Z. Ye, K. Twayana, P. A. Andrekson, *et. al.*, *High-Q si_3n_4 microresonators based on a subtractive processing for Kerr nonlinear optics*, *Optics express* **27** (2019), no. 24 35719–35727.

[15] Q. Li, A. A. Eftekhar, M. Sodagar, Z. Xia, A. H. Atabaki, and A. Adibi, *Vertical integration of high-Q silicon nitride microresonators into silicon-on-insulator platform*, *Optics express* **21** (2013), no. 15 18236–18248.

[16] A. Biberman, M. J. Shaw, E. Timurdogan, J. B. Wright, and M. R. Watts, *Ultralow-loss silicon ring resonators*, *Optics letters* **37** (2012), no. 20 4236–4238.

[17] M. Zhang, C. Wang, R. Cheng, A. Shams-Ansari, and M. Lončar, *Monolithic ultra-high-Q lithium niobate microring resonator*, *Optica* **4** (2017), no. 12 1536–1537.

[18] R. Adar, M. Serbin, and V. Mizrahi, *Less than 1 dB per meter propagation loss of silica waveguides measured using a ring resonator*, *Journal of lightwave technology* **12** (1994), no. 8 1369–1372.

[19] G. A. Thomas, B. I. Shraiman, P. F. Glodis, and M. J. Stephen, *Towards the clarity limit in optical fibre*, *Nature* **404** (2000), no. 6775 262–264.

[20] A. Spott, M. Davenport, J. Peters, J. Bovington, M. J. Heck, E. J. Stanton, I. Vurgaftman, J. Meyer, and J. Bowers, *Heterogeneously integrated 2.0 μm cw hybrid silicon lasers at room temperature*, *Optics letters* **40** (2015), no. 7 1480–1483.

[21] A. Spott, J. Peters, M. L. Davenport, E. J. Stanton, C. D. Merritt, W. W. Bewley, I. Vurgaftman, C. S. Kim, J. R. Meyer, J. Kirch, *et. al.*, *Quantum cascade laser on silicon*, *Optica* **3** (2016), no. 5 545–551.

Chapter 4

Ultra-narrow linewidth lasers

This section presents the application of high Q factor devices discussed in the previous chapter to creating highly coherent lasers. The benefits of high coherence lasers extend to many applications. Hertz-level linewidth is required to interrogate and manipulate atomic transitions with long coherence times, which form the basis of optical atomic clocks [1, 2]. Furthermore, linewidth directly impacts performance in optical sensing and signal generation applications, such as laser gyroscopes [3, 4], light detection and ranging (LIDAR) systems [5, 6], spectroscopy [7], optical frequency synthesis [8], microwave photonics [9, 10, 11, 12, 13], and coherent optical communications[14, 15]. In considering the future transfer of such high coherence technologies to a mass manufacturable form, semiconductor laser sources represent the most compelling choice. They are directly electrically pumped, wafer-scale manufacturable and capable of complex integration with other photonic devices. Indeed, their considerable advantages have made them into a kind of 'photonic engine' for nearly all modern day optical source technology, including commercial benchtop laser sources. Nonetheless, mass manufacturable semiconductor lasers, such as used in communications systems, have linewidths ranging from 100 kHz to a few MHz [14], which is many orders of magnitude too large for the above mentioned ap-

plications. This section presents advances in the state-of-the-art of integrated photonics, combining conventional DFB laser diodes with integrated, ultra-low loss, silicon nitride resonators in a self-injection-locking scheme. The hybrid-integrated lasers realized with this approach attain instantaneous linewidths well below 1 Hz, and overall frequency noise performance at or beyond the level of high-performance, commercial fiber lasers.

The contents of this chapter were originally published in [16, 17].

4.1 Self injection locking

Recent advances have revealed a pathway towards ultra-narrow linewidth on-a-chip by self-injection-locking (SIL) integrated lasers to ultra-high Q microresonators [18, 16, 19]. Compared to other means of laser stabilisation, such as Pound-Drever-Hall locking of a laser to a reference cavity, SIL is well suited to integrated photonics due to its simplicity. Coupling a diode laser chip to a silicon nitride chip in a hybrid [18, 16, 20, 21, 22] or heterogeneous [19] integration scheme stabilises the laser without extraneous hardware such as electronic control circuitry, modulators, or isolators. In self-injection locking, surface and bulk inhomogeneities in the resonator lead to backscattering. When the laser frequency is aligned sufficiently close to a resonance frequency, the optical field reflected from within the resonator provides feedback to spontaneously align the laser to the resonance, dramatically reducing the laser linewidth [23, 24, 25, 26].

The amount of noise reduction in self-injection locked laser depends on the spectral response and power of the backscattered field, which has been derived in the supplement to [16], based on a theory involving both laser and microresonator dynamics [25]. In particular, the magnitude of the backscattering coefficient, β, compared to the cavity linewidth, $1/(2\tau)$, as defined in Equation 2.13 determines the behavior. In the case of weak backscattering ($\beta \ll 1/(2\tau)$), i.e., the resonator mode remains as a singlet, and the

laser frequency noise can be reduced by the noise reduction factor, NRF [16]:

$$\mathrm{NRF} \approx 256(1+\alpha^2)T^2\eta^2\tau^2|\beta|^2\frac{Q_\mathrm{R}^2}{Q_\mathrm{d}^2}, \tag{4.1}$$

where Q_R and Q_d stand for the Q of the microresonator and the laser diode, respectively. $\eta = Q_\mathrm{R}/Q_\mathrm{e}$ is the microresonator loading factor with Q_e being the coupling Q between the bus waveguide and the resonator. T denotes the power insertion loss between the facets of the laser and the bus waveguide, while α is the amplitude-phase coupling coefficient of the laser. In the presence of a strong backscattered field ($\beta \gg 1/(2\tau)$), i.e., the mode splits into doublets, the NRF is saturated as [16]

$$\mathrm{NRF} \approx 4(1+\alpha^2)T^2\eta^2\frac{Q_\mathrm{R}^2}{Q_\mathrm{d}^2}, \tag{4.2}$$

which is independent of the backscattering coefficient.

The self-injection-locking setup comprises a commercial DFB laser butt-coupled to the bus waveguide of the Si_3N_4 resonator chip. A schematic of the setup is shown in Figure 4.1a. The laser chip is powered by an ultra-low-noise current source (ILX Lightwave LDX-3620B) and is mounted on a thermoelectric cooler to avoid long-term drift, is able to deliver power up to 30 mW at 1556 nm into the Si_3N_4 bus waveguide. Optical feedback is provided to the laser by backward Rayleigh scattering in the microresonator, which spontaneously aligns the laser frequency to the nearest resonator mode. As the phase accumulated in the feedback is critical to determining the stability of injection-locking [25, 18, 27], we precisely control the feedback phase by adjusting the air gap between the chips. In the case of a rigidly co-packaged laser and resonator, feedback phase control may instead be achieved by the addition of a resistive heater to the waveguide linking the laser and resonator. The laser output is taken through the bus waveguide of the

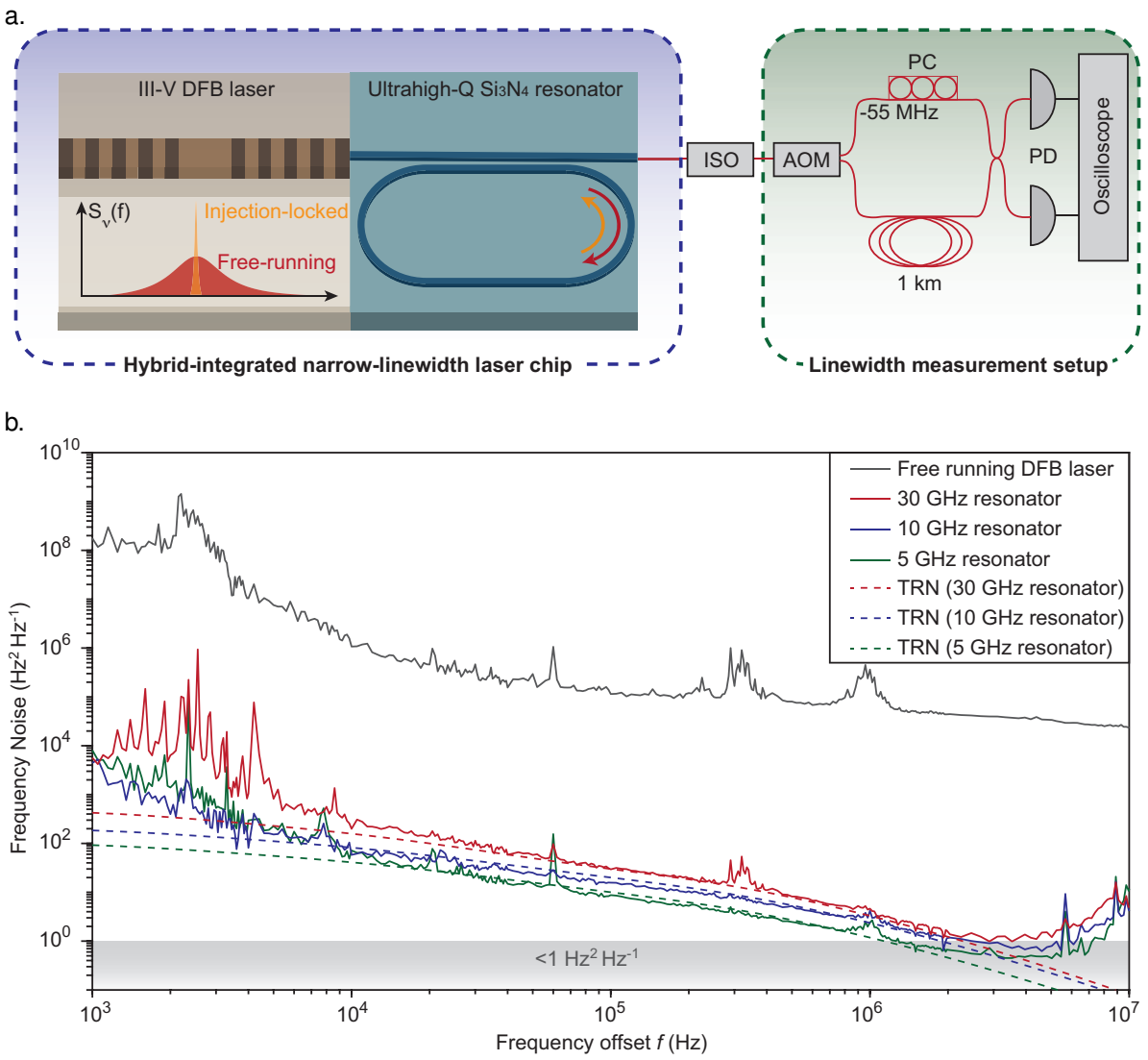

Figure 4.1: **Hybrid-integrated narrow-linewidth laser based on ultra-high-Q Si_3N_4 microresonator.** (a) Schematic of the hybrid laser design (not to scale) and frequency noise test setup. The red (yellow) arrow denotes the forward (backscattered) light field. ISO: optical isolator; AOM: acousto-optic modulator; PC: polarization controller; PD: photodetector. (b) Measurement of single-sideband frequency noise of the free-running and self-injection locked DFB laser with various resonators. The minimum frequency-noise levels are 1 Hz^2 Hz^{-1}, 0.8 Hz^2 Hz^{-1}, 0.5 Hz^2 Hz^{-1} for resonators with 30 GHz, 10 GHz and 5 GHz FSR, respectively. The dashed lines give the simulated thermorefractive noise (TRN). Reproduced from [16].

microresonator, and directed to a self-heterodyne setup for frequency noise characterization. Two photodetectors and a cross-correlation technique are used to improve detection sensitivity [28, 16].

The frequency noise spectra of the self-injection locked laser system using the 30 GHz ring and the 10 GHz and 5 GHz racetrack resonators (respective intrinsic Q factors of 250 M, 56 M and 100 M) are compared in Figure 4.1b. The ultra-high-Q factors enable the frequency noise of the free-running DFB laser to, in principle, be suppressed by up to 80 dB. In practice, however, the noise suppression over a broad range of offset frequencies (10 kHz to 2 MHz) is limited to 50 dB by the presence of thermorefractive noise [29, 30, 31] in the microresonator. Consistent with theory, microresonators with larger mode volume, i.e. smaller FSR, experience a lower thermorefractive fluctuation and exhibit reduced frequency noise (Figure 4.1b). At low frequency offset (below 10 kHz), frequency noise is primarily limited by temperature drift and coupling stability between chips. This can be suppressed by improved device packaging. At high offset frequencies (above 5 MHz), frequency noise rises with the square of offset frequency, as the maximum noise suppression bandwidth of injection locking is limited to the bandwidth of the resonator [24, 32, 16]. Thus, minimum frequency noise below 1 $\text{Hz}^2\ \text{Hz}^{-1}$ is observed at about 5 MHz offset frequency, where the contributions of rising laser noise and falling thermorefractive noise are approximately equal.

However, the bandwidth of limitation of self-injection locking can be overcome by including an additional waveguide coupler, called a drop port, and taking the laser output that has passed through the ring itself [33]. This configuration is shown in a schematic in Figure 4.2a. While the self-injection locking bandwidth is limited to the resonator linewidth, beyond the resonator's linewidth the resonator itself can provide low-pass filtering on the frequency noise. The impact of this filtering is explored theoretically in the supplement to [16]. As shown in Figure 4.2b, the noise reduction factor at the

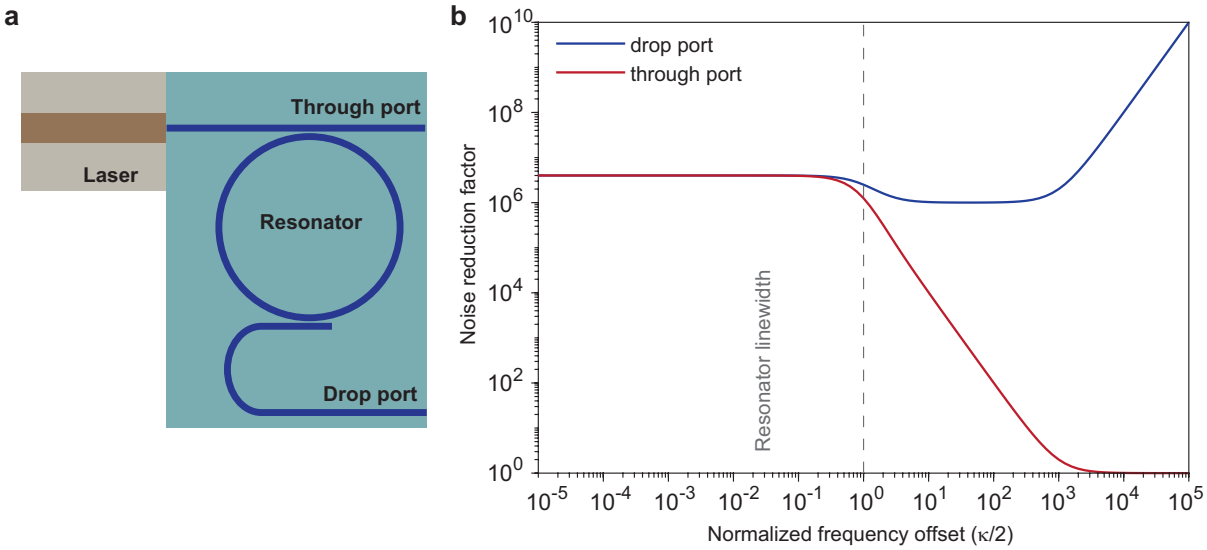

Figure 4.2: **Spectral dependence of noise reduction factor.** (a) Configuration of a laser butt-coupled to a microresonator with add-drop port. (b) Calculated noise reduction factor of laser emission from through (red) and drop (blue) port. The frequency offset is normalized to $\kappa/2$, one half of resonator linewidth. Reproduced from [16].

through port declines beyond the resonator linewidth, but the filtering action at the drop port allows the system to retain a high noise reduction factor at higher offset frequency as well. However, this model does not include the adjacent longitudinal modes of the resonator, and a reduced noise reduction factor would be expected at offset frequencies corresponding to the resonator FSR.

To demonstrate the drop-port filtering effect experimentally, the self-injection-locking experiment was repeated using a resonator featuring a drop port (Figure 4.3a). This configuration yields an ultra-low, white frequency-noise floor of 0.2 Hz^2 Hz^{-1} at high offset frequencies, corresponding to a short-term linewidth of 1.2 Hz (Figure 4.3b).

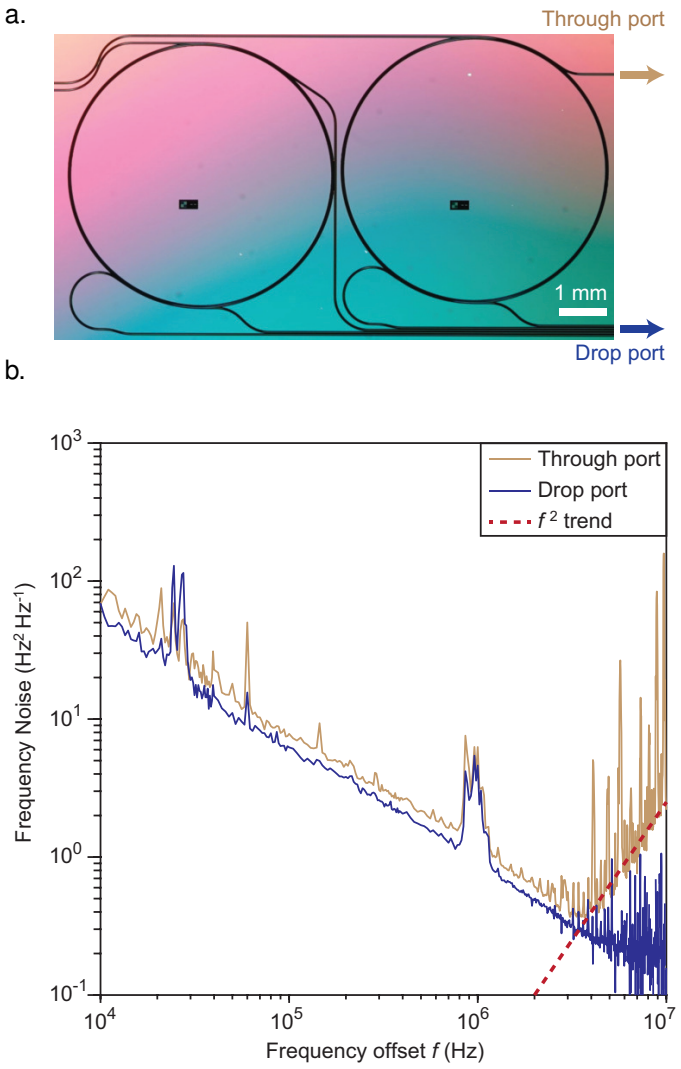

Figure 4.3: **Self-injection locking with drop port.** (a) Photograph of a 10.8 GHz FSR ring resonator fabricated with a drop port. (b) A comparison of single sideband frequency noise measured from the through port and drop port of the same device. The drop port enables the resonator itself to act as a low-pass filter, yielding a white-noise floor of 0.2 Hz^2 Hz^{-1}. Reproduced from [16].

4.2 Large mode-volume spiral resonators

As the frequency noise level is limited by thermorefractive noise over a range of offset frequencies spanning from 10 kHz to over 1 MHz, any further reduction in the thermorefractive noise should lead directly to improved frequency noise performance. Since thermorefractive noise scales inversely to the modal volume of the resonator [29, 30, 31], increasing the modal volume by fabricating spiraled resonant cavities [34] provides direct means to attain even lower frequency noise levels.

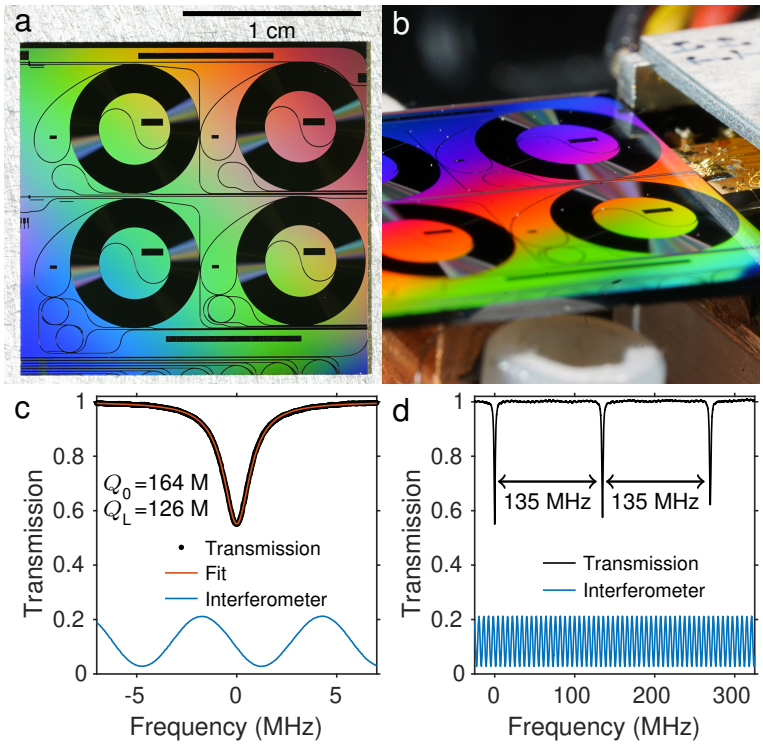

Figure 4.4: **Spiraled Resonators for self injection locking.** (a) Photograph of 1.41 m round-trip-length spiral resonators. Each resonator occupies a 9.2 mm×7.2 mm footprint. The chip features four independent, identical resonators, each designed with a different coupling strength (b) Photograph of self-injection-locking (SIL) setup. (c) The transmission spectrum of a 1.41 m resonator with the measured intrinsic (Q_0=164) and loaded (Q_L=125.9±0.2) Q-factor values indicated. An average propagation loss of 0.17 dB/m within the resonator is implied by Q_0. Intrinsic Q factor is calculated assuming the coupling rate of the drop port is 0.7 of the through port, inferred from the design. (d) Transmission spectrum showing FSR of 135 MHz (134.73 ± 0.01 MHz) at 1551 nm. Reproduced from [17].

To achieve large mode volume in a compact footprint, we design spiraled resonators [34] featuring a 100 nm thick silicon nitride core, 2.2 μm thick tetraethyl-orthosilicate (TEOS) -based silicon dioxide top cladding, and 14.5 μm thick thermally oxidized silicon dioxide bottom cladding. The devices (pictured in Figure 4.4a) were fabricated on 200 mm silicon wafers in a CMOS foundry [16]. Each resonator is drawn from two identical Archimedes spirals [35] with 40 μm pitch and minimum bend radius of 2 mm. The two spirals share a common center of curvature, and are interleaved by rotating one spiral by 180° with respect to the other. The resonator is formed by linking interior and exterior spiral endpoints with adiabatically curved transitions [36] with 0.9 mm minimum bend radius, drawn to precisely match direction and curvature with the spiral endpoints. Each adiabatic transition maintains 2.8 μm single-mode-waveguide width to prevent coupling to higher-order modes, while the waveguides widen to 10 μm waveguide width within the Archimedes spirals to minimize propagation loss. Two couplers are drawn along the outermost loop of the spiral to allow the SIL laser output to be taken from the drop-port, and thereby filter out high-offset frequency noise [16]. Resonators featuring round-trip length of 1.41 m (shown in Fig. 4.4a) and 0.312 m length (not pictured) were fabricated, with free spectral range of 135 MHz and 610 MHz, respectively. Intrinsic and loaded Q factors as well as the FSR are measured for each resonator using a tunable laser, with tuning rate calibrated by a fiber interferometer, as illustrated for the 1.41 m resonator in Fig. 4.4c and Figure 4.4d.

As shown in Figure 4.5a, single-mode lasing with large side-mode suppression ratio (SMSR) can be achieved over a wide range of pumping currents. Typical output power, collected from the drop port of the resonator, for the same range of pumping current, is shown in Figure 4.5b. At each pumping condition, the air gap between the chips is adjusted to control the feedback phase [23] to achieve single-mode lasing. Moreover, at any given pumping current, single-mode lasing can be observed at multiple distinct

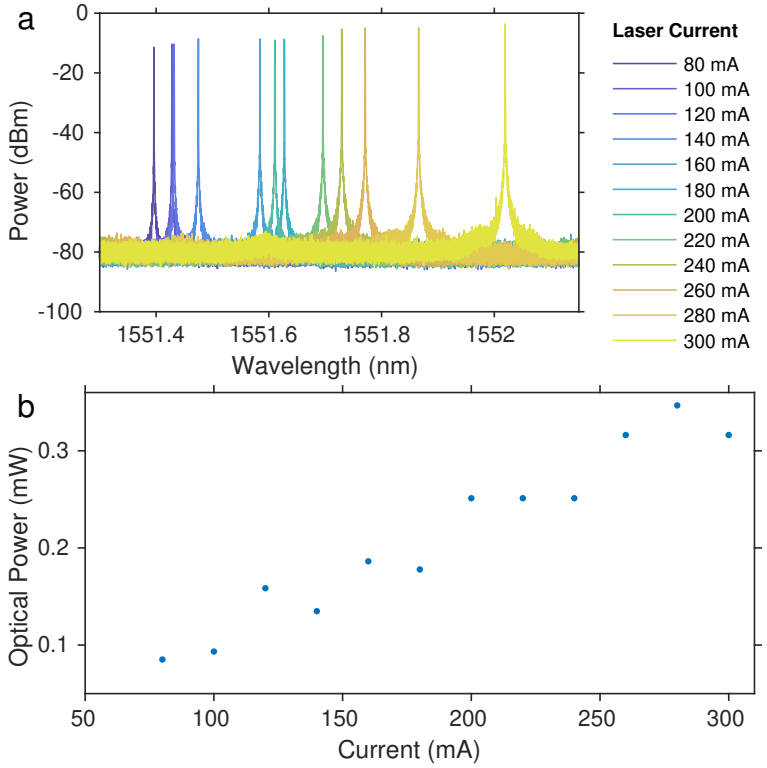

Figure 4.5: **Self injection locking conditions.** (a) Single-mode lasing with large side mode suppression ratio (SMSR) and (b) output power taken from the drop port of the SIL device (from a different scan) are shown for the 1.41 m long resonator at a series of pumping currents to the distributed feedback (DFB) laser. The data in (a) are collected using an optical spectrum analyzer (OSA) with 5 MHz resolution bandwidth (Apex AP2051A) in order to confirm single-mode operation. Reproduced from [17].

wavelengths depending on feedback phase. As a result, the wavelengths in Figure 4.5a and power in Figure 4.5b do not increase monotonically with the driving current, as they would in a free-running DFB laser. We note that below 80 mA, single-mode lasing could not be achieved for any feedback phase. Details of the single-mode lasing condition in the DFB-spiral system are under further study. Although the laser chip is mounted on a thermoelectric cooler, the spiral resonator is not temperature stabilized. Also, the air gap is not feedback stabilized. We believe that drift in the feedback phase and ambient temperature contribute to occasional mode hops between adjacent resonances of the resonator that were observed to occur on a time scale of approximately one hour. These factors could be addressed by packaging the device to improve thermal and mechanical stability [37]. In a packaged device, as the gap between chips would no longer be adjustable, a resistive heater [19] placed between the resonator and laser could be used instead to tune the feedback phase by the thermo-optic effect.

The frequency noise (FN) of the DFB laser self-injection-locked to the spiral resonators is shown in Figure 4.6a. A commercial FN tester (OE4000) is used to measure FN below 10 kHz offset frequency. We combine this with a self-heterodyne cross-correlation method [28, 16] with higher sensitivity at offset frequency above 10 kHz. To explore the dependence on mode volume, we also measure the FN of the DFB laser self-injection locked to 30 GHz, 10 GHz, and 5 GHz FSR resonators studied in prior work [16]. The FN of these devices rises at high offset frequency (>2 MHz) due to their through-port configuration, as the frequency noise reduction factor decreases for offset frequency beyond the resonator's resonance bandwidth [24]. However, the spiral resonators exhibit flat FN reduction factor at high offset frequency [16] due to their drop-port configuration. We note that the noise spectrum for the FSR=135 MHz spiral device rises for offset frequencies above 4 MHz due to reaching the measurement-limited noise floor. FN below 10kHz offset is strongly influenced by environmental perturbations, and could be

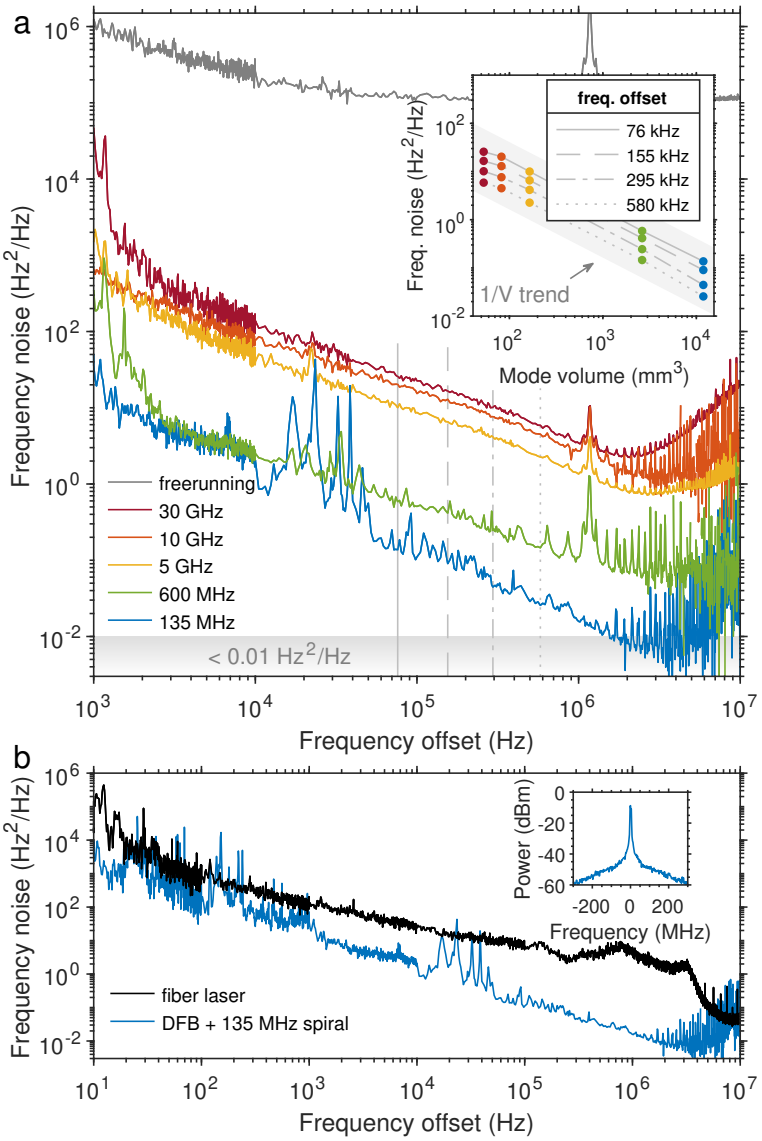

Figure 4.6: **Self injection locking frequency noise.** (a) Single-sideband frequency noise (FN) spectra of the DFB laser in free-running state, as well as in the SIL mode to resonators of various FSR. Vertical lines indicate the frequency offsets selected in the inset. Inset: FN versus mode volume at offset frequencies selected to avoid noise spurs and reveal the TRN floor. (b) FN comparison of a high-performance fiber laser to the SIL DFB laser using a 135 MHz spiral resonator. Inset: high-resolution optical spectrum of SIL DFB laser. Reproduced from [17].

reduced by packaging, as discussed above. In the 10 kHz to 1 MHz range, we expect the FN to be dominated by thermorefractive contributions. In the inset, FN is plotted versus resonator mode volume, V, at selected offset frequencies. The data show strong agreement with the expected $1/V$ trend of TRN [38].

As shown in Figure 4.6b, the FN of the DFB self-injection-locked to the 135 MHz spiral is comparable to or better than a high-performance fiber laser (Orbits Ethernal) over a wide range of offset frequencies. At high offset frequency, it outperforms the fiber laser by over an order of magnitude, reaching 0.006 Hz^2/Hz at 4 MHz, corresponding to Lorentzian linewidth [16] below 40 mHz. Remarkably, the hybrid laser exhibits stability comparable to the fiber laser in the 100 Hz to 10 kHz frequency offset range as well, with a frequency noise level of 200 Hz^2/Hz at 100 Hz offset. In all configurations, we confirm single-mode operation of the SIL laser (Figure 4.6b inset) using a high resolution (5 MHz resolution bandwidth) optical spectrum analyzer. We note that the noise spurs around 1 MHz offset, present in certain measurements, come from the pump current source, and are absent when using a different current source of the same model.

4.3 Performance comparison

Finally, we compare the current hybrid-integrated laser linewidths to state-of-the-art results in Table 4.1. The linewidth of monolithic III-V lasers is generally limited to the 100 kHz to 1 MHz range by passive waveguide losses well above 1 dB cm^{-1}, with best demonstrated linewidth below 100 kHz [39]. Phase and amplitude noise scale according to the square of cavity losses [24, 25]. Thus, hybrid integration, where the active III-V and passive photonic chips are assembled post-fabrication, and heterogeneous integration [40], where III-V material is directly bonded to the passive chip during fabrication, have emerged as primary technologies to create narrow-linewidth integrated lasers. As shown

Table 4.1: **Integrated Laser Comparison.** Linewidth of best-to-date integrated narrow-linewidth lasers. Based on a similar table from [16].

Operating principle	**Configuration**	**Instantaneous Linewidth (Hz)**	**Ref**
Self-injection locking (this work)	Hybrid III-V/Si_3N_4	0.04	[17]
Self-injection locking (this work)	Hybrid III-V/Si_3N_4	1.2	[16]
Self-injection locking	Heterogeneous III-V/Si_3N_4	25	[19]
Self-injection locking	Hybrid III-V/Si_3N_4	25	[20]
External Cavity	Hybrid III-V/Si_3N_4	40	[41]
External Cavity	Heterogeneous III-V/Si	140	[42]
External Cavity	Heterogeneous III-V/Si_3N_4	4,000	[43]
External Cavity	Monolithic III-V	50,000	[39]

in Table 4.1, hybrid and heterogeneous integration can produce linewidth well below 1 kHz. The best instantaneous linewidth demonstrated is below 0.04 Hz [17], limited by the measurement noise floor. This substantially improves upon the 1.2 Hz linewidth we demonstrated with smaller mode-volume resonators [16]. Furthermore, both results are more than an order of magnitude better than the best results to date [41, 19, 20]. Additionally, the integrated linewidth, $\Delta\nu$, calculated as follows [24, 42],

$$\int_{\Delta\nu}^{\infty} \frac{S_\nu(f)}{f^2}\, df = \frac{1}{\pi}\text{rad}^2 \tag{4.3}$$

yields an integrated linewidth of 280 Hz, which is the lowest such linewidth demonstrated for any chip-scale laser. These results compare favorably to results achieved in non-integrated systems as well. Besides our earlier comparison to a commercial fiber laser, the achieved instantaneous linewidth below 0.04 Hz also surpasses the 0.1 Hz linewidth using non-planar crystalline resonators [37], achieved by self-injection locking.

Discussion

In conclusion, we self-injection-lock a DFB laser to high Q resonators with various mode volume, achieving frequency noise at the thermorefractive noise limit. The resulting devices have outstanding frequency noise characteristics capable of exceeding those of a high performance fiber laser. These hybrid-integrated devices are readily applicable to many coherent optical systems. For example, while laboratory communication experiments pursuing spectral efficiency approaching 20 bit s^{-1} Hz^{-1} rely on high performance single-frequency fiber lasers [15], narrow-linewidth integrated photonic comb lasers could accelerate the adoption of similar schemes in practical data-center and metro links [44, 45, 46, 47, 48, 18]. Microwave photonics [9, 10, 11, 12, 13], atomic clocks [1, 2], and quantum information [49] will also benefit greatly from the reduced size, weight, power and cost provided by the combination of ultra-high Q and photonic integration.

Many improvements beyond the results presented here are feasible. We infer propagation loss of 0.1 dB m^{-1}, however, lower loss of 0.045 dB m^{-1} is feasible in thinner cores [50], suggesting that the limits of Q for this platform have not been fully explored. Finally, heterogeneous integration of III-V lasers and ultra-high-Q microresonators may eventually unite the device onto a single substrate [42, 43, 40], enabling the production of mass-manufactured laser sources with fiber-laser-equivalent coherence on chip.

Bibliography

[1] A. D. Ludlow, M. M. Boyd, J. Ye, E. Peik, and P. O. Schmidt, *Optical atomic clocks*, *Rev. Mod. Phys.* **87** (2015), no. 2 637.

[2] Z. L. Newman, V. Maurice, T. Drake, J. R. Stone, T. C. Briles, D. T. Spencer,

C. Fredrick, Q. Li, D. Westly, B. R. Ilic, *et. al.*, *Architecture for the photonic integration of an optical atomic clock*, *Optica* **6** (2019), no. 5 680–685.

[3] S. Gundavarapu, G. M. Brodnik, M. Puckett, T. Huffman, D. Bose, R. Behunin, J. Wu, T. Qiu, C. Pinho, N. Chauhan, *et. al.*, *Sub-Hertz fundamental linewidth photonic integrated Brillouin laser*, *Nature Photonics* **13** (2019), no. 1 60–67.

[4] Y.-H. Lai, M.-G. Suh, Y.-K. Lu, B. Shen, Q.-F. Yang, H. Wang, J. Li, S. H. Lee, K. Y. Yang, and K. Vahala, *Earth rotation measured by a chip-scale ring laser gyroscope*, *Nat. Photon.* **14** (2020) 345–349.

[5] P. Trocha, M. Karpov, D. Ganin, M. H. Pfeiffer, A. Kordts, S. Wolf, J. Krockenberger, P. Marin-Palomo, C. Weimann, S. Randel, *et. al.*, *Ultrafast optical ranging using microresonator soliton frequency combs*, *Science* **359** (2018), no. 6378 887–891.

[6] M.-G. Suh and K. J. Vahala, *Soliton microcomb range measurement*, *Science* **359** (2018), no. 6378 884–887.

[7] M.-G. Suh, Q.-F. Yang, K. Y. Yang, X. Yi, and K. J. Vahala, *Microresonator soliton dual-comb spectroscopy*, *Science* **354** (2016), no. 6312 600–603.

[8] D. T. Spencer, T. Drake, T. C. Briles, J. Stone, L. C. Sinclair, C. Fredrick, Q. Li, D. Westly, B. R. Ilic, A. Bluestone, *et. al.*, *An optical-frequency synthesizer using integrated photonics.*, *Nature* **557** (2018), no. 7703 81–85.

[9] J. Li, H. Lee, and K. J. Vahala, *Microwave synthesizer using an on-chip brillouin oscillator*, *Nat. Commun.* **4** (Oct, 2013) 2041–1723.

[10] W. Liang, D. Eliyahu, V. Ilchenko, A. Savchenkov, A. Matsko, D. Seidel, and

L. Maleki, *High spectral purity Kerr frequency comb radio frequency photonic oscillator*, *Nat. Commun.* **6** (2015) 7957.

[11] T. Hao, J. Tang, D. Domenech, W. Li, N. Zhu, J. Capmany, and M. Li, *Toward monolithic integration of OEOs: From systems to chips*, *J. Light. Technol.* **36** (2018), no. 19 4565–4582.

[12] D. Marpaung, J. Yao, and J. Capmany, *Integrated microwave photonics*, *Nat. Photon.* **13** (2019), no. 2 80–90.

[13] J. Liu, E. Lucas, A. S. Raja, J. He, J. Riemensberger, R. N. Wang, M. Karpov, H. Guo, R. Bouchand, and T. J. Kippenberg, *Photonic microwave generation in the X-and K-band using integrated soliton microcombs*, *Nat. Photon.* (2020).

[14] K. Kikuchi, *Fundamentals of coherent optical fiber communications*, *J. Light. Technol.* **34** (2015), no. 1 157–179.

[15] S. L. Olsson, J. Cho, S. Chandrasekhar, X. Chen, P. J. Winzer, and S. Makovejs, *Probabilistically shaped PDM 4096-QAM transmission over up to 200 km of fiber using standard intradyne detection*, *Opt. Express* **26** (2018), no. 4 4522–4530.

[16] W. Jin, Q.-F. Yang, L. Chang, B. Shen, H. Wang, M. A. Leal, L. Wu, M. Gao, A. Feshali, M. Paniccia, *et. al.*, *Hertz-linewidth semiconductor lasers using CMOS-ready ultra-high-Q microresonators*, *Nature Photonics* **15** (2021), no. 5 346–353.

[17] B. Li, W. Jin, L. Wu, L. Chang, H. Wang, B. Shen, Z. Yuan, A. Feshali, M. Paniccia, K. J. Vahala, *et. al.*, *Reaching fiber-laser coherence in integrated photonics*, *Optics Letters* **46** (2021), no. 20 5201–5204.

[18] B. Shen, L. Chang, J. Liu, H. Wang, Q.-F. Yang, C. Xiang, R. N. Wang, J. He, T. Liu, W. Xie, J. Guo, D. Kinghorn, L. Wu, Q.-X. Ji, T. J. Kippenberg, K. J. Vahala, and J. E. Bowers, *Integrated turnkey soliton microcombs*, *Nature* **582** (2020), no. 7812 365–369.

[19] C. Xiang, J. Liu, J. Guo, L. Chang, R. N. Wang, W. Weng, J. Peters, W. Xie, Z. Zhang, J. Riemensberger, J. Selvidge, T. J. Kippenberg, and J. E. Bowers, *Laser soliton microcombs heterogeneously integrated on silicon*, *Science* **373** (2021), no. 6550 99–103, [https://science.sciencemag.org/content/373/6550/99.full.pdf].

[20] G. Lihachev, J. Riemensberger, W. Weng, J. Liu, H. Tian, A. Siddharth, V. Snigirev, R. N. Wang, J. He, S. A. Bhave, and T. J. Kippenberg, *Ultralow-noise frequency-agile photonic integrated lasers*, 2021.

[21] R. Oldenbeuving, E. Klein, H. L. Offerhaus, C. J. Lee, H. Song, and K. J. Boller, *25 khz narrow spectral bandwidth of a wavelength tunable diode laser with a short waveguide-based external cavity*, *Laser Phys. Lett.* **10** (2012), no. 1 015804.

[22] Y. Fan, J. P. Epping, R. M. Oldenbeuving, C. G. Roeloffzen, M. Hoekman, R. Dekker, R. G. Heideman, P. J. van der Slot, and K.-J. Boller, *Optically integrated inp–si _3 n _4 hybrid laser*, *IEEE Photonics J.* **8** (2016), no. 6 1–11.

[23] B. Dahmani, L. Hollberg, and R. Drullinger, *Frequency stabilization of semiconductor lasers by resonant optical feedback*, *Opt. Lett.* **12** (1987), no. 11 876–878.

[24] D. R. Hjelme, A. R. Mickelson, and R. G. Beausoleil, *Semiconductor laser stabilization by external optical feedback*, *IEEE J. Quantum Electron.* **27** (1991), no. 3 352–372.

[25] N. Kondratiev, V. Lobanov, A. Cherenkov, A. Voloshin, N. Pavlov, S. Koptyaev, and M. Gorodetsky, *Self-injection locking of a laser diode to a high-Q WGM microresonator*, *Opt. Express* **25** (2017), no. 23 28167–28178.

[26] A. B. Matsko, A. A. Savchenkov, N. Yu, and L. Maleki, *Whispering-gallery-mode resonators as frequency references. I. fundamental limitations*, *J. Opt. Soc. Am. B* **24** (2007), no. 6 1324–1335.

[27] A. Savchenkov, S. Williams, and A. Matsko, *On stiffness of optical self-injection locking*, in *Photonics*, vol. 5, p. 43, Multidisciplinary Digital Publishing Institute, 2018.

[28] H. Wang, L. Wu, Z. Yuan, and K. Vahala, *Towards milli-hertz laser frequency noise on a chip*, *arXiv preprint arXiv:2010.09248* (2020).

[29] N. Kondratiev and M. Gorodetsky, *Thermorefractive noise in whispering gallery mode microresonators: Analytical results and numerical simulation*, *Phys. Lett. A* **382** (2018), no. 33 2265–2268.

[30] G. Huang, E. Lucas, J. Liu, A. S. Raja, G. Lihachev, M. L. Gorodetsky, N. J. Engelsen, and T. J. Kippenberg, *Thermorefractive noise in silicon-nitride microresonators*, *Phys. Rev. A* **99** (2019), no. 6 061801.

[31] J. Lim, A. A. Savchenkov, E. Dale, W. Liang, D. Eliyahu, V. Ilchenko, A. B. Matsko, L. Maleki, and C. W. Wong, *Chasing the thermodynamical noise limit in whispering-gallery-mode resonators for ultrastable laser frequency stabilization*, *Nat. Commun.* **8** (2017), no. 1 1–7.

[32] H. Li and N. Abraham, *Analysis of the noise spectra of a laser diode with optical*

feedback from a high-finesse resonator, *IEEE J. Quantum Electron.* **25** (1989), no. 8 1782–1793.

[33] P.-H. Wang, Y. Xuan, L. Fan, L. T. Varghese, J. Wang, Y. Liu, X. Xue, D. E. Leaird, M. Qi, and A. M. Weiner, *Drop-port study of microresonator frequency combs: power transfer, spectra and time-domain characterization*, *Opt. Express* **21** (2013), no. 19 22441–22452.

[34] H. Lee, M.-G. Suh, T. Chen, J. Li, S. A. Diddams, and K. J. Vahala, *Spiral resonators for on-chip laser frequency stabilization*, *Nat. Commun.* **4** (2013), no. 1 1–6.

[35] T. Chen, H. Lee, and K. J. Vahala, *Design and characterization of whispering-gallery spiral waveguides*, *Opt. Express* **22** (2014), no. 5 5196–5208.

[36] F. Ladouceur and E. Labeye, *A new general approach to optical waveguide path design*, *J. Light. Technol.* **13** (1995), no. 3 481–492.

[37] W. Liang, V. Ilchenko, D. Eliyahu, A. Savchenkov, A. Matsko, D. Seidel, and L. Maleki, *Ultralow noise miniature external cavity semiconductor laser*, *Nat. Commun.* **6** (2015), no. 1 1–6.

[38] M. L. Gorodetsky and I. S. Grudinin, *Fundamental thermal fluctuations in microspheres*, *J. Opt. Soc. Am. B* **21** (2004), no. 4 697–705.

[39] M. Larson, A. Bhardwaj, W. Xiong, Y. Feng, X. Huang, K. Petrov, M. Moewe, H. Ji, A. Semakov, C. Lv, *et. al.*, *Narrow linewidth sampled-grating distributed Bragg reflector laser with enhanced side-mode suppression*, in *Proc. OFC'15*, pp. 1–3, IEEE, 2015.

[40] T. Komljenovic, M. Davenport, J. Hulme, A. Y. Liu, C. T. Santis, A. Spott, S. Srinivasan, E. J. Stanton, C. Zhang, and J. E. Bowers, *Heterogeneous silicon photonic integrated circuits*, *J. Light. Technol.* **34** (2016), no. 1 20–35.

[41] Y. Fan, A. van Rees, P. J. Van der Slot, J. Mak, R. M. Oldenbeuving, M. Hoekman, D. Geskus, C. G. Roeloffzen, and K.-J. Boller, *Hybrid integrated inp-si 3 n 4 diode laser with a 40-hz intrinsic linewidth*, *Opt. Express* **28** (2020), no. 15 21713–21728.

[42] M. A. Tran, D. Huang, and J. E. Bowers, *Tutorial on narrow linewidth tunable semiconductor lasers using Si/III-V heterogeneous integration*, *APL photonics* **4** (2019), no. 11 111101.

[43] C. Xiang, W. Jin, J. Guo, J. D. Peters, M. Kennedy, J. Selvidge, P. A. Morton, and J. E. Bowers, *Narrow-linewidth III-V/Si/Si_3N_4 laser using multilayer heterogeneous integration*, *Optica* **7** (2020), no. 1 20–21.

[44] P. Marin-Palomo, J. N. Kemal, M. Karpov, A. Kordts, J. Pfeifle, M. H. Pfeiffer, P. Trocha, S. Wolf, V. Brasch, M. H. Anderson, *et. al.*, *Microresonator-based solitons for massively parallel coherent optical communications*, *Nature* **546** (2017), no. 7657 274.

[45] A. Fülöp, M. Mazur, A. Lorences-Riesgo, Ó. B. Helgason, P.-H. Wang, Y. Xuan, D. E. Leaird, M. Qi, P. A. Andrekson, A. M. Weiner, *et. al.*, *High-order coherent communications using mode-locked dark-pulse Kerr combs from microresonators*, *Nat. Commun.* **9** (2018), no. 1 1–8.

[46] A. S. Raja, A. S. Voloshin, H. Guo, S. E. Agafonova, J. Liu, A. S. Gorodnitskiy, M. Karpov, N. G. Pavlov, E. Lucas, R. R. Galiev, *et. al.*, *Electrically pumped photonic integrated soliton microcomb*, *Nat. Commun.* **10** (2019), no. 1 680.

[47] B. Stern, X. Ji, Y. Okawachi, A. L. Gaeta, and M. Lipson, *Battery-operated integrated frequency comb generator*, *Nature* **562** (2018), no. 7727 401.

[48] B. Corcoran, M. Tan, X. Xu, A. Boes, J. Wu, T. G. Nguyen, S. T. Chu, B. E. Little, R. Morandotti, A. Mitchell, *et. al.*, *Ultra-dense optical data transmission over standard fibre with a single chip source*, *Nat. Commun.* **11** (2020), no. 1 1–7.

[49] S. Tanzilli, A. Martin, F. Kaiser, M. P. De Micheli, O. Alibart, and D. B. Ostrowsky, *On the genesis and evolution of integrated quantum optics*, *Laser Photonics Rev.* **6** (2012), no. 1 115–143.

[50] J. F. Bauters, M. J. Heck, D. D. John, J. S. Barton, C. M. Bruinink, A. Leinse, R. G. Heideman, D. J. Blumenthal, and J. E. Bowers, *Planar waveguides with less than 0.1 dB/m propagation loss fabricated with wafer bonding*, *Optics Express* **19** (2011), no. 24 24090–24101.

Chapter 5

Nonlinear effects

In the previous chapter, a DFB laser, self-injection-locked to ultra-high Q microresonators, was shown to be capable of producing ultra-low frequency noise, rivaling the coherence of commercial fiber lasers. Within the same configuration, a new regime of Kerr comb operation in microresonators is supported. Specifically, the comb demonstrates turnkey operation [1] as well as attaining coherent comb operation under conditions of normal dispersion, without any special dispersion engineering. The comb's line spacing is suitable for dense wavelength division multiplexed (DWDM) communications systems. Moreover, each comb line benefits from the exceptional frequency-noise performance of the disciplined pump, representing an important advance for DWDM source technology. The microwave phase noise performance of the comb is also comparable to that of existing commercial microwave oscillators.

In addition to Kerr nonlinearity, this low-loss silicon nitride platform is also demonstrated to exhibit significant Raman and Brillouin nonlinearities. The Brillouin nonlinearity is measured to be on-par with other silicon nitride results, while a novel resonator design results in a significantly enhanced mode selectivity, leading to the demonstration of a single-mode Raman laser.

The self-injection-locked Kerr comb results were originally published in [2]. The results on Raman and Brillouin nonlinearity are under preparation for publication.

5.1 Mode-locked Kerr combs

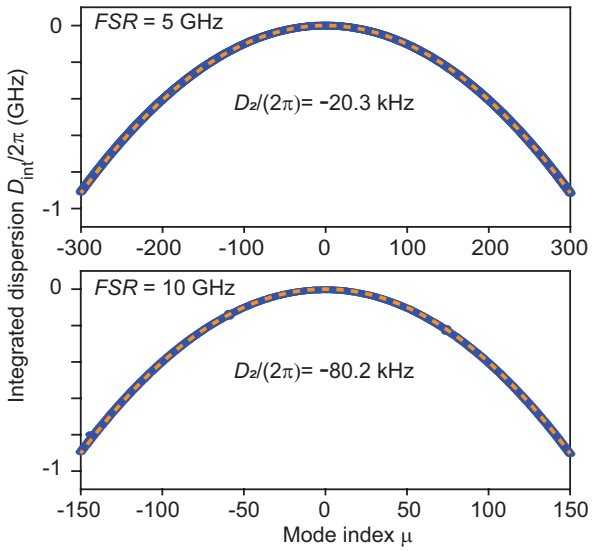

Figure 5.1: **Measured mode family dispersion** is normal. The plot shows the integrated dispersion defined as $D_{\text{int}} = \omega_\mu - \omega_o - D_1\mu$ where ω_μ is the resonant frequency of a mode with index μ and D_1 is the FSR at $\mu = 0$. The wavelength of the central mode ($\mu = 0$) is around 1550 nm. The dashed lines are parabolic fits ($D_{\text{int}} = D_2\mu^2/2$) with $D_2/2\pi$ equal to -20.3 kHz and -80.2 kHz corresponding to 5 GHz and 10 GHz FSR, respectively. Note: $D_2 = -cD_1^2\beta_2/n_{\text{eff}}$ where β_2 is the group velocity dispersion, c the speed of light and n_{eff} the effective index of the mode. Reproduced from [2].

The ultra-high Q of the microresonators enables strong resonant build-up of the circulating intensity, providing access to nonlinear optical phenomena at low input power levels [3]. As an example, optical frequency combs have been realized in continuously pumped high-Q optical microresonators due to the Kerr nonlinearity and they are finding a wide range of applications [4]. To explore the nonlinear operating regime of the hybrid-integrated laser in pursuit of highly-coherent Kerr combs, the mode dispersion

of racetrack resonators with 5 GHz and 10 GHz FSR was characterized. Their mode families are measured to have normal dispersion across the telecommunication C-band (Figure 5.1). Also, the dispersion curves exhibit no avoided-mode-crossings, which is consistent with the single-mode nature of the waveguides. As distinct from microresonators with anomalous dispersion wherein bright soliton pulses are readily generated, comb formation is forbidden in microresonators with normal dispersion, unless avoided-mode-crossings are introduced to alter mode family dispersion so as to allow formation of dark pulses [5]. Surprisingly, however, it was nonetheless possible to readily form coherent combs in these devices without either of the aforementioned conditions being satisfied.

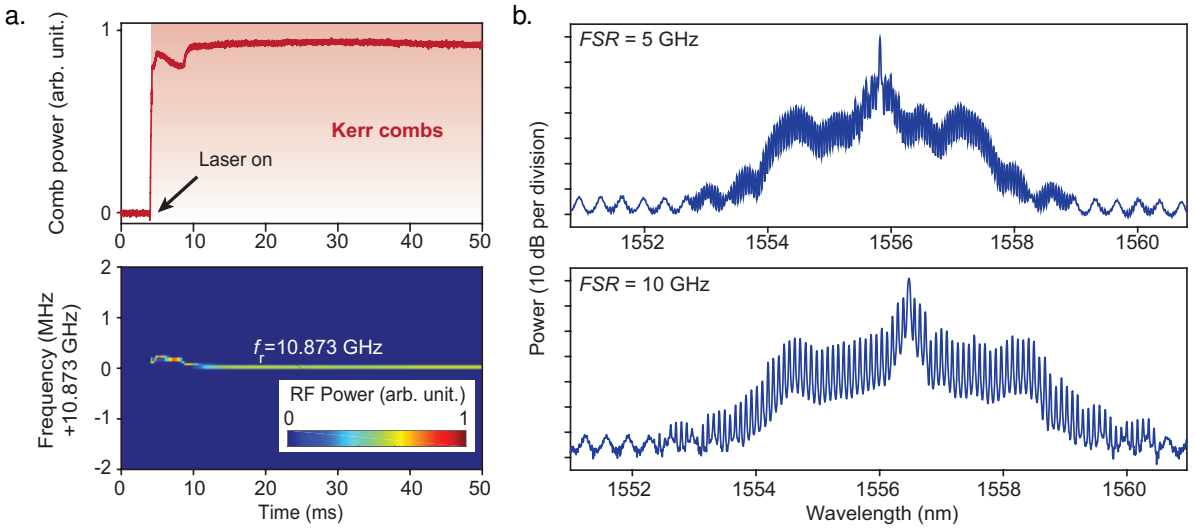

Figure 5.2: **Observation of Kerr comb generation.** (a) Experimental comb power (upper panel) and detected comb repetition rate signal (lower panel) with laser turn-on indicated at 5 ms. (b) Measured optical spectra of mode-locked Kerr combs with 5 GHz (upper panel) and 10 GHz (lower panel) repetition rates. The background fringes, observed below 1553 nm and above 1559 nm for the 5 GHz comb, and below 1552 nm and above 1561 nm in the 10 GHz comb, are attributed to the DFB laser. Reproduced from [2].

Indeed, deterministic, turnkey comb formation was experimentally observed when the DFB laser was switched-on to a preset driving current (see Figure 5.2a). A clean and

stable beatnote of the comb is established 5 ms after turning on the laser, indicating that mode-locking has been achieved (see Figure 5.2a). Plotted in Figure. 5.2c are optical spectra of the mode-locked Kerr combs in racetrack resonators with 5 GHz and 10 GHz FSR, where the typical spectral shape of dark pulses is observed [6, 5, 7, 4].

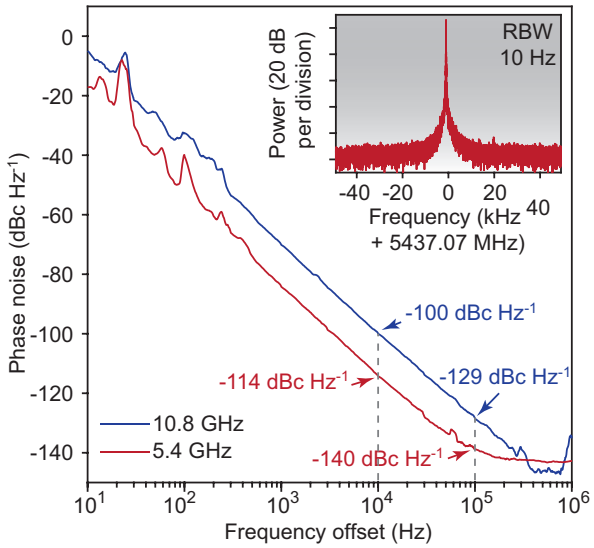

Figure 5.3: **Single-sideband phase noise of dark pulse repetition rates.** Dark pulses with repetition rate 10.8 GHz and 5.4 GHz are characterized. Inset: electrical beatnote showing 5.4 GHz repetition rate. Reproduced from [2].

The stability of mode-locking is characterized by measurement of the comb beat note phase noise (Figure. 5.3). For Kerr combs with 10.8 (5.4) GHz FSR, the phase noise reaches -100 (-114) dBc Hz^{-1} at 10 kHz and -129 (-140) dBc Hz^{-1} at 100 kHz offset frequencies. We note that in order to suppress noise at high-offset frequencies, the pump is excluded in the photodetection using a fiber Bragg grating filter, as suggested by previous works [8].

This unexpected result is studied theoretically in the supplement to [2]. Here, results from that study are briefly summarized. A phase diagram of the microcomb system is given in Figure 5.4a, and separates resonator operation into continuous-wave (c.w.) and Kerr comb regimes based on the viability of parametric oscillation [9]. The intracavity

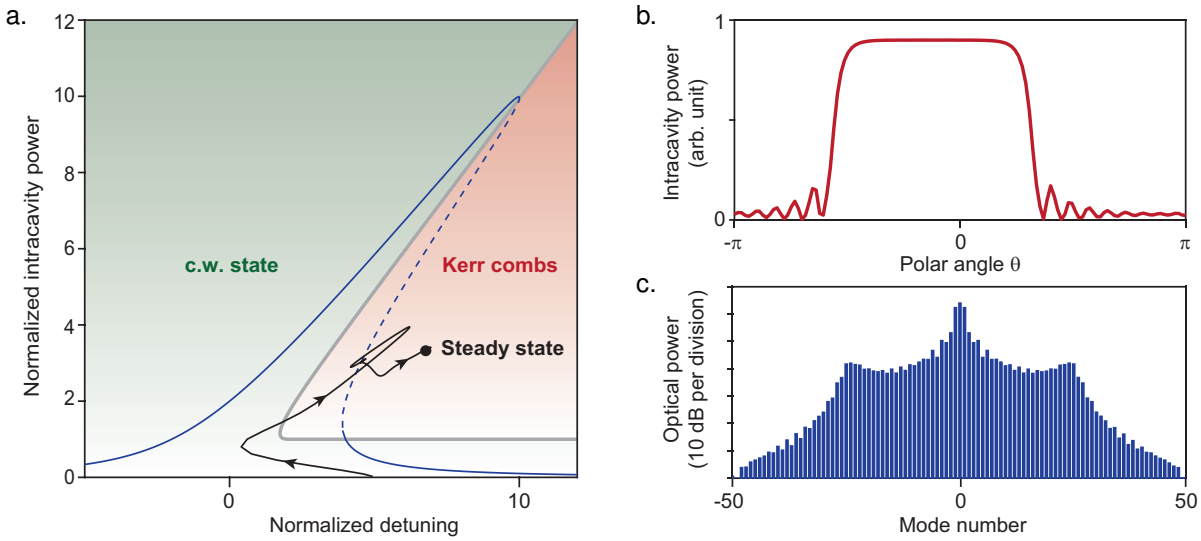

Figure 5.4: **Kerr comb modeling.** (a) Phase diagram of microresonator pumped by an isolated laser. The backscattering is assumed weak enough to not cause mode-splittings. The detuning is normalized to one half of microresonator linewidth, while the intracavity power is normalized to parametric oscillation threshold. Green and red shaded areas indicate regimes corresponding to the c.w. state and Kerr combs. The blue curve is the c.w. intracavity power, where stable (unstable) branches are indicated by solid (dashed) lines. Simulated evolution of the unisolated laser is plotted as the solid black curve, which first evolves towards the middle unstable branch of the c.w. intracavity power curve, and then converges to the comb steady state (average normalized power shown) as marked by the black dot. The initial condition is set within the self-injection locking bandwidth [1], while feedback phase is set to 0. (b) Simulated intracavity field and (c) optical spectrum of the unisolated laser steady state in (a). Reproduced from [2].

power exhibits a typical bi-stable behavior as a function of cavity-pump frequency detuning when pumped by a laser with optical isolation [4]. In contrast, a recent study shows that the feedback from a nonlinear microresonator to a non-isolated laser creates an operating point for the compound laser-resonator system in the middle branch [1]. The operating point is induced through a combination of self- and cross-phase modulation, and is associated with turnkey operation of soliton combs operating under conditions of anomalous dispersion [1]. Here, we have validated through simulation that a similar operating point allows access to dark pulses (normal dispersion) without the requirement for extra dispersion engineering provided by avoided mode crossings. As has been previously shown for bright solitons, the phase of the feedback path plays a major role. Indeed, control of this phase through precision control of the coupling gap between and laser and resonator chips enabled suppression of comb formation for frequency noise measurements reported in Figure 4.1b and Figure 4.3b. The black curve in Figure 5.4a gives the dynamics of the compound laser-resonator system when initialized at a point that is within the locking bandwidth of the system. It first evolves towards the operating point located on the middle branch of the c.w. power bi-stability curve, where comb formation can be initiated, and then converges to a steady Kerr comb state (average normalized power shown). The spectral and temporal profile of the steady state solutions show that flat-top pulses are formed in the microresonator with normal dispersion (Figure 5.4b). Though the possible presence of dark pulse formation in microresonators pumped by a self-injection locked laser has been previously observed [6, 7, 10], the theory of the mutually coupled system has only recently been clarified [1, 2, 11, 12].

The combs generated in these devices exhibit several important properties. In Fig. 5.5a, the spectrum of a 43.2 GHz repetition rate comb is presented. Curiously, this spectrum was generated in a microresonator having a 10.8 GHz FSR. The appearance of rates that are different from the FSR rate has been observed for dark pulses [5]. This line spacing

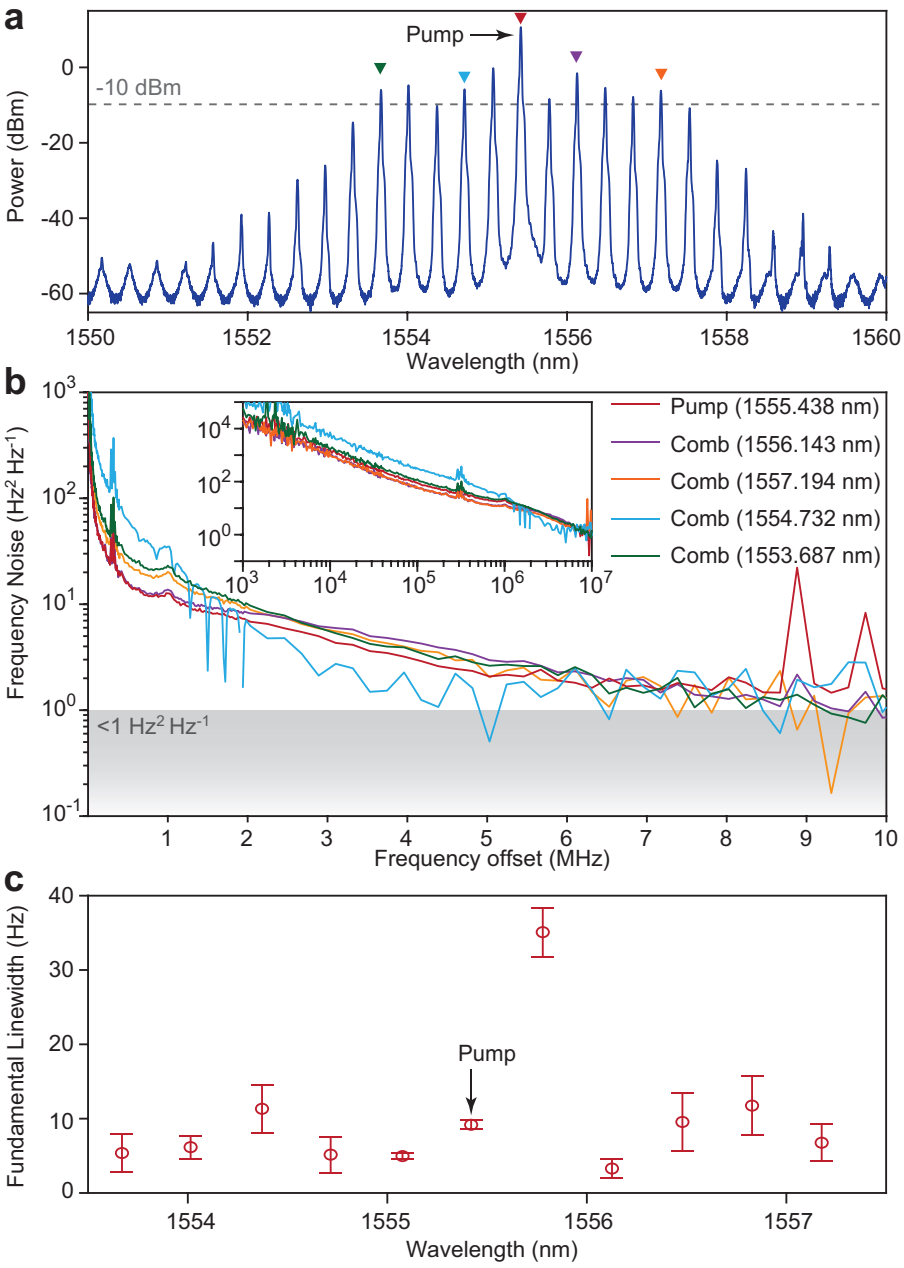

Figure 5.5: **Coherence of integrated mode-locked Kerr combs.** (a) Optical spectrum of a mode-locked comb with 43.2 GHz repetition rate generated in a microresonator with 10.8 GHz FSR. (b) Single-sideband optical frequency noise of the pump and comb lines as indicated in panel a, selected using a tunable fiber-Bragg-grating (FBG) filter. (Inset: the same data in log-log format) (c) Wavelength dependence of white frequency noise linewidth of comb lines in panel a. Reproduced from [2].

is compatible with DWDM channel spacings and 10 comb teeth feature on-chip optical power over -10 dBm, which is a per channel power that is readily usable in DWDM communication systems [13]. However, most significant, is that the white-frequency-noise-level floor for each of these optical lines (Fig. 5.5b) is measured to be on the order of 1 Hz^2 Hz^{-1}. We note that these spectra are white at higher offset frequency, i.e., not rising for higher offset as discussed above for the laser source. The corresponding linewidths of the comb teeth are plotted in Fig. 5.5c. One of the lines exhibits degraded linewidth of approximately 30 Hz, which is suspected to be due to its coincidence with a sub-lasing-threshold side-mode of the DFB laser. Notably, certain comb teeth are quieter than the pump due to the filtering of pump noise by the ultra-high-Q modes. These results represent a two order-of-magnitude improvement as compared to previously demonstrated integrated microcombs [14, 15, 1, 10].

5.2 Stimulated Brillouin scattering

Stimulated Brillouin scattering (SBS) is a nonlinear process involving the scattering of optical waves by acoustic waves [16]. The mechanical properties of a silicon nitride and silicon dioxide are such that the acoustic velocities in silicon nitride core exceed those of silicon dioxide cladding. As a result the optical waveguide forms an acoustic anti-guide, and acoustic energy generated in the stimulated Brillouin scattering process is generally radiated from the silicon nitride core rather than confined within it. This acoustic rejection reduces the acoustic lifetime of SBS phonons, resulting in a weaker SBS gain than would be expected from bulk material [17].

A measurement of SBS gain is shown in Figure 5.6 for a silicon nitride waveguide with 2.8 μm width, 100 nm height cross-sectional geometry, and with 14.5 μm silicon dioxide lower cladding, and 2.2 μm silicon dioxide upper cladding. 21±1 dBm of on-

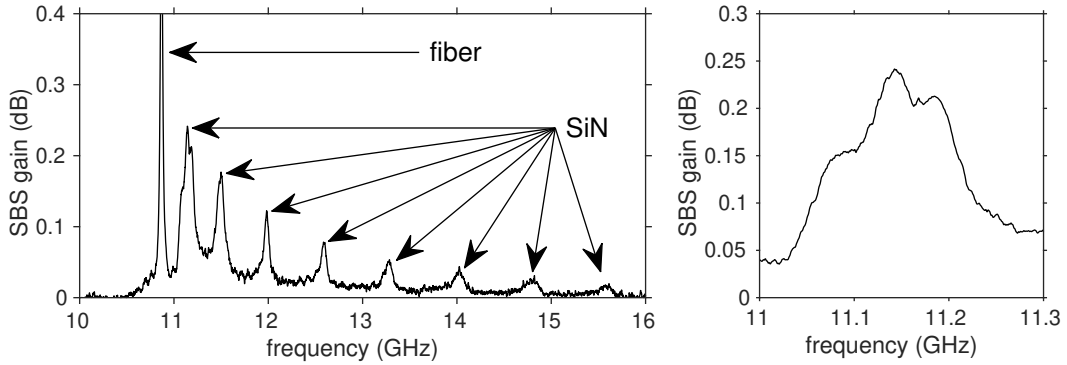

Figure 5.6: **Measured SBS gain spectrum in a 6 m long silicon nitride waveguide,** with 2.8 µm width and 100 nm thickness, and 0.25 dB/m of propagation loss, under 21±1 dBm on-chip pump power. (left panel) A narrow SBS gain feature at 10.87 GHz is attributed to optical fiber in the measurement path, while the multiple spectral peaks spanning 11 GHz to 16 GHz frequency are attributed to the silicon nitride waveguide. (right panel) The largest feature of the gain spectrum is shown, with maximum 0.24 dB of net gain at 11.14 GHz, corresponding to a Brillouin gain of 0.9±0.2 $\mathrm{m^{-1}\,W^{-1}}$ and FWHM of approximately 160 MHz.

chip power at 1550 nm was coupled in the forward direction to a 6 m long waveguide featuring 0.25 dB/m of propagation loss. A probe signal was injected in the reverse direction and swept in the vicinity of the pump wavelength using a continuously tunable laser. The transmitted probe signal was separated from the pump signal with a circulator and narrowband (10 GHz bandwidth) tunable fiber Bragg grating, and measured with an amplified photodetector to characterize the SBS gain.

In the left panel of Figure 5.6, the sharp feature at 10.87 GHz frequency is attributed to SBS within optical fiber in the measurement path. The remaining features are attributed to SBS within the silicon nitride waveguide. The presence of multiple SBS features in the silicon nitride waveguide is likely caused by acoustic reflections at the interface of the silicon dioxide lower cladding and the silicon substrate, as well as the interface of the silicon dioxide upper cladding with the air above, similar to the acoustic resonances observed in [17]. These interfaces form a reflecting waveguide, such that the SBS interactions at frequencies corresponding to the resonant acoustic modes of the

silicon dioxide cladding are enhanced.

The largest feature of the SBS gain spectrum is shown, enlarged, in the right panel of Figure 5.6. The peak, observed gain of 0.24 dB corresponds to a SBS gain coefficient of 0.9 $m^{-1} W^{-1}$, with the uncertainty of ± 0.2 $m^{-1} W^{-1}$ corresponding to uncertainty in the fiber-to-chip coupling loss. The full-width-half-maximum is approximately 160 MHz. The spectrum exhibits two local maxima and a shoulder feature, and is likely comprised of multiple super-imposed acoustic resonances. The gain coefficient of 0.9 $m^{-1} W^{-1}$ is comparable with previously measured gain coefficients of 0.10 $m^{-1} W^{-1}$ in 40 nm thick, 7 µm wide silicon nitride waveguides [18], and 0.067 $m^{-1} W^{-1}$ in 800 nm thick, 2 µm wide silicon nitride waveguides. This level of SBS gain, combined with the ultra-low propagation loss, is compatible with the formation of a narrow linewidth SBS laser [18], and is potentially useful for applications involving microwave signal processing, as well as rotation sensing [19, 18].

5.3 Single-mode Raman laser

In integrated photonics, Raman lasing has been explored in a variety of material systems. In silica microcavities, single-mode Raman oscillation has been observed with threshold powers below 100 µW for cavity diameters below 50 µm [20]. Notably, the first demonstration of continuous-wave lasing in silicon photonics was realized for a silicon Raman laser [21]. Raman lasing has also been observed in integrated photonic microcavities formed from diamond [22], aluminum nitride [23], and lithium niobate [24]. In crystalline media, such as the silicon, diamond, aluminum nitride, and lithium niobate platforms, the Raman gain spectrum generally exhibits a larger peak value, as well as narrow gain bandwidth as compared to amorphous media [25]. As a result, if the microresonator FSR is selected larger than the Raman gain bandwidth, single mode Raman oscillation is

guaranteed. By contrast, single-mode Raman lasing in amorphous glass microresonators generally requires resonator diameters below 50 µm. Large FSR provides the necessary mode selectivity to compensate for the broad gain bandwidth, while small mode volume provides higher field intensity, which compensates for relatively weak magnitude of the Raman gain. In the high-aspect ratio silicon nitride platform, ultra-low waveguide loss enables the observation of Raman interactions, however single mode lasing is difficult to achieve due to bend radius larger than 700 µm, which limits FSR below 50 GHz. In this section, a resonator design is presented to provide enhanced modal selectivity, to enable single-mode Raman laser operation.

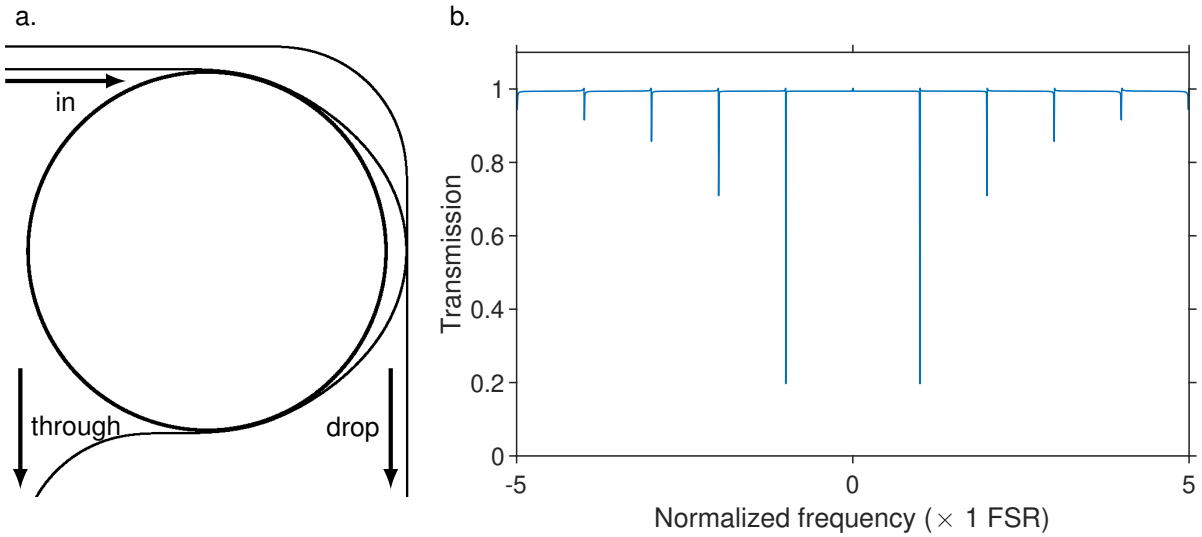

Figure 5.7: **Raman laser design.** (a) Schematic of the resonator structure. The pump light is injected through the port labeled *in*. The Raman laser output is measured from the port labeled *drop*. (b) Simulated resonator transmission spectrum, measured at the port labeled *through*. The frequency axis is normalized to the resonator FSR.

A resonator is designed to use an unbalanced Mach-Zehnder-interferometer-based directional coupler. Length imbalance between the two arms results in frequency-dependent interference interaction in the coupled power, which provides a periodic coupling spectrum. A schematic of the design is shown in Figure 5.9a. The resonator is pumped

through the input waveguide, which couples to the circular, resonator waveguide in two locations. The coupling coefficients at each point are selected to be identical, and much larger than the intrinsic loss of the resonator, such that the resonator is highly overcoupled except at those wavelengths for which the coupler fields interfere destructively and the coupling becomes very weak. The device is expected to lase in a resonance for which the coupler interference is destructive and the coupling is minimized, thus resulting in a higher loaded Q factor approaching the intrinsic Q factor. At such a wavelength, the out-coupling of the coupler waveguide is close to zero. Thus an additional waveguide is coupled to the coupler waveguide between the coupling points to the resonator, labeled *drop* in Figure 5.7. The coupling of this additional waveguide to the coupler waveguide is designed to be much weaker than the individual couplings of the coupler waveguide to the ring waveguide, such that power routed to the drop port does not significantly modify the destructive interference phenomena in the coupler waveguide. At the lasing frequency, the Raman signal is resonantly enhanced within the coupler waveguide, and the Raman spectrum can be observed at the drop-port.

The modeled transmitted power at the through-port is plotted in Figure 5.9b. At 0 normalized frequency, there is destructive interference between the couplers, and the resonator is uncoupled from the coupler waveguide, resulting in a negligible extinction ratio, as well as the highest intrinsic Q factor. The highest exinction ratio is observed for the adjacent resonances, at which the effective coupling coefficient approaches the intrinsic loss. For higher detuning from 0 normalized frequency, the resonances exhibit reduced extinction ratio, as the resonator becomes increasingly overcoupled. Consequently, the loaded Q factor falls with increasing detuning. Close inspection of the resonance shapes in Figure 5.7b reveals that the resonances exhibit a Fano-resonance asymmetric lineshape [26]. In this case, the Fano-resonance lineshape can be attributed to antiresonance within the twice-coupled coupler waveguide. When the electric field within this section

and the resonator are antiresonant, the transmission loss attributed to the drop-port coupler waveguide is eliminated, resulting in a slight enhancement of power transmitted to the through port.

In Figure 5.8, experimental characteristics for a fabricated resonator are demonstrated. The resonator was designed with a bend radius of 1 mm, with FSR of approximately 30 GHz. The path length imbalance of the coupler interferometer is approximately 145 µm, resulting in a FSR in the coupler of 1.3 THz. The amplitude coupling factor of coupler waveguide to the ring waveguide is designed as $k = 0.35$ at each of the coupling regions, while the amplitude coupling factor of the coupler waveguide to the drop port waveguide is designed to be $k = 0.08$. Figure 5.8a shows the measured transmission spectrum of the resonator through-port. The resonator waveguide supports multiple transverse modes, and resonances belonging to two mode families are evident. Those belonging to a higher-order transverse mode are indicated. Those modes corresponding to the resonator fundamental mode exhibit similarity to the simulated spectrum of Figure 5.7b. In Figure 5.8b, the transmission spectrum is measured from the drop-port. At the resonance frequencies of the fundamental mode, the field within the coupler waveguide experiences resonant enhancement, and the transmitted power is higher. Figure 5.8c shows the intrinsic, coupled, and loaded Q factors of the fundamental mode resonances fitted from the measured transmission spectrum shown in Figure 5.8a. The intrinsic Q factor of the fundamental mode is approximately 50 M, while the coupler Q factor varies with frequency. The loaded Q factor varies similarly, such that the loaded Q factor is highest for 1559.4 nm, at which the coupler Q is also highest, and the loaded Q nearly identical to the intrinsic Q factor.

To operate the device as a laser, the device is pumped at the input-port, and the output collected from the drop-port. In the experiment, a pump wavelength of 1559.3 nm was selected, corresponding to a higher-order-mode resonance of the resonator, which

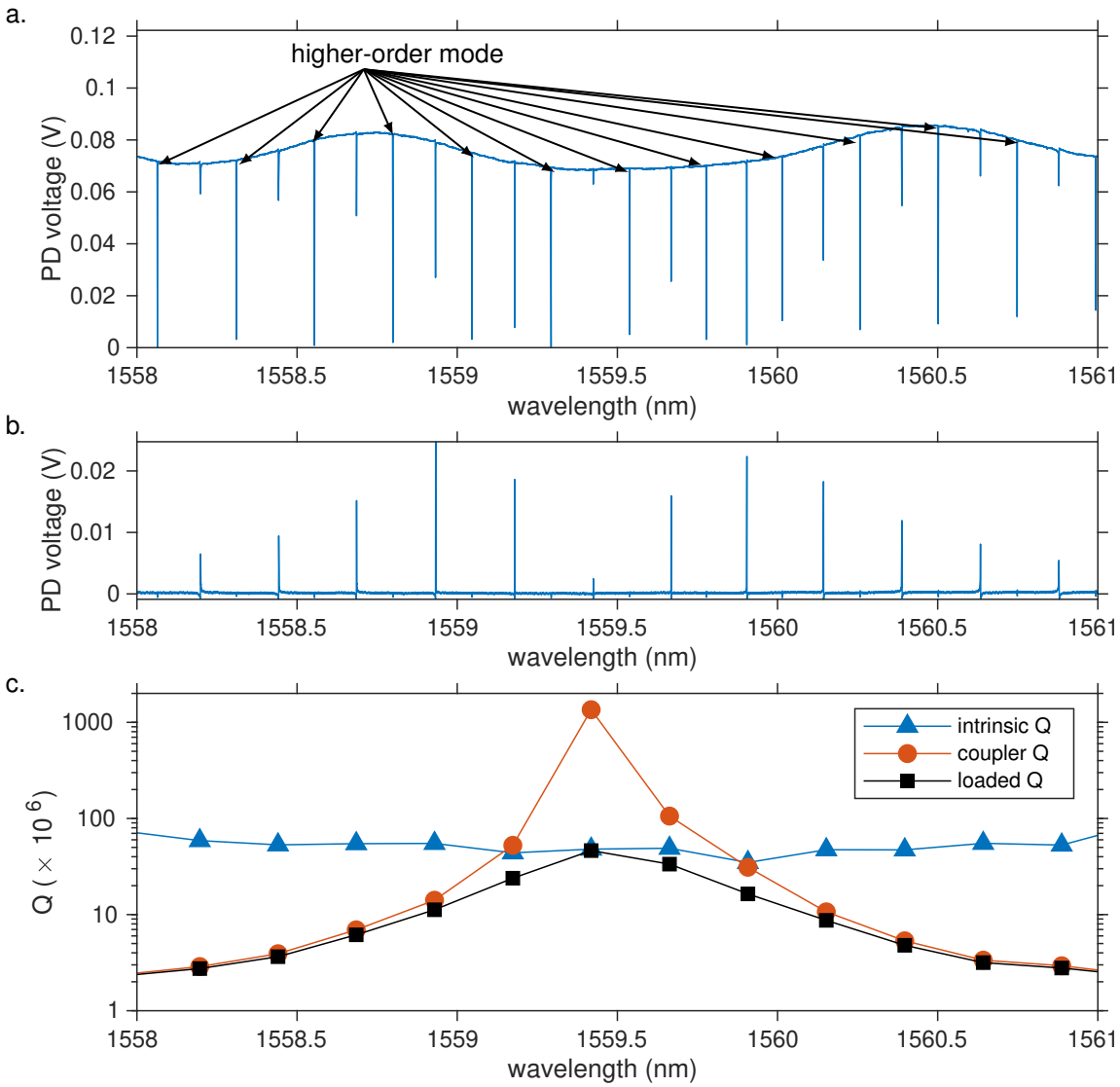

Figure 5.8: **Device characterization.** (a) The spectrum of a fabricated device, measured from the through-port. The resonator waveguide supports multiple transverse modes, and resonances belonging to two mode families are evident. Those belonging to a higher-order transverse mode are indicated. Those corresponding to the resonator fundamental mode exhibit similarity to the simulated spectrum of Figure 5.7b. (b) The spectrum of a fabricated device, measured from the drop-port. At resonances of the fundamental transverse mode, the field within the coupler waveguide experience resonant enhancement. (c) Intrinsic, coupled, and loaded Q factors of the fundamental mode resonances, determined by fitting the transmission spectrum at the through–port.

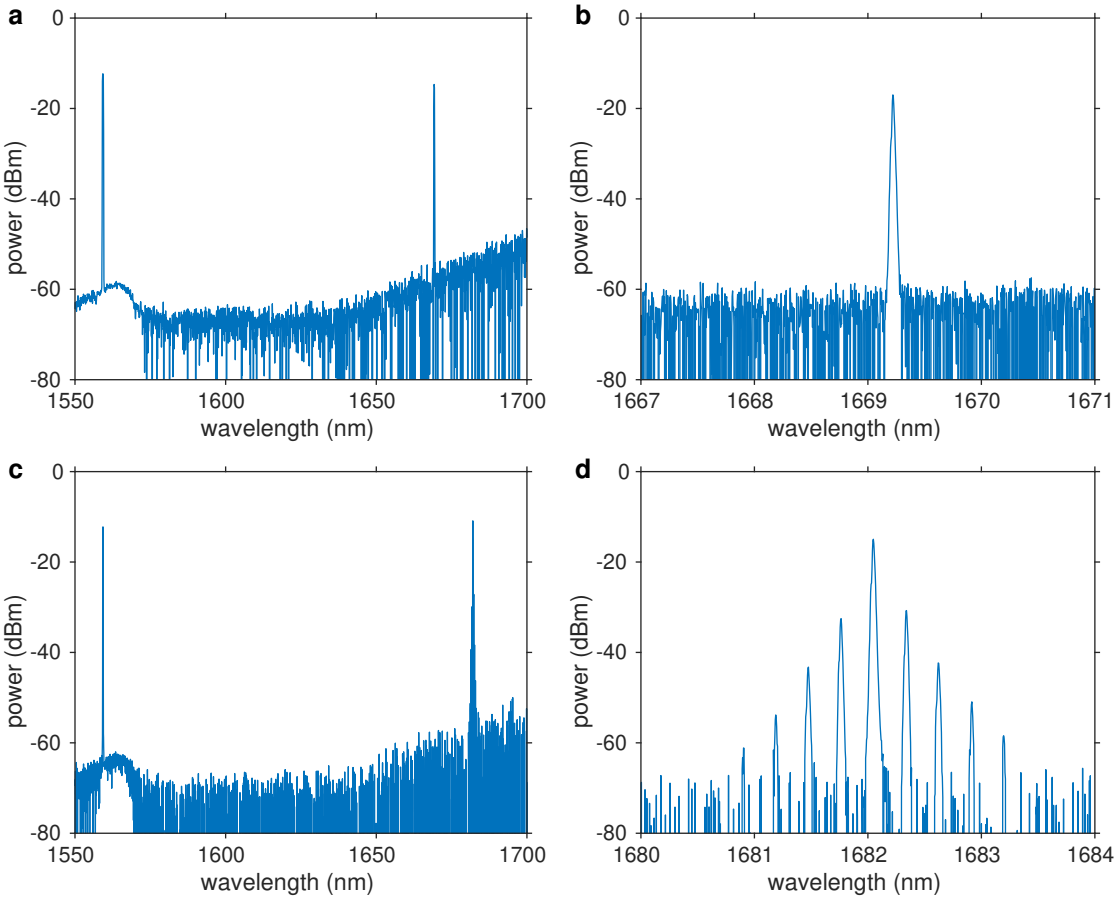

Figure 5.9: **Raman emission.** (a) optical spectrum including both pump wavelength at 1559.3 nm, as well as single-mode Raman lasing signal at 1669 nm, for a pump power of 60 mW in fiber. (b) High resolution optical spectrum, demonstrating that only a single optical mode is excited. The lasing linewidth is instrument limited. (c) optical spectrum for the same conditions as (a), with the pump laser further red-detuned. (d) The high resolution optical spectrum exhibits multiple lasing lines.

exhibits high extinction ratio. The optical spectra, measured from the drop-port of the device, for 60 mW of pump power, are shown in Figure 5.9. Figure 5.9a,b show a single-mode Raman emission line. No optical emission above the measurement noise-floor is evident in the adjacent resonator modes, which have approximately 30 GHz spacing. Thus the side-mode suppression ratio exceeds 40 dB. Figure 5.9c,d show the device with a multi-mode emission state. As compared to Figure 5.9a,b, the pump laser has been slightly red-detuned. Due to optical absorption of the pump light, the resonator is loosely thermally-locked to the pump frequency, and so that the red-detuning of the pump laser causes the resonator itself to also be red-detuned. Since the optical mode exhibits different intensity in the resonator versus coupler waveguides, the red-detuning of the pump leads to differential heating of the resonator and coupler waveguides, which alters the coupling condition. Thus, device can be tuned from a single-wavelength emission state into a multiple-wavelength emission state by differential tuning of the resonator and coupler waveguides. Notably, the slight red-detuning of the pump wavelength causes the emission peak to red-shift from 1669 nm to 1682 nm, which is attributed to the red-shifting of the coupling spectrum of the Mach-Zehnder interferometer coupler. The 1669 nm emission shown in Figure 5.9a,b corresponds to a Raman shift of 12.6 THz, whereas the 1682 nm emission shown in Figure 5.9c,d corresponds to a Raman shift of 14.0 THz. Both are in good agreement with the Raman gain spectrum of silicon dioxide glass, which exhibits a broad peak spanning 12 THz to 15 THz [27, 28].

Summary

Comprised entirely of large-bandgap dielectric materials, ultra-low loss silicon waveguides are frequently touted for their high power-handling capability and compatibility with nonlinear photonics [29]. Thus, a key benefit of ultra-high Q resonators and reduced

propagation loss is the improved accessibility to nonlinear phenomena. In this section, we demonstrate that in spite of stronly normal waveguide dispersion, a wide range of nonlinear phenomena may both be observed and engineered, including highly coherent, dark soliton frequency combs, Brillouin gain, and single-mode Raman lasing.

For Kerr-effect based devices, we expect future work to explore additional design-driven approaches to improving device performance and demonstrating novel capabilities. For example, the use of edge-less grating resonators [30], inter-modal coupling [31], and inter-resonator coupling [32, 33, 34] have been demonstrated to enable degrees of freedom in engineering nonlinear phenomena beyond just waveguide dispersion. Additionally, the use of coupled resonators has also been used to improve the efficiency of comb generation [35]. This platform is well-suited to the application of such approaches, due to its capability to support multiple devices on the same die, with high yield and low loss. The narrow Brillouin gain spectrum in this platform may also be useful for narrowband microwave photonic filters. Further work on the Raman device may further leverage the design to create integrated lasers at wavelengths for which semiconductor-based gain media are not readily available.

Bibliography

[1] B. Shen, L. Chang, J. Liu, H. Wang, Q.-F. Yang, C. Xiang, R. N. Wang, J. He, T. Liu, W. Xie, J. Guo, D. Kinghorn, L. Wu, Q.-X. Ji, T. J. Kippenberg, K. J. Vahala, and J. E. Bowers, *Integrated turnkey soliton microcombs*, *Nature* **582** (2020), no. 7812 365–369.

[2] W. Jin, Q.-F. Yang, L. Chang, B. Shen, H. Wang, M. A. Leal, L. Wu, M. Gao, A. Feshali, M. Paniccia, *et. al.*, *Hertz-linewidth semiconductor lasers using*

CMOS-ready ultra-high-Q microresonators, *Nature Photonics* **15** (2021), no. 5 346–353.

[3] K. J. Vahala, *Optical microcavities*, *Nature* **424** (2003), no. 6950 839–846.

[4] T. J. Kippenberg, A. L. Gaeta, M. Lipson, and M. L. Gorodetsky, *Dissipative Kerr solitons in optical microresonators*, *Science* **361** (2018), no. 6402.

[5] X. Xue, Y. Xuan, Y. Liu, P.-H. Wang, S. Chen, J. Wang, D. E. Leaird, M. Qi, and A. M. Weiner, *Mode-locked dark pulse Kerr combs in normal-dispersion microresonators*, *Nat. Photon.* **9** (2015), no. 9 594–600.

[6] W. Liang, A. A. Savchenkov, V. S. Ilchenko, D. Eliyahu, D. Seidel, A. B. Matsko, and L. Maleki, *Generation of a coherent near-infrared Kerr frequency comb in a monolithic microresonator with normal GVD*, *Opt. Lett.* **39** (2014), no. 10 2920–2923.

[7] V. Lobanov, G. Lihachev, T. Kippenberg, and M. Gorodetsky, *Frequency combs and platicons in optical microresonators with normal GVD*, *Opt. Express* **23** (2015), no. 6 7713–7721.

[8] W. Liang, D. Eliyahu, V. Ilchenko, A. Savchenkov, A. Matsko, D. Seidel, and L. Maleki, *High spectral purity Kerr frequency comb radio frequency photonic oscillator*, *Nat. Commun.* **6** (2015) 7957.

[9] C. Godey, I. V. Balakireva, A. Coillet, and Y. K. Chembo, *Stability analysis of the spatiotemporal Lugiato-Lefever model for Kerr optical frequency combs in the anomalous and normal dispersion regimes*, *Phys. Rev. A* **89** (2014), no. 6 063814.

[10] G. V. Lihachev, J. Liu, L. Chang, J. He, R. N. Wang, J. Guo, A. S. Raja, E. Lucas, N. G. Pavlov, J. D. Jost, D. Kinghorn, J. E. Bowers, and T. J.

Kippenberg, *Laser self-injection locked frequency combs in a normal GVD integrated microresonator*, in *CLEO: Science and Innovations*, pp. STh1O–3, Optical Society of America, 2020.

[11] N. M. Kondratiev and V. E. Lobanov, *Modulational instability and frequency combs in whispering-gallery-mode microresonators with backscattering*, *Phys. Rev. A* **101** (2020), no. 1 013816.

[12] N. M. Kondratiev, A. S. Voloshin, V. E. Lobanov, and I. A. Bilenko, *Numerical modelling of WGM microresonator Kerr frequency combs in self-injection locking regime*, in *Nonlinear Optics and its Applications 2020*, vol. 11358, p. 113580O, International Society for Optics and Photonics, 2020.

[13] A. Fülöp, M. Mazur, A. Lorences-Riesgo, Ó. B. Helgason, P.-H. Wang, Y. Xuan, D. E. Leaird, M. Qi, P. A. Andrekson, A. M. Weiner, *et. al.*, *High-order coherent communications using mode-locked dark-pulse Kerr combs from microresonators*, *Nat. Commun.* **9** (2018), no. 1 1–8.

[14] B. Stern, X. Ji, Y. Okawachi, A. L. Gaeta, and M. Lipson, *Battery-operated integrated frequency comb generator*, *Nature* **562** (2018), no. 7727 401.

[15] A. S. Raja, A. S. Voloshin, H. Guo, S. E. Agafonova, J. Liu, A. S. Gorodnitskiy, M. Karpov, N. G. Pavlov, E. Lucas, R. R. Galiev, *et. al.*, *Electrically pumped photonic integrated soliton microcomb*, *Nat. Commun.* **10** (2019), no. 1 680.

[16] R. W. Boyd, *Nonlinear optics*. Academic press, 2020.

[17] F. Gyger, J. Liu, F. Yang, J. He, A. S. Raja, R. N. Wang, S. A. Bhave, T. J. Kippenberg, and L. Thévenaz, *Observation of stimulated brillouin scattering in*

silicon nitride integrated waveguides, *Physical review letters* **124** (2020), no. 1 013902.

[18] S. Gundavarapu, G. M. Brodnik, M. Puckett, T. Huffman, D. Bose, R. Behunin, J. Wu, T. Qiu, C. Pinho, N. Chauhan, *et. al.*, *Sub-Hertz fundamental linewidth photonic integrated Brillouin laser*, *Nature Photonics* **13** (2019), no. 1 60–67.

[19] D. J. Blumenthal, R. Heideman, D. Geuzebroek, A. Leinse, and C. Roeloffzen, *Silicon nitride in silicon photonics*, *Proceedings of the IEEE* **106** (2018), no. 12 2209–2231.

[20] T. J. Kippenberg, S. M. Spillane, B. Min, and K. J. Vahala, *Theoretical and experimental study of stimulated and cascaded raman scattering in ultrahigh-q optical microcavities*, *IEEE Journal of selected topics in Quantum Electronics* **10** (2004), no. 5 1219–1228.

[21] H. Rong, S. Xu, Y.-H. Kuo, V. Sih, O. Cohen, O. Raday, and M. Paniccia, *Low-threshold continuous-wave raman silicon laser*, *Nature Photonics* **1** (2007), no. 4 232–237.

[22] P. Latawiec, V. Venkataraman, M. J. Burek, B. J. M. Hausmann, I. Bulu, and M. Lončar, *On-chip diamond raman laser*, *Optica* **2** (Nov, 2015) 924–928.

[23] X. Liu, C. Sun, B. Xiong, L. Wang, J. Wang, Y. Han, Z. Hao, H. Li, Y. Luo, J. Yan, T. Wei, Y. Zhang, and J. Wang, *Integrated continuous-wave aluminum nitride raman laser*, *Optica* **4** (Aug, 2017) 893–896.

[24] M. Yu, Y. Okawachi, R. Cheng, C. Wang, M. Zhang, A. L. Gaeta, and M. Lončar, *Raman lasing and soliton mode-locking in lithium niobate microresonators*, *Light: Science & Applications* **9** (2020), no. 1 1–7.

[25] M. A. Ferrara and L. Sirleto, *Integrated raman laser: A review of the last two decades*, *Micromachines* **11** (2020), no. 3 330.

[26] M. F. Limonov, M. V. Rybin, A. N. Poddubny, and Y. S. Kivshar, *Fano resonances in photonics*, *Nature Photonics* **11** (2017), no. 9 543–554.

[27] R. Stolen and E. Ippen, *Raman gain in glass optical waveguides*, *Applied Physics Letters* **22** (1973), no. 6 276–278.

[28] G. P. Agrawal, *Nonlinear fiber optics*, in *Nonlinear Science at the Dawn of the 21st Century*, pp. 195–211. Springer, 2000.

[29] D. J. Moss, R. Morandotti, A. L. Gaeta, and M. Lipson, *New cmos-compatible platforms based on silicon nitride and hydex for nonlinear optics*, *Nature photonics* **7** (2013), no. 8 597–607.

[30] S.-P. Yu, D. C. Cole, H. Jung, G. T. Moille, K. Srinivasan, and S. B. Papp, *Spontaneous pulse formation in edgeless photonic crystal resonators*, *Nature Photonics* **15** (2021), no. 6 461–467.

[31] H. Wang, Y.-K. Lu, L. Wu, D. Y. Oh, B. Shen, S. H. Lee, and K. Vahala, *Dirac solitons in optical microresonators*, *Light: Science & Applications* **9** (2020), no. 1 1–15.

[32] A. Tikan, J. Riemensberger, K. Komagata, S. Hönl, M. Churaev, C. Skehan, H. Guo, R. N. Wang, J. Liu, P. Seidler, *et. al.*, *Emergent nonlinear phenomena in a driven dissipative photonic dimer*, *Nature Physics* **17** (2021), no. 5 604–610.

[33] K. Komagata, A. Tikan, A. Tusnin, J. Riemensberger, M. Churaev, H. Guo, and T. J. Kippenberg, *Dissipative kerr solitons in a photonic dimer on both sides of exceptional point*, *arXiv preprint arXiv:2101.09237* (2021).

[34] S. Mittal, G. Moille, K. Srinivasan, Y. K. Chembo, and M. Hafezi, *Topological frequency combs and nested temporal solitons*, *arXiv preprint arXiv:2101.02229* (2021).

[35] Y. Hu, M. Yu, B. Buscaino, N. Sinclair, D. Zhu, R. Cheng, A. Shams-Ansari, L. Shao, M. Zhang, J. M. Kahn, *et. al.*, *High-efficiency and broadband electro-optic frequency combs enabled by coupled micro-resonators*, *arXiv preprint arXiv:2111.14743* (2021).

Chapter 6

Seamless multi-reticle photonics

While Moore's law predicted shrinking transistors would enable exponential scaling of electronic circuits, the footprint of photonic components is limited by the wavelength of light. Thus, future high-complexity photonic integrated circuits (PICs) such as petabit-per-second transceivers, thousand-channel switches, and photonic quantum computers will require more area than a single reticle provides. In our novel approach, we overlay and widen waveguides in adjacent reticles to stitch a smooth transition between misaligned exposures. In SiN waveguides we measure ultra-low loss of 0.0004 dB per stitch, and produce a stitched delay line 23 m in length. We extend the design to silicon channel waveguides, and predict 50-fold lower loss or 50-fold smaller footprint versus a multi-mode-waveguide-based method. Our approach enables large-scale photonic integrated circuits to scale seamlessly beyond the single-reticle limit. The contents of this chapter are published as [1].

Introduction

While major progress in the interconnect bandwidth of PICs has been driven by increasing modulation rate, further improvement in bandwidth will require spatial, spectral, and polarization multiplexing [2, 3]. Indeed, a recent demonstration with 1.6 Tbit s^{-1} capacity used 16 parallel 100 Gbit s^{-1} lanes [4]. As each lane needs a driver, modulator, and fan-out for electrical and optical connections, future higher-capacity optical interconnects will occupy even larger chip area. Similarly, switches [5], optical phased arrays (OPA) [6, 7], quantum circuits [8], and tensor cores [9] have all demonstrated optical systems with component count from several hundreds to tens of thousands, and will grow in area as their capabilities improve. The need for large chips is especially acute for ultra-low-loss photonic platforms [10, 11] that are desirable for microwave photonics [12, 13], nonlinear optics [10], and gyroscopes [14, 15, 16]. These platforms may have bend radius 1 mm or larger [10], and often require PICs at the cm-scale.

The availability of 300 mm substrates in silicon foundries and the relatively large dimensions of PIC components enable PICs to be fabricated at low cost and high volume using prior-generation process nodes. Thus, increasing the area of PICs to the size of a reticle and beyond is an economical way to continue to scale performance. In Table 6.1, we estimate performance as die size grows to multiple reticles. With switch bandwidths projected to reach 51.2 Tbit s^{-1} by 2024 [3], the footprint of interconnect PICs interfacing with those switches may soon surpass a single reticle. A 8192 element active OPA spanned an entire reticle [7]. Optical switches [5] and gyroscopes [16] have already reached multiple reticles, while a photonic quantum computer could achieve quantum supremacy in a system spanning three reticles [8]. The need for multi-reticle PICs motivates us to seek a stitching method optimized for photonics.

Multi-reticle exposures have already been used in electronic circuits for large-scale

Table 6.1: **Multi-reticle performance of integrated optical systems.** We assume single-reticle size 2 cm×2 cm. Interconnect bandwidth based on bandwidth density 100 Gbit s^{-1} mm^{-2} [4]. Switch radix based on 110 µm×110 µm unit cell [5]. Neural network, quantum circuit size based on density of 2450 phase tuners per 21 cm^2 [8]. Passive 2D OPA size based on 4096 emitters per 576 µm×576µm [6]. Active 1D OPA emitter density based on an 8192 emitter chip [7]. Delay line length, gyroscope scale factor (rotation rate per Sagnac phase) based on Archimedes spiral of 50 µm pitch, 1 mm minimum bend radius [14].

	# of reticles		
	1	2×2	4×4
Interconnect bandwidth (Tbit s^{-1})	40	160	640
Optical switch (2D) radix	180×180	360×360	720×720
Optical neural network size (neurons)	470	1,900	7,500
Quantum circuit mode count (qubits)	21	43	86
OPA (2D, passive) emitters	5,000,000	20,000,000	80,000,000
OPA (1D, active) emitters	5,000	20,000	80,000
Delay line length (m)	6	25	100
Gyroscope scale factor ((°/h)/µrad)	180	23	2.8

phased-array antennas and image sensors. Misalignment of exposures normal to the reticle boundary (x-direction in Fig. 6.1) can lead to a gap between reticles, and is addressed by overlaying the adjacent reticles by a distance L larger than the alignment tolerance (Fig. 6.1a). Lateral misalignment δ (y-direction) causes an abrupt step in the sidewall as the waveguide crosses the reticle boundary. Deep-UV stepper alignment error of tens-of-nanometers [17] has little impact on all but the narrowest electronic wires, but such sidewall discontinuities lead to appreciable loss in photonic waveguides.

We propose enlarging the overlay distance, and widening the waveguides as they traverse the stitch length L, which results in a seamless transition (Fig. 6.1b). To design for alignment tolerance δ_{MAX}, the waveguide in each reticle widens linearly by $2\delta_{\mathrm{MAX}}$ as it traverses the stitch length, L. The angle of the sidewall with respect to the propagation axis is $\theta = \tan^{-1}(\delta_{\mathrm{MAX}}/L) \approx \delta_{\mathrm{MAX}}/L$. Our scheme applies to positive photoresist, in which exposed areas (indicated by hatching) are dissolved in developer and etched to

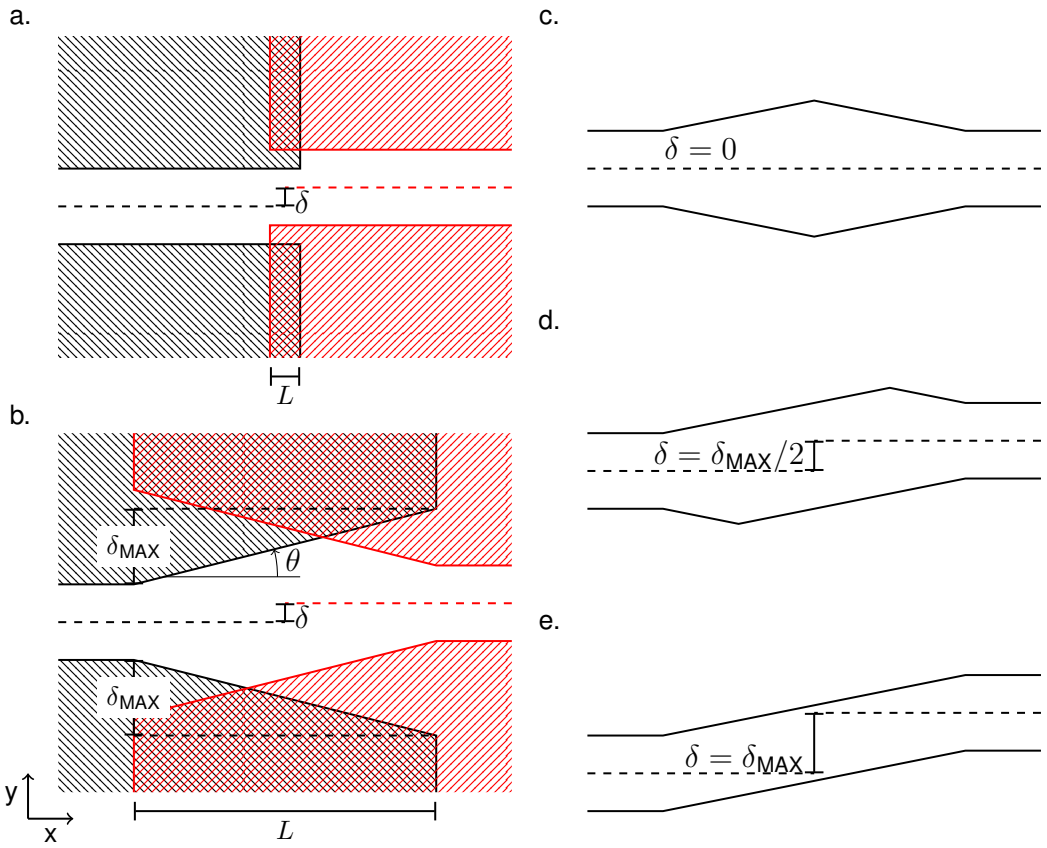

Figure 6.1: **Optimized stitching method.** (a) Plan-view of un-optimized stitched waveguide between adjacent reticles. Black (red) hatched areas indicate regions which are exposed by the left (right) reticle; the waveguide is defined by the remaining unexposed areas; the dashed lines indicate the centers of the respective waveguides; δ indicates the lateral alignment error. Stitching causes abrupt steps in the sidewall at the reticle boundary. (b) Instead, widening the overlaid waveguides over a larger distance L results in a continuous sidewall; the angle of the sidewall to the propagation axis is given by θ; the waveguides widen by $2\delta_{\mathrm{MAX}}$ yielding alignment tolerance δ_{MAX}; regions with both black and red hatching are exposed by both reticles. The stitched waveguide's plan-view-profile varies from (c) zero misalignment, to (d) intermediate misalignment, to (e) the maximum tolerable misalignment. Reproduced from [1].

form the waveguide. For negative resist, each waveguide should instead be narrowed. In the case of perfect alignment (Fig. 6.1c), the waveguide widens and then narrows in the stitch region. For misalignment half of the alignment tolerance (Fig. 6.1d), the waveguide widens at the beginning of the stitch region, and narrows at the end, as in the previous case. However, the width of the waveguide in the center of the stitch is constant, with propagation direction tilted from the input and output waveguides by the angle θ. For a misalignment equal to the alignment tolerance (Fig. 6.1e), the waveguide width is constant throughout the stitch region, and angles by θ with respect to the input and output waveguides. Thus, the lateral misalignment is accommodated by a corresponding length of waveguide with offset angle θ. The widening of the waveguide should be adiabatic enough that mode conversion loss is negligible, so the loss of the stitch can be entirely attributed to the junctions at either end of the angled waveguide, where the propagation direction changes and the phase fronts of the waveguide modes are misaligned. Accordingly, we refer to the stitched waveguide of Fig. 6.1a as an "abrupt" stitch, and our optimized design of Fig. 6.1b as an "angled" stitch consisting of two "angled" junctions.

Measurement and Modeling

We validate our design using 100 nm thick silicon nitride waveguides in a CMOS-foundry ultra-low loss photonic platform [10]. Prior work in a similar platform [16, 15] for which 0.1 dB/m loss is achievable [11] demonstrated abrupt stitching junctions with an estimated loss of 0.006 dB/stitch, contributing around 0.2 dB/m to the total loss in a 3 m delay line. We demonstrate our improved stitching method by fabricating stitched delay lines 23 m in length with an order-of-magnitude lower stitching loss (Fig. 6.2). In our design, the input to the stitch is a single-mode waveguide of 2.8 µm width. We select δ_{MAX}

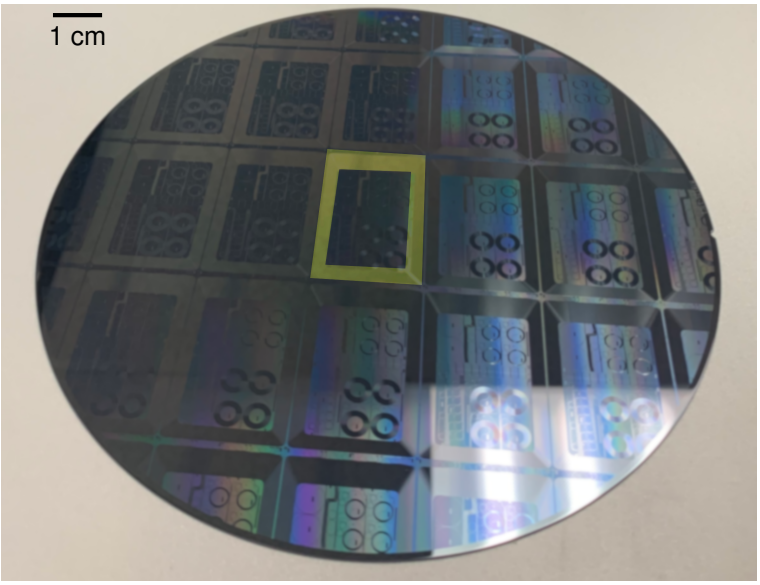

Figure 6.2: **Fabricated 200 mm wafer with stitched, 23 m long, delay lines** on the perimeter of each die. The delay line of the center die has been highlighted. Each die consists of two stitched reticles. The interior of each die is occupied by test structures. Reproduced from [1].

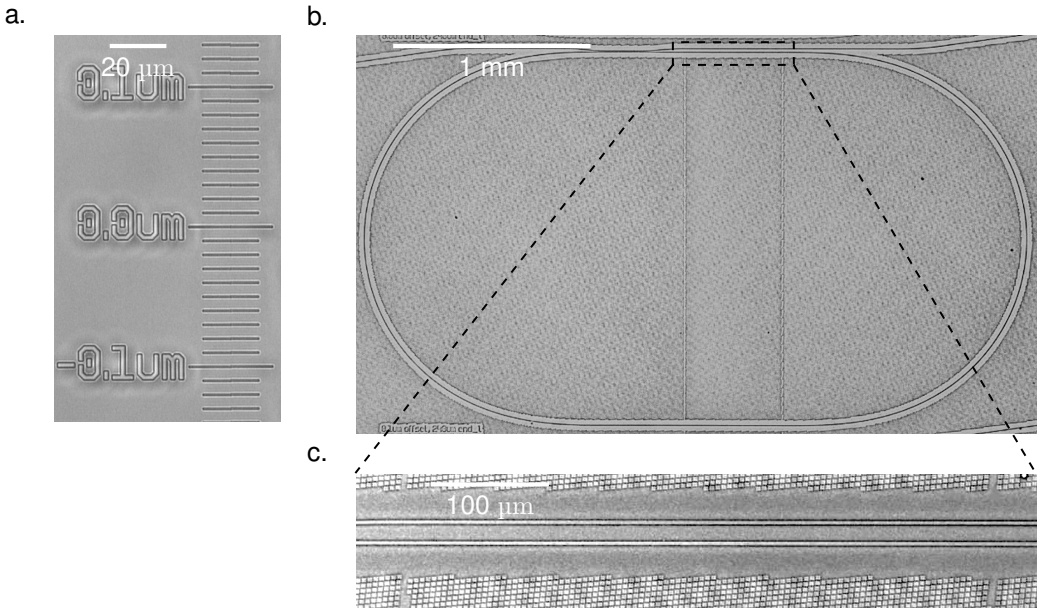

Figure 6.3: **Micrographs of stitching test structures.** (a) Micrograph of vernier–type alignment test structure between adjacent reticles. Each half of the mark is exposed separately, each mark represents an additional 10 nm alignment bias between left and right reticles. We estimate an alignment error below 20 nm. (b) Stitched race-track resonator test structure. (c) Micrograph of stitched waveguides in a resonator. Reproduced from [1].

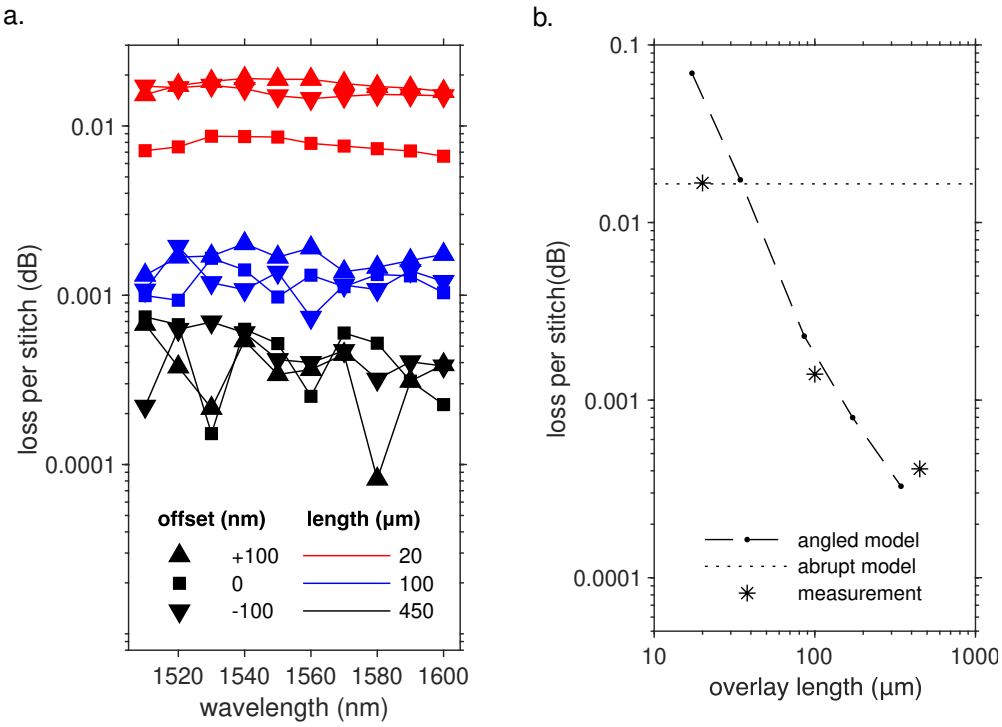

Figure 6.4: **Experimental stitching results.** (a) Measured stitching loss versus wavelength for each test structure. Nine configurations were measured, consisting of three different stitch lengths each evaluated for three mask offsets. (b) Comparison of measurement with simulation of our design at ±100 nm misalignment. Reproduced from [1].

of 300 nm, so that the waveguide widens to a width of 3.4 µm at the edge of the reticle. When exposed, adjacent reticles are overlaid by 500 µm. We design structures with stitch length L of 20 µm, 100 µm, and 450 µm. We observe a lateral misalignment below 20 nm on the fabricated wafer (Fig. 6.3a), so we use mask bias to apply additional misalignment (y-direction) of -100 nm, 0 nm, and 100 nm for each stitch length. We fabricate a stitched racetrack resonator for each configuration (Fig. 6.3b). The resonator transmission spectra were measured and fitted to determine the resonator round-trip loss, and compared to a control device from the same die, consisting of a non-stitched resonator of identical dimensions. Any excess round-trip loss of the stitched devices versus the control device was attributed to the stitch design. The control device features an intrinsic Q factor of 45 M and round-trip loss of 0.005 dB at 1550 nm wavelength, allowing us to measure very low stitching losses. The measured data is presented in Fig. 6.4a. For 20 µm, 100 µm, and 450 µm stitch lengths, the mean stitching losses, averaged over ±100 nm bias and spectral range 1510 nm to 1600 nm, are 0.0167 dB, 0.0014 dB, and 0.00041 dB, with standard deviations of the means 0.0003 dB, 0.00008 dB, and 0.00004 dB, respectively. The measured loss of 0.0004 dB/stitch represents an order-of-magnitude improvement compared to prior work [16, 5].

We compare our measured results with simulation. Rather than simulate the full structure, we observe that for short stitch lengths, we expect input and output waveguide modes to couple directly through the near-field such that the loss approaches that of an abrupt junction, which we simulate by the modal overlap of the input and output waveguides with 100 nm alignment error. For large stitch lengths, the stitch is modeled by two junctions of waveguides with propagation directions differing by θ, which we calculate by finite-difference-time-domain simulation. The waveguide width of the stitch at the angle junction tapers up to δ_{MAX} wider than the input waveguide (W) depending on the misalignment, but $\delta_{\mathrm{MAX}} \ll W$ so the dependence of loss on misalignment is small.

The waveguide width at the junction is simulated as $W + \delta_{\mathrm{MAX}}$, which provides a tight upper bound on the loss. The results of these two models are plotted with the measured stitching loss (Fig. 6.4b). The loss of the 20 µm device agrees with the abrupt junction model, whereas the losses of the 100 µm and 450 µm devices agree with the angled junction model. Indeed, this suggests for a given misalignment (in this case ±100 nm), the abrupt junction model imposes a maximum loss for the stitched waveguide, that is, the abrupt junction model is valid for stitch lengths below the point at which the models intersect (here, 35 μm), while the angled junction model is valid above it. The data of Fig. 6.4a are consistent with this interpretation: the loss in an abrupt junction should vary with the alignment error, and the loss in the 20 µm long stitch indeed exhibits the lowest loss for 0 nm alignment bias. On the other hand, we expect the loss in the angled junctions to depend only on the angular misalignment $\theta \approx \delta_{\mathrm{MAX}}/L$, independent of the alignment error δ. Accordingly, the measured losses in 100 µm and 450 µm long stitches do not depend on alignment bias.

We use our validated model to compare the performance of seamless "angled" stitching method to the typical "abrupt" stitching method. Indeed, other authors [5] have employed abrupt stitching of 10 µm wide waveguides to achieve loss of 0.004 dB/stitch. While the abrupt stitch itself occupies zero length, the mode converters on either side of the stitch must be included in the length as well. We calculate the necessary length according to Milton and Burns [18] $L = n_{\mathrm{eff}} {W_{\mathrm{MAX}}}^2/\alpha\lambda$, where L is the total length of the abrupt stitch including two mode converters, W_{MAX} is the width of the waveguide at the abrupt stitch, n_{eff} is the effective index of the mode at the stitch, $\alpha = 1$ is a scaling factor unity or lower for low-loss, and $\lambda = 1550$ nm is the wavelength. The loss of the stitch is then calculated by mode overlap at the wide-waveguide abrupt junction. For simplicity, the conversion from single-mode to multi-mode is assumed lossless. In Fig. 6.5a we compare the abrupt stitch loss to the angled stitch loss for an alignment error of 100 nm.

In the angled stitch design, we retain the 2.8 µm silicon nitride waveguide width at the stitch input and output, but choose δ_{MAX} of 100 nm. This reduction of δ_{MAX} from 300 nm in measured devices to 100 nm still represents a conservative alignment error, since a 3σ value of alignment error below 18 nm is achievable for deep-UV stepper lithography [17]. The abrupt stitch loss is simulated up to a waveguide width of 10 µm. For stitch length beyond 12 µm, the angled stitch outperforms the abrupt stitch.

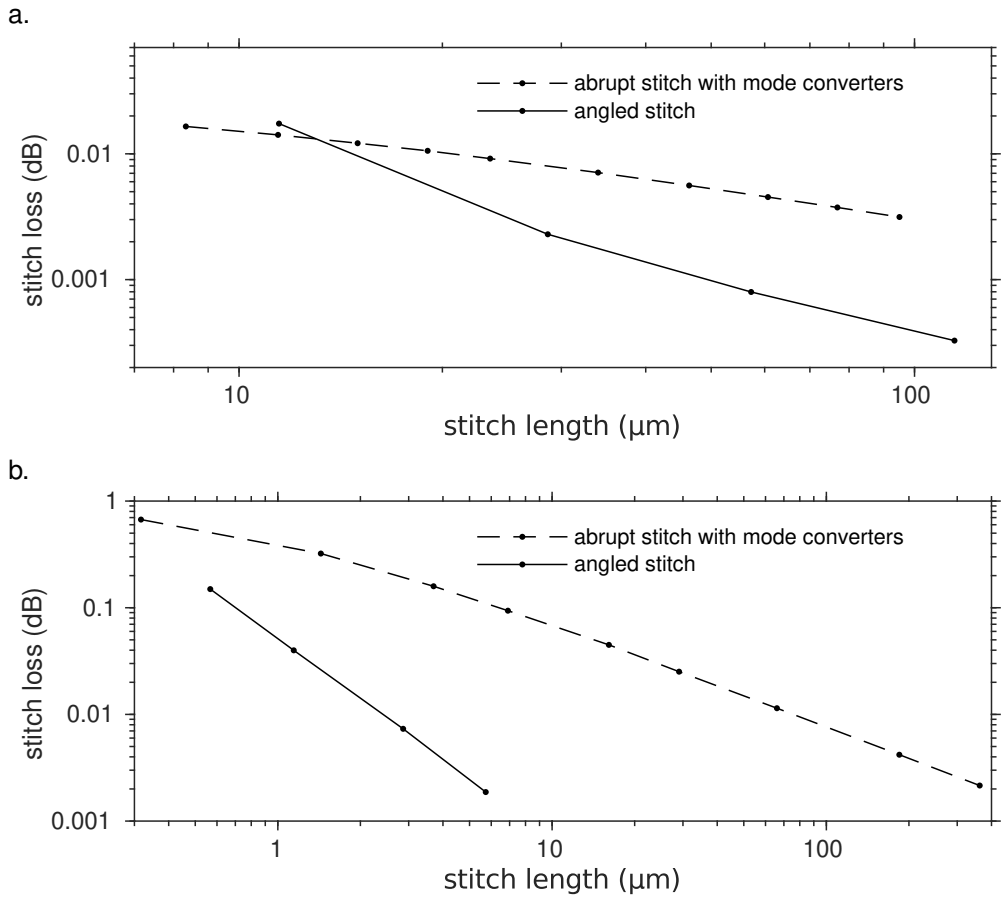

Figure 6.5: **Simulated loss vs length of "abrupt" and "angled" stitching** at 100 nm alignment error for **a,** 100 nm thick silicon nitride waveguides and **b,** 220 nm thick silicon waveguides. To compare the loss and length of abrupt stitches with angled stitches, abrupt stitch loss is simulated as a function of waveguide width, while the length is calculated as the length of the corresponding mode converters for each waveguide width. Reproduced from [1].

To demonstrate the generality of the approach, we also consider widely-available,

220 nm thick, deeply-etched silicon channel waveguides. In this stitch design, we adopt 400 nm single-mode waveguide width at the input and output of the stitch, δ_{MAX} of 100 nm, and we again simulate the performance of our design as a function of stitch length L (Fig. 6.5b). The abrupt stitch loss is simulated up to a waveguide width of 14 µm. Our optimized design in this silicon waveguide platform approaches 0.001 dB per stitch for a stitch length below 10 µm, compared to over 50 µm in the silicon-nitride-based design. We attribute this reduction to the narrower waveguide width of 400 nm, compared to 2.8 µm. This is because a narrower optical mode, for the same angle θ, accumulates less phase error across its width due to the mismatched phase fronts at the angled junction. At a stitch length of just 6 µm, our silicon waveguide stitch design achieves approximately 50-fold lower loss for the same length, or approximately 50-fold smaller footprint at the same level of loss, compared to the abrupt stitching approach.

Discussion

In conclusion, we presented a novel method for stitching photonic waveguides to enable seamless transitions between reticles. We demonstrated both in simulation and experiment that it produces stitched waveguides with smaller footprint and lower loss by over an order of magnitude compared to prior approaches. For delay lines and interferometric gyroscopes where the waveguide crosses a stitching boundary multiple times per round trip, ultra-low stitching loss is critical. In our 23 m long device, the 332 stitches contribute just 0.13 dB to the total loss. However, for optical switch and interconnect applications, no signal path should cross a stitching boundary more than a handful of times, so the small stitch footprint is more valuable. Indeed, an abrupt stitch limits the pitch of waveguides crossing the reticle boundary to a value above the waveguide's width – over 10 µm in prior works [5]. In our approach, the width of the stitched waveguide can

be kept close to the single mode width, allowing a high density of waveguides to traverse reticles. Furthermore, while our approach was developed for the case of deep-UV stepper lithography in a foundry context, we note that it could be applied to the contact, i-line stepper, and even E-beam lithography tools that are common in research contexts.

Initially driven by demand for low-cost interconnects for datacenter networks and high-performance computing, photonic integrated circuit performance and scale have grown dramatically in recent years. Large-scale devices have emerged: high-radix optical switches; optical phased arrays for LiDAR, free-space communications, and augmented/virtual reality displays; meshed interferometer networks for artificial intelligence, machine learning, and quantum computation; and ultra-low loss delay lines and resonators for nonlinear optics and metrology. Many of these applications have already demonstrated PICs at or beyond the single reticle limit, and will continue to grow as fabrication yields improve. We believe low-loss multi-reticle photonic integrated circuits will soon become a critical tool in the optical system designer's toolbox.

Bibliography

[1] W. Jin, A. Feshali, M. Paniccia, and J. E. Bowers, *Seamless multi-reticle photonics*, *Optics Letters* **46** (2021), no. 12 2984–2987.

[2] N. Margalit, C. Xiang, S. M. Bowers, A. Bjorlin, R. Blum, and J. E. Bowers, *Perspective on the future of silicon photonics and electronics*, *Applied Physics Letters* **118** (2021), no. 22 220501.

[3] B. Buscaino, E. Chen, J. W. Stewart, T. T. Pham, and J. M. Kahn, *External vs. integrated light sources for intra-data center co-packaged optical interfaces*, *Journal of Lightwave Technology* (2020).

[4] S. Fathololoumi, D. Hui, S. Jadhav, J. Chen, K. Nguyen, M. Sakib, Z. Li, H. Mahalingam, S. Amiralizadeh, N. N. Tang, H. Potluri, M. Montazeri, H. Frish, R. A. Defrees, C. Seibert, A. Krichevsky, J. K. Doylend, J. Heck, R. Venables, A. Dahal, A. Awujoola, A. Vardapetyan, G. Kaur, M. Cen, V. Kulkarni, S. S. Islam, R. Spreitzer, S. Garag, A. Alduino, R. Chiou, L. Kamyab, S. Gupta, B. Xie, R. Appleton, S. Hollingsworth, S. McCargar, and Y. Akulova, *1.6 Tbps silicon photonics integrated circuit and 800 Gbps photonic engine for switch co-packaging demonstration*, *Journal of Lightwave Technology* **39** (2021), no. 4 1155–1161.

[5] T. J. Seok, K. Kwon, J. Henriksson, J. Luo, and M. C. Wu, *Wafer-scale silicon photonic switches beyond die size limit*, *Optica* **6** (2019), no. 4 490–494.

[6] J. Sun, E. Timurdogan, A. Yaacobi, E. S. Hosseini, and M. R. Watts, *Large-scale nanophotonic phased array*, *Nature* **493** (2013), no. 7431 195–199.

[7] C. V. Poulton, M. J. Byrd, B. Moss, E. Timurdogan, R. Millman, and M. R. Watts, *8192-element optical phased array with 100 steering range and flip-chip CMOS*, in *CLEO: Applications and Technology*, pp. JTh4A–3, OSA, 2020.

[8] J. Arrazola, V. Bergholm, K. Brádler, T. Bromley, M. Collins, I. Dhand, A. Fumagalli, T. Gerrits, A. Goussev, L. Helt, J. Hundal, T. Isacsson, R. Israel, J. Izaac, S. Jahangiri, R. Janik, N. Killoran, S. Sumar, J. Lavoie, A. Lita, D. Mahler, M. Menotti, B. Morrison, S. Nam, L. Neuhaus, H. Qi, N. Quesada, A. Repingon, K. Sabapathy, M. Schuld, D. Su, J. Swinarton, A. Sava, K. Tan, V. Vaidya, Z. Vernon, Z. Zabaneh, and Y. Zhang, *Quantum circuits with many photons on a programmable nanophotonic chip*, *Nature* **591** (2021), no. 7848 54–60.

[9] J. Feldmann, N. Youngblood, M. Karpov, H. Gehring, X. Li, M. Stappers, M. Le Gallo, X. Fu, A. Lukashchuk, A. S. Raja, J. Liu, C. Wright, A. Sebastian,

T. Kippenberg, W. Pernice, and H. Bhaskaran, *Parallel convolutional processing using an integrated photonic tensor core*, *Nature* **589** (2021), no. 7840 52–58.

[10] W. Jin, Q.-F. Yang, L. Chang, B. Shen, H. Wang, M. A. Leal, L. Wu, M. Gao, A. Feshali, M. Paniccia, *et. al.*, *Hertz-linewidth semiconductor lasers using CMOS-ready ultra-high-Q microresonators*, *Nature Photonics* **15** (2021), no. 5 346–353.

[11] J. F. Bauters, M. J. Heck, D. D. John, J. S. Barton, C. M. Bruinink, A. Leinse, R. G. Heideman, D. J. Blumenthal, and J. E. Bowers, *Planar waveguides with less than 0.1 dB/m propagation loss fabricated with wafer bonding*, *Optics Express* **19** (2011), no. 24 24090–24101.

[12] C. G. Roeloffzen, L. Zhuang, C. Taddei, A. Leinse, R. G. Heideman, P. W. van Dijk, R. M. Oldenbeuving, D. A. Marpaung, M. Burla, and K.-J. Boller, *Silicon nitride microwave photonic circuits*, *Optics Express* **21** (2013), no. 19 22937–22961.

[13] C. Xiang, M. L. Davenport, J. B. Khurgin, P. A. Morton, and J. E. Bowers, *Low-loss continuously tunable optical true time delay based on Si_3N_4 ring resonators*, *IEEE J. Sel. Top. Quantum Electron.* **24** (2017), no. 4 1–9.

[14] S. Srinivasan, R. Moreira, D. Blumenthal, and J. E. Bowers, *Design of integrated hybrid silicon waveguide optical gyroscope*, *Opt. Express* **22** (2014), no. 21 24988–24993.

[15] S. Gundavarapu, M. Belt, T. A. Huffman, M. A. Tran, T. Komljenovic, J. E. Bowers, and D. J. Blumenthal, *Interferometric optical gyroscope based on an integrated Si_3N_4 low-loss waveguide coil*, *Journal of Lightwave Technology* **36** (2018), no. 4 1185–1191.

[16] T. Huffman, M. Davenport, M. Belt, J. E. Bowers, and D. J. Blumenthal, *Ultra-low loss stitching for large-area waveguide based delay-line gyroscopes*, in *IEEE Photonics Conference*, pp. 478–479, IEEE, 2016.

[17] M. J. Van de Moosdijk, E. Van den Brink, K. Simon, A. Friz, G. N. Phillipps, R. J. Travers, and E. Raaymakers, *Collinearity and stitching performance on an ASML stepper*, in *Emerging Lithographic Technologies VI*, vol. 4688, pp. 858–866, SPIE, 2002.

[18] A. Milton and W. Burns, *Mode coupling in optical waveguide horns*, *IEEE Journal of Quantum Electronics* **13** (1977), no. 10 828–835.

Chapter 7

Deuterated silicon dioxide for heterogeneous integration of ultra-low-loss waveguides

Ultra low-loss waveguide fabrication typically requires high-temperature annealing beyond 1000 °C to reduce hydrogen content in deposited dielectric films. However, realizing the full potential of ultra low loss will require integration of active materials that cannot tolerate high temperature. Uniting ultra low-loss waveguides with on-chip sources, modulators, and detectors will require low-temperature, low-loss dielectric to serve as passivation and spacer layers for complex fabrication processes. We report a 250 °C deuterated silicon dioxide film for top cladding in ultra low-loss waveguides. Using multiple techniques, we measure propagation loss below 12 $\mathrm{dB\,m^{-1}}$ for the entire 1200 nm to 1650 nm range and top-cladding material absorption below 1 $\mathrm{dB\,m^{-1}}$ in the S, C, and L bands. The contents of this chapter were originally published as [1].

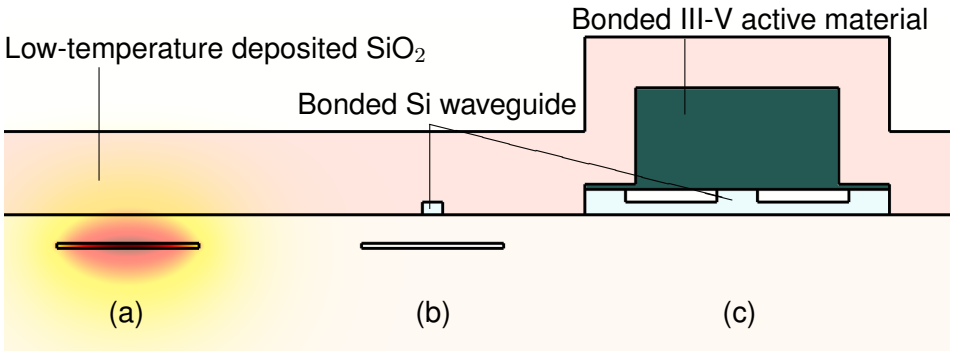

Figure 7.1: **Diagram of the heterogenous integration approach in [12] for the waveguide geometry used in this work.** (a) The ultra-low loss waveguide with its optical mode profile overlaid, (b) the silicon to ultra low-loss transition, and (c) the hybrid silicon/III-V active waveguide. Low temperature oxide, indicated above, is necessary for passivation and electrical routing after III-V material has been bonded. It must also have low optical loss, as it overlaps the mode of the ultra low-loss waveguide at (a). Reproduced from [1].

Introduction

Recent advances in ultra low-loss ($<10\,\mathrm{dB\,m^{-1}}$) waveguide technology have enabled photonic integrated circuit (PIC) demonstrations of a variety of applications typically in the domain of fiber and bulk optics, including narrow linewidth lasers [2, 3, 4, 5], optical gyroscopes [6, 7], and nonlinear optical frequency conversion [8, 9]. However, the majority of ultra low-loss devices require co-packaging with fiber [10] or active PICs [5, 4, 11], since integration of on-chip light sources is highly challenging. To date, the only technology capable of providing electrically-pumped light generation and detection to ultra low-loss devices on a single chip is heterogeneous integration of III-V semiconductor gain media [3, 12].

Through heterogeneous integration, active material is bonded above the passive waveguide so that light may couple vertically between active and passive layers. After the active material has been bonded, a strict thermal budget must be imposed for all following process steps, otherwise coefficient of thermal expansion mismatch with the substrate will cause proliferation of material defects in the gain medium [13, 14]. However, as shown in

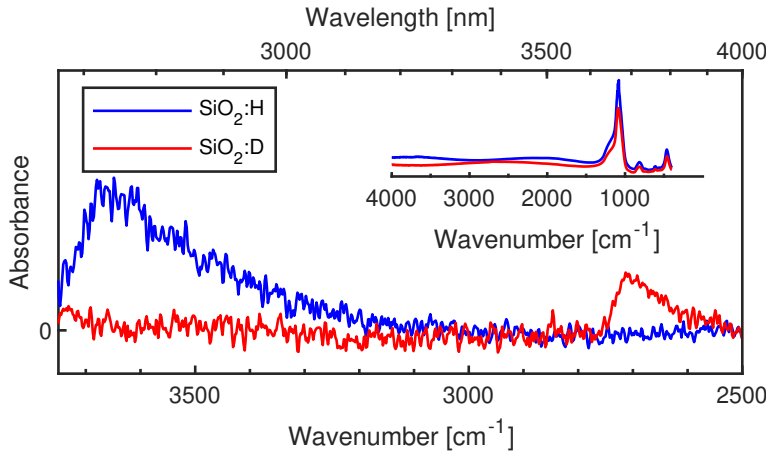

Figure 7.2: **Absorbance of SiO_2:H and SiO_2:D thin films by Fourier-transform infrared (FTIR) spectroscopy.** The fundamental SiO-H vibrational mode at 2.73 µm shifts to 3.74 µm for SiO-D. The full FTIR spectrum is shown in the inset. A model of the Fabry-Perot ripple was fitted over 2500 cm^{-1} to 4000 cm^{-1} and subtracted to reveal the absorption spectra of the fundamental vibrational modes of SiO-H and SiO-D as shown above. Reproduced from [1].

Fig. 7.1, any additional passivation or spacer dielectrics for electrical routing will become upper cladding for the low-loss waveguide, and must therefore exhibit low loss without the high temperature annealing typically required to reduce hydrogen content [15, 16]. This barrier to heterogeneous integration is especially severe for high aspect-ratio waveguides in which the optical mode is squeezed into the cladding to achieve losses below 1 dB m^{-1} [17, 2]. To integrate gain media with such devices without degrading performance, a low-loss, low-temperature deposited oxide cladding is required.

This problem is also relevant to the nonlinear integrated photonics community. As the field moves beyond the well-studied silicon nitride waveguide, promising new nonlinear platforms have emerged which require low-loss top cladding, but cannot tolerate high-temperature annealing. These include $LiNbO_3$ [9], AlGaAs [18], and GaP [19] on insulator, all formed by direct wafer bonding. It also includes Ta_2O_5 [20] which undergoes phase change at 650 °C. Furthermore, for integrated atomic clock applications, probing atomic resonances around 700 nm by frequency doubling will require eliminating

the SiO−H absorption at 1390 nm.

In this work, we explore plasma-enhanced chemical vapor deposited (PECVD) SiO_2 films from a deuterated silane (SiD_4) precursor. We choose the PECVD technique due to its ability to provide high-quality, conformal silicon dioxide films at low deposition temperature, as opposed to other chemical vapor deposition (CVD) techniques that require high temperature, or wafer bonding [17] which requires a planarized surface and so cannot provide a conformal coating. The main impact of the isotopic substitution of deuterium for hydrogen in the PECVD film is to shift the fundamental SiO−H absorption from its peak value at 2.73 µm to 3.74 µm, as shown in Fig. 7.2. In the near-infrared, the corresponding first overtone of this absorption shifts from 1390 nm to 1870 nm, reducing the material loss in the technologically important C and O telecommunications bands. A summary of known hydrogen-induced absorption peaks in SiO_2:H and their corresponding locations in SiO_2:D can be found in [21]. While deuteration has been used to deposit PECVD silicon nitride [22, 23], and to suppress O−H losses in optical fibers [21, 24], deuterated silicon dioxide (SiO_2:D) has yet to be thoroughly explored in the context of integrated photonics.

Experiment

We employ a silicon nitride waveguide with 90 nm thick and 2.8 µm wide core, which is single mode in the C band. Due to the high-aspect-ratio design, the mode (shown in Fig. 7.1a) has a large overlap with the cladding and low impact of sidewall roughness allowing for loss as low as $1\,\mathrm{dB\,m^{-1}}$ [15] — ideal for probing the intrinsic material loss limit of the SiO_2:D top cladding. We note that to measure the loss of the low-temperature top cladding, high temperature processes are used to prepare a low-loss lower cladding and core. To prepare the samples, 90 nm of stoichiometric Si_3N_4 is deposited via low-pressure

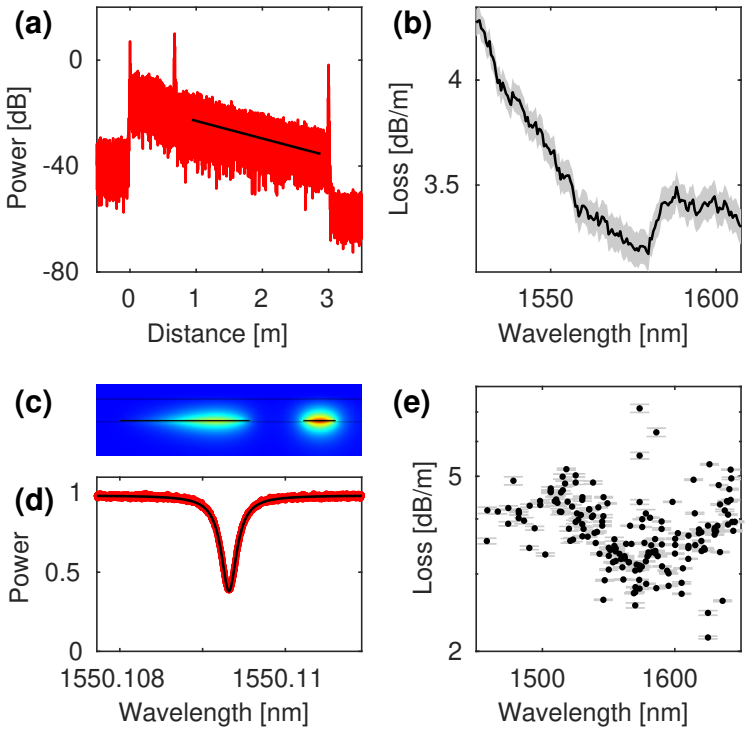

Figure 7.3: **Overview of OFDR and resonator loss measurement techniques.** (a) Fitting the slope of the backscattered OFDR signal as a function of distance allows for (b) measurement of waveguide loss as a function of wavelength. For the 2 m segment analyzed in (a), the fitting generates a 95 % confidence interval (CI) of $\pm 0.07\,\mathrm{dB\,m^{-1}}$ indicated by the shaded area in (b). Through design of the (c) resonator and coupler mode, and (d) fitting the optical linewidth, we demonstrate (e) robust fitting of multiple resonance spectra to measure spectral dependence of propagation loss, with mean 95 % CI of $\pm 0.025\,\mathrm{dB\,m^{-1}}$. Reproduced from [1].

chemical vapor deposition from dichlorosilane and ammonia precursors on 15 µm of thermal silicon dioxide at 800 °C. The silicon nitride layer is patterned using 248 nm deep UV lithography and inductively-coupled plasma (ICP) etching in $CHF_3/CF_4/O_2$ gas. Prior to top cladding deposition, the samples are annealed at 1050 °C for 7 h. We measured that this reduces the residual SiN−H overtone at 1520 nm from over 50 dB m^{-1} to about 1 dB m^{-1}. Finally, the low-temperature top cladding is deposited to a thickness of at least 1.5 µm by inductively-coupled plasma chemical vapor deposition. The deposition parameters were: 5 sccm SiH_4, 15 sccm O_2, 800 W ICP power, 0 W radio-frequency (RF) bias power, 5 mTorr chamber pressure, and 250 °C temperature. This recipe produces a film with refractive index of 1.459 at 632.8 nm and 1.451 at 1550 nm wavelength as measured by ellipsometry. After depositions with SiH_4 were complete, the line was evacuated and swapped to a SiD_4 gas cylinder with 99 % isotopic enrichment, and depositions were carried out with the same recipe parameters. The silane mass flow controller was not recalibrated after switching to SiD_4, as film parameters such as buffered oxide etch rate and refractive index were observed to be insensitive to minor changes in gas flow. Devices in the following configurations were prepared: (1) 2.8 µm wide waveguide with SiH_4-based top cladding, and length either 0.8 cm or 0.5 m, (2) 2.8 µm wide waveguide with SiD_4-based top cladding, and length 3 m, and (3) whispering-gallery ring resonators with SiD_4-based top cladding, designed with long, phase-matched pulley couplers [25] as shown in Fig. 7.3(c) for selective coupling to the fundamental mode in either the C or O bands. All devices were laid out with at least 1 mm bend radius to ensure negligible bend loss.

Finally, samples were diced into chips, and tested by edge coupling using cleaved fiber and index-matching gel with coupling loss of approximately 3 dB per facet. In order to measure waveguide loss, multiple techniques, each with unique benefits and drawbacks, were used to probe the loss at various wavelengths. By comparing them, we were able

to obtain loss estimates with high accuracy and spectral resolution.

- Optical frequency domain reflectometry (OFDR) (Luna OBR 4400 and 4413) was used to measure propagation loss over 1525 nm to 1610 nm and 1280 nm to 1340 nm. Spectral data was obtained by analyzing the backscatter signal in 5 nm windows at 0.5 nm increments, shown in Fig. 7.3(a-b). OFDR provides an accurate measurement of propagation loss that is independent of coupling loss to the chip, however precision is proportional to the propagation distance and can require prohibitively long lengths due to the stochastic nature of distributed backscatter.

- Ring resonator linewidth was measured using a tunable laser (Keysight 81608A) and photodetector over 1240 nm to 1380 nm and 1450 nm to 1650 nm. By fitting the lineshape of under-coupled ring resonators, accurate measures of propagation loss could be obtained in wavelength ranges where OFDR was not available. As shown in Fig. 7.3(d-e), the uncertainty introduced by fitting is negligible. Instead, the precision of the measurement was limited by phase noise of the laser, which caused jitter in the tuning rate. This source of noise can be addressed by simultaneous use of an interferometer to correct the tuning rate [10].

- Tunable laser (TL) (Keysight 81608A) transmission spectrum over 1240 nm to 1380 nm and 1450 nm to 1650 nm was able to resolve fine spectral features. However, due to uncertainty in the coupling loss it was necessary to reference this data to more accurate measurements such as OFDR and ring resonator linewidth. Broadband spectral dependence of coupling loss also distorts the data.

- Superluminescent diode (SLED) transmission spectra, spanning 1200 nm to 1700 nm and measured with optical spectrum analyzer (OSA) (Yokogawa AQ6370C), provided broadband estimates of waveguide loss. However, difficulty of obtaining con-

sistent coupling to the chip over a broad wavelength span, as well as environmental perturbations due to long scanning duration required to improve OSA sensitivity, led to severe uncertainty in coupling loss to the chip, in particular large spectral variability of the coupling loss. As such, while the spectra produced by this method provide qualitative insight into resonance wavelength and magnitude, the accuracy is poor when fiber-to-chip coupling losses greatly exceed accumulated propagation loss within the waveguide. This problem is more acute in spectral windows where the propagation loss is low.

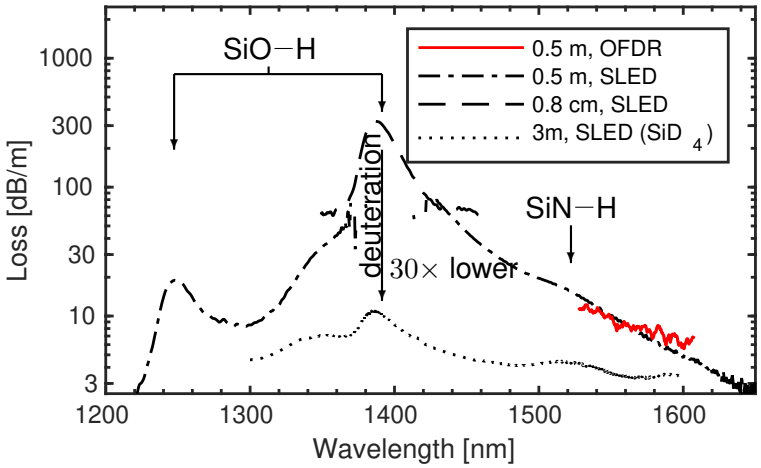

Figure 7.4: **Waveguide loss with top cladding from SiH_4 precursor.** Uniform offsets were applied to the SLED transmission spectra to obtain approximate agreement with OFDR-measured loss in the C-band. We also show the loss from SiD_4 precursor (reproduced from Fig. 7.5) to demonstrate 30× reduction at the 1390 nm peak. Reproduced from [1].

The data obtained by these techniques are summarized for SiO_2:H top cladding in Fig. 7.4, and SiO_2:D top cladding in Fig. 7.5, with a comparison of the two in Fig. 7.4. In particular, we observe that the loss from the SiO−H overtone at 1390 nm is thirty times lower, reduced from 300 dB m^{-1} to 10 dB m^{-1}. We attribute the residual absorption at this wavelength to isotopic impurity of the source and trace H_2O contamination within the chamber. Regarding the other absorption features, deuteration shifts the 1240 nm

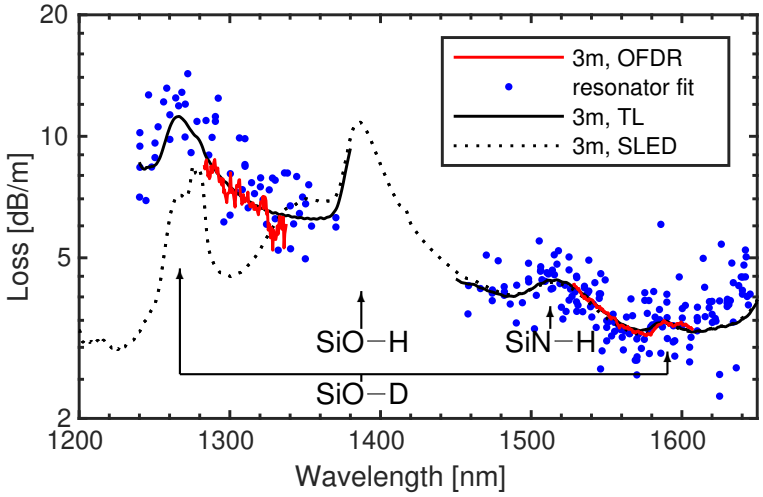

Figure 7.5: **Waveguide loss with top cladding from SiD_4 precursor.** Uniform offsets were applied to SLED and TL transmission spectra to obtain approximate agreement with OFDR and ring resonator data in C and O bands. Reproduced from [1].

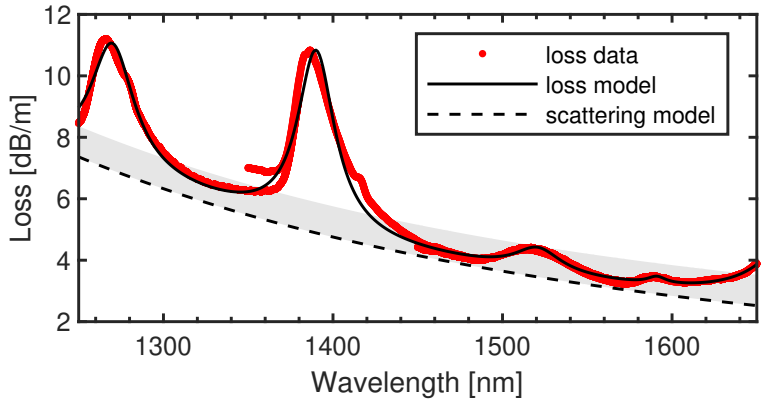

Figure 7.6: **A simple model including scattering and material losses** was fitted to data from Fig. 7.5 for waveguides with deuterated top cladding. The region above the scattering model has been shaded to indicate where the material loss is below $1\,\mathrm{dB\,m^{-1}}$. The scattering loss follows a $1/\lambda^p$ dependence where $p = 3.86 \pm 0.04$, while each absorption is approximately modeled by a Lorentzian resonance (95 % CI, $R^2 = 0.99$). Reproduced from [1].

SiO_2:H resonance, visible in Fig. 7.4, to 1680 nm [21], the tail of which is visible in Fig. 7.5. SiO_2:H absorption lines at 950 nm and 1130 nm are shifted to 1270 nm and 1580 nm following deuteration [21], as observed in Fig. 7.5. Common to both of Fig. 7.4, and Fig. 7.5 is the residual 1520 nm SiN−H overtone absorption [22, 23] due to the waveguide core.

To infer the relative contributions of scattering loss and material absorption loss, we fit an approximate model to the data in Fig. 7.5. We adopt a scattering loss model $\alpha_{\mathrm{sc}} \propto 1/\lambda^p$ where α_{sc} is the scattering component of propagation loss, λ is the wavelength, and p is a fitted parameter. Based on analytical scattering models, we expect $p \approx 4$ [15]. In addition, we also fit a Lorentzian distribution to each of the absorption peaks around 1270 nm, 1390 nm, 1520 nm, 1580 nm, and 1680 nm. As the O−H absorption feature in reality consists of multiple overlapping vibrational modes [26], a Lorentzian fit to a single line has limited accuracy. Nonetheless, an adequate fit to the data was obtained, as shown in Fig. 7.6. We conclude that in the transmission windows 1310 nm to 1360 nm and 1440 nm to 1630 nm, the majority of propagation loss is due to scattering, with material absorption contributing below $1\,\mathrm{dB\,m^{-1}}$. We note that the 1520 nm peak contributing approximately $1\,\mathrm{dB\,m^{-1}}$ is associated with the core, rather than the top cladding. Furthermore, as shown in Fig. 7.5, the loss measured by OFDR in a single-mode waveguide (2.8 µm width) agrees closely with the loss extracted from resonance fitting of whispering gallery mode resonators (12 µm width). Since sidewall scattering loss typically falls with increasing waveguide width [27], we conclude sidewall scattering is negligible, and that the scattering loss is mostly due to roughness at the top surface of the waveguide core ($R_{\mathrm{q}} = 0.4$ nm).

Discussion

As the field of integrated photonics matures, it will move beyond the communications O, S, C, and L wavelength bands studied in this manuscript. In particular, the visible and near-visible wavelength ranges of 0.4 µm to 1.0 µm will be of interest for applications involving quantum information [28] and frequency stabilization to atomic resonances [29]. Nonetheless, we believe that the low-temperature, low-loss cladding material developed in this work will prove critical to heterogeneous integration of frequency-doubling based approaches [29], as such systems will still require ultra-low loss in the near infrared. However, we expect that deuteration will provide reduced benefit to propagation loss in the near-visible, since O−H absorption bands in this spectral range correspond to orders-of-magnitude weaker fourth and fifth harmonic overtones of the O−H bond resonances, rather than second and third harmonic overtones in the near infrared [30, 21]. Rather, we expect losses in this range to dominated by scattering losses due to the $1/\lambda^4$ dependence of scattering loss on wavelength as discussed above.

In conclusion, we have demonstrated a high quality, 250 °C SiO_2 film for use as top cladding in ultra-low-loss waveguides. In high-aspect-ratio silicon nitride, we measured a total propagation loss below $5\,\mathrm{dB\,m^{-1}}$ and material absorption loss below $1\,\mathrm{dB\,m^{-1}}$ across the entire S, C, and L bands without annealing after top cladding deposition. We believe this approach will be critical for integration of active III-V material with ultra-low loss waveguides and other platforms with limited thermal budget, thereby enabling a new generation of compact, all-on-chip narrow linewidth lasers, sensors, and nonlinear devices.

Bibliography

[1] W. Jin, D. D. John, J. F. Bauters, T. Bosch, B. J. Thibeault, and J. E. Bowers, *Deuterated silicon dioxide for heterogeneous integration of ultra-low-loss waveguides*, *Optics Letters* **45** (2020), no. 12 3340–3343.

[2] S. Gundavarapu, G. M. Brodnik, M. Puckett, T. Huffman, D. Bose, R. Behunin, J. Wu, T. Qiu, C. Pinho, N. Chauhan, *et. al.*, *Sub-Hertz fundamental linewidth photonic integrated Brillouin laser*, *Nature Photonics* **13** (2019), no. 1 60–67.

[3] D. Huang, M. A. Tran, J. Guo, J. Peters, T. Komljenovic, A. Malik, P. A. Morton, and J. E. Bowers, *High-power sub-kHz linewidth lasers fully integrated on silicon*, *Optica* **6** (2019), no. 6 745–752.

[4] C. Xiang, P. A. Morton, and J. E. Bowers, *Ultra-narrow linewidth laser based on a semiconductor gain chip and extended si_3n_4 Bragg grating*, *Optics letters* **44** (2019), no. 15 3825–3828.

[5] Y. Fan, A. van Rees, P. J. Van der Slot, J. Mak, R. M. Oldenbeuving, M. Hoekman, D. Geskus, C. G. Roeloffzen, and K.-J. Boller, *Hybrid integrated inp-si 3 n 4 diode laser with a 40-hz intrinsic linewidth*, *Opt. Express* **28** (2020), no. 15 21713–21728.

[6] Y.-H. Lai, M.-G. Suh, Y.-K. Lu, B. Shen, Q.-F. Yang, H. Wang, J. Li, S. H. Lee, K. Y. Yang, and K. Vahala, *Earth rotation measured by a chip-scale ring laser gyroscope*, *Nat. Photon.* **14** (2020) 345–349.

[7] S. Gundavarapu, M. Belt, T. A. Huffman, M. A. Tran, T. Komljenovic, J. E. Bowers, and D. J. Blumenthal, *Interferometric optical gyroscope based on an*

integrated Si_3N_4 low-loss waveguide coil, *Journal of Lightwave Technology* **36** (2018), no. 4 1185–1191.

[8] T. J. Kippenberg, A. L. Gaeta, M. Lipson, and M. L. Gorodetsky, *Dissipative Kerr solitons in optical microresonators*, *Science* **361** (2018), no. 6402.

[9] M. Zhang, B. Buscaino, C. Wang, A. Shams-Ansari, C. Reimer, R. Zhu, J. M. Kahn, and M. Loncar, *Broadband electro-optic frequency comb generation in a lithium niobate microring resonator*, *Nature* **568** (2019), no. 7752 373–377.

[10] K. Y. Yang, D. Y. Oh, S. H. Lee, Q.-F. Yang, X. Yi, B. Shen, H. Wang, and K. Vahala, *Bridging ultrahigh-Q devices and photonic circuits*, *Nature Photonics* **12** (2018), no. 5 297–302.

[11] B. Stern, X. Ji, Y. Okawachi, A. L. Gaeta, and M. Lipson, *Battery-operated integrated frequency comb generator*, *Nature* **562** (2018), no. 7727 401.

[12] C. Xiang, W. Jin, J. Guo, J. D. Peters, M. Kennedy, J. Selvidge, P. A. Morton, and J. E. Bowers, *Narrow-linewidth III-V/Si/Si_3N_4 laser using multilayer heterogeneous integration*, *Optica* **7** (2020), no. 1 20–21.

[13] T. Fujii, T. Sato, K. Takeda, K. Hasebe, T. Kakitsuka, and S. Matsuo, *Epitaxial growth of InP to bury directly bonded thin active layer on SiO_2/Si substrate for fabricating distributed feedback lasers on silicon*, *IET Optoelectronics* **9** (2015), no. 4 151–157.

[14] M. L. Davenport, *Heterogeneous silicon III-V mode-locked lasers*. PhD thesis, UC Santa Barbara, 2017.

[15] J. F. Bauters, M. J. Heck, D. John, D. Dai, M.-C. Tien, J. S. Barton, A. Leinse,

R. G. Heideman, D. J. Blumenthal, and J. E. Bowers, *Ultra-low-loss high-aspect-ratio Si_3N_4 waveguides*, *Optics Express* **19** (2011), no. 4 3163–3174.

[16] M. H. Pfeiffer, J. Liu, A. S. Raja, T. Morais, B. Ghadiani, and T. J. Kippenberg, *Ultra-smooth silicon nitride waveguides based on the Damascene reflow process: fabrication and loss origins*, *Optica* **5** (2018), no. 7 884–892.

[17] J. F. Bauters, M. J. Heck, D. D. John, J. S. Barton, C. M. Bruinink, A. Leinse, R. G. Heideman, D. J. Blumenthal, and J. E. Bowers, *Planar waveguides with less than 0.1 dB/m propagation loss fabricated with wafer bonding*, *Optics Express* **19** (2011), no. 24 24090–24101.

[18] L. Chang, W. Xie, H. Shu, Q.-F. Yang, B. Shen, A. Boes, J. D. Peters, W. Jin, C. Xiang, S. Liu, G. Moille, S.-P. Yu, X. Wang, K. Srinivasan, S. B. Papp, K. Vahala, and J. E. Bowers, *Ultra-efficient frequency comb generation in AlGaAs-on-insulator microresonators*, *Nature Communications* **11** (2020) 1331.

[19] D. J. Wilson, K. Schneider, S. Hönl, M. Anderson, Y. Baumgartner, L. Czornomaz, T. J. Kippenberg, and P. Seidler, *Integrated gallium phosphide nonlinear photonics*, *Nature Photonics* **14** (2020), no. 1 57–62.

[20] S.-P. Yu, D. C. Cole, H. Jung, G. T. Moille, K. Srinivasan, and S. B. Papp, *Spontaneous pulse formation in edge-less photonic crystal resonators*, *arXiv preprint arXiv:2002.12502* (2020).

[21] M. Nakahara, Y. Ohmori, and H. Itoh, *Loss increase in deuterium-doped VAD fibres with heat treatment*, *Electronics Letters* **20** (1984), no. 8 327–329.

[22] F. G. Johnson, O. S. King, J. V. Hryniewicz, L. G. Joneckis, S. T. Chu, and D. M.

Gill, *Use of deuterated gases for the vapor deposition of thin films for low-loss optical devices and waveguides*, Sept. 2, 2003. US Patent 6,614,977.

[23] J. Chiles, N. Nader, D. D. Hickstein, S. P. Yu, T. C. Briles, D. Carlson, H. Jung, J. M. Shainline, S. Diddams, S. B. Papp, S. W. Nam, and R. P. Mirin, *Deuterated silicon nitride photonic devices for broadband optical frequency comb generation*, *Optics letters* **43** (2018), no. 7 1527–1530.

[24] J. Stone, *Interactions of hydrogen and deuterium with silica optical fibers: A review*, *Journal of Lightwave technology* **5** (1987), no. 5 712–733.

[25] D. T. Spencer, J. F. Bauters, M. J. Heck, and J. E. Bowers, *Integrated waveguide coupled Si_3N_4 resonators in the ultrahigh-Q regime*, *Optica* **1** (2014), no. 3 153–157.

[26] G. A. Thomas, B. I. Shraiman, P. F. Glodis, and M. J. Stephen, *Towards the clarity limit in optical fibre*, *Nature* **404** (2000), no. 6775 262–264.

[27] D. Marcuse, *Theory of dielectric optical waveguides*. Acad. Press, 1974.

[28] T. Chanelière, D. Matsukevich, S. Jenkins, S.-Y. Lan, T. Kennedy, and A. Kuzmich, *Storage and retrieval of single photons transmitted between remote quantum memories*, *Nature* **438** (2005), no. 7069 833–836.

[29] W. Zhang, L. Stern, D. Carlson, D. Bopp, Z. Newman, S. Kang, J. Kitching, and S. B. Papp, *Ultranarrow linewidth photonic-atomic laser*, *Laser & Photonics Reviews* **14** (2020), no. 4 1900293.

[30] P. Kaiser, A. Tynes, H. Astle, A. Pearson, W. French, R. Jaeger, and A. Cherin, *Spectral losses of unclad vitreous silica and soda-lime-silicate fibers*, *JOSA* **63** (1973), no. 9 1141–1148.

Chapter 8

Piezoelectrically tuned silicon nitride resonator

Typical integrated optical phase tuners alter the effective index. In this chapter, we explore tuning by geometric deformation. We show that tuning efficiency, $V_\pi L$, improves as the device size shrinks down to the optimal bend radius, contrary to conventional index-shift based approaches where $V_\pi L$ remains constant. We demonstrate that this approach is capable of ultra-low power tuning across a full FSR in a low-confinement silicon nitride based ring resonator of 580 µm radius. We demonstrate record performance with $V_{\mathrm{FSR}} = 16\,\mathrm{V}$, $V_\pi L = 3.6\,\mathrm{V\,dB}$, $V_\pi L\alpha = 1.1\,\mathrm{V\,dB}$, tuning current below 10 nA, and unattenuated tuning response up to 1 MHz. We also present optimized designs for high confinement silicon nitride and silicon based platforms with radius down to 80 µm and 45 µm, respectively, with performance well beyond current state-of-the-art. Applications include narrow-linewidth tunable diode lasers for spectroscopy and non-linear optics, optical phased array beamforming networks for RF antennas and LIDAR, and optical filters for WDM telecommunication links. The contents of this chapter were orignally published as [1].

Introduction

Ultra-low loss integrated photonic platforms are universally hamstrung by a lack of effective phase tuning mechanisms. The typical thermo-optic tuning approach requires 1 mW to 100 mW per free spectral range (FSR) per device in silicon-based platforms [2, 3], and 200 mW to 500 mW per FSR per device in silicon nitride-based platforms [4]. Electro-optic or charge-carrier-based approaches tend to increase propagation loss and degrade device performance. Demonstrations of tuning by the photoelastic effect show low propagation losses and low tuning power, however the effect is weak, requiring impractically long devices to tune by a full FSR [5, 6]. Real-world optical beamforming networks for RF antennas [7, 8] would require thousands of devices [4], so low tuning power, low optical loss, and small size are required for practical applications. In this work, we will show that all three requirements may be simultaneously satisfied by a purely geometric tuning approach. We demonstrate this by incorporating a PZT thin film piezoelectric actuator with suspended waveguides. In what follows, we will present the theory, detailed analysis of the design, and comparison with current state of the art.

Theory

Within an optical resonator, the resonance condition is expressed as

$$Ln_{\text{eff}} = m\lambda \tag{8.1}$$

where L is the round-trip device length, n_{eff} the effective index of the optical mode, λ the free-space wavelength, m the longitudinal mode number and a positive integer. This results in a periodic array of resonance wavelengths, with spacing given by the free

spectral range (FSR)

$$\Delta\lambda_{\mathrm{FSR}} = \frac{\lambda^2}{n_{\mathrm{g,eff}} L} \tag{8.2}$$

where $n_{\mathrm{g,eff}}$ is the effective group index. Tunability by an FSR, representing a 2π phase shift, is a critical metric, as it allows for aligning a resonance to any arbitrary wavelength. Equivalently, tuning by an FSR corresponds to changing the longitudinal mode number by exactly 1 for fixed wavelength, that is,

$$\Delta m = 1 \tag{8.3}$$

$$\Delta\lambda = 0 \tag{8.4}$$

Differentiating Eq. (8.1), and substituting Eq. (8.3) and Eq. (8.4), we obtain

$$L\Delta n_{\mathrm{eff}} + n_{\mathrm{eff}}\Delta L = \lambda \tag{8.5}$$

Typical approaches to tuning employ the first term on the left hand side of Eq. (8.5). Instead, we target the second term on the left hand side of Eq. (8.5). By fabricating a piezoelectric actuator on a suspended membrane containing an optical ring resonator, we form a radially symmetric unimorph cantilever structure, shown in Fig. 8.1. In a piezoelectric material, electric fields are related to mechanical deformation through [9, 10].

$$T = -\underline{e}E + c^E S \tag{8.6}$$

$$D = eS + \epsilon^S E \tag{8.7}$$

where e and $\underline{e}$ are piezoelectric stress tensors, S the strain tensor, T the stress tensor, c^E the stiffness tensor, D the electrical displacement vector, E the electric field vector, and ϵ^S the dielectric permittivity tensor. With the application of an electric field across

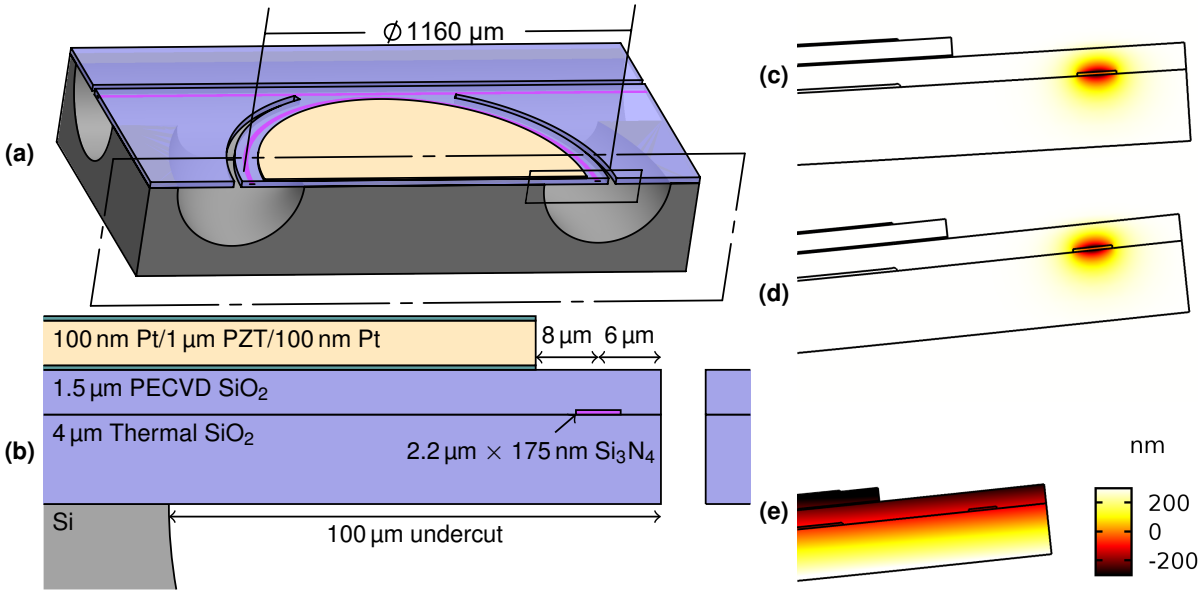

Figure 8.1: **Geometry for fabricated devices.** Undercut of the ring allows the resonator to deform, straining the waveguide and tuning the optical resonance. (a) The geometry is roughly symmetric about the dashed cross-section plane. Devices were designed with two coupled bus waveguides in the add-drop configuration. (b) Detail view of the area denoted by solid rectangle in (a). Simulated TM optical mode profile and device shape under 0V (c) and 16V (d) applied bias to PZT actuator. (e) radial displacement in nm between (c) and (d). Reproduced from [1].

the actuator, an in-plane contraction of the piezoelectric causes the structure to curl upwards (Fig. 8.1(c), 8.1(d)). This upwards displacement is accompanied by a radial displacement, ΔR, (Fig. 8.1(e)), and corresponding contraction in the path length of the ring resonator, ΔL, given by

$$\Delta L = 2\pi\Delta R \tag{8.8}$$

Ignoring any perturbation to the effective index ($\Delta n_{\text{eff}} = 0$), and substituting Eq. (8.8) into Eq. (8.5) we observe that the required radial displacement for tuning by an FSR is in fact independent of device size and is given by

$$\Delta R = \frac{\lambda}{2\pi n_{\text{eff}}} \tag{8.9}$$

To explore the relationship between tuning efficiency and device size, we consider a fixed cross sectional geometry (as in Fig. 8.1(b)), fixed tuning voltage, and fixed released membrane distance, changing only the bend radius. We note that even a device approaching infinite bend radius (corresponding to a straight waveguide) still experiences a radial (i.e. lateral) displacement under applied voltage that is identical to the lateral displacement of a unimorph cantilever beam with the same cross-section. Thus, in the limit of large bend radii, we expect the radial displacement to be independent of device radius.

Since the required radial displacement for tuning by an FSR in Eq. (8.9), and the radial displacement itself are both independent of device radius, we conclude that a device design tunable by an FSR remains tunable by an FSR as device size is reduced, so long as the bend radius is large. However, since FSR grows as the device size is reduced in Eq. (8.2), this leads to the counterintuitive result that the tuning range of the device actually improves as the device size is reduced. When the device radius

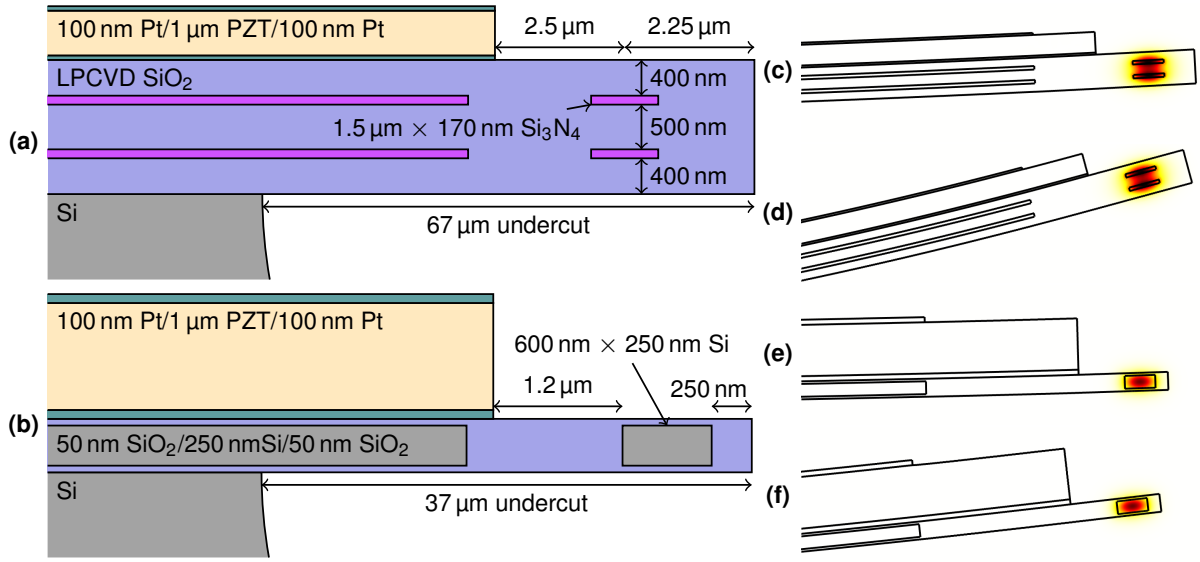

Figure 8.2: **Geometry for proposed devices.** (a) cross-sectional geometry based on dual strip SiN waveguide of [11]. (b) cross-sectional geometry based on deeply etched SOI waveguides. TE mode within the dual-strip nitride waveguide under 0V (c) and 30V (d) bias. TE mode within the silicon waveguide under 0V (e) and 30V (f) bias. Reproduced from [1].

becomes comparable to the released distance, the structure will stiffen as the radius is further reduced and eventually the ratio of tuning range to FSR will fall. We show in the following section that there is an optimal bend radius, on the order of the release distance, for which the absolute tuning range is maximized.

In contrast, tuning caused by electro-optic effect is linearly proportional to applied voltage and interaction length, leading to a natural figure of merit $V_\pi L$ which remains constant as device length is changed, where V_π is the voltage required to induce a π phase shift. Borrowing this same figure of merit, we find that in the large radius limit of this proposed structure, $V_\pi L$ in fact decreases proportionally as we reduce the device length, and it is V_π that remains constant.

Design

To demonstrate this principle, we select the high-aspect-ratio Si_3N_4 waveguide platform of [12]. However, since we hope to induce a significant geometric deformation of the structure, we choose thinner upper and lower claddings of 1.5 µm and 4 µm, respectively. For the piezoelectric we select PZT due to its large piezoelectric coefficient $e_{31,f}$ of $-8\,\mathrm{C\,m^{-2}}$ to $-12\,\mathrm{C\,m^{-2}}$, an order of magnitude better than other readily available strongly piezoelectric materials such as AlN ($e_{31,f} = -1.05\,\mathrm{C\,m^{-2}}$) or ZnO ($e_{31,f} = -1.00\,\mathrm{C\,m^{-2}}$) [13]. The designed geometry and mode profile of the fabricated structure is shown in Fig. 8.1(a), 8.1(b), 8.1(c). To explore the limits of the approach, we will also consider the dual-stripe Si_3N_4 platform of [11], and a deeply etched silicon-on-insulator (SOI) waveguide platform, shown in Fig. 8.2(a) and 8.2(b), respectively. For each design we choose a fixed undercut distance and maximum applied voltage, and simulate the tuning range as a function of bend radius. Finite-element-method simulations were carried out at 1550 nm in cylindrically symmetric geometry, incorporating simultaneous effects of mechanical deformation as well as photoelastic index shift. The photoelastic coefficients of amorphous Si_3N_4 are unknown in the literature; as a coarse approximation, they were assumed equal to the photoelastic coefficients of SiO_2. The photoelastic coefficients of SiO_2 used were $p_{11} = 0.121$, $p_{12} = 0.270$, $p_{44} = -0.075$ [14], whereas the photoelastic coefficients of Si used were $p_{11} = -0.094$, $p_{12} = 0.017$, $p_{44} = -0.051$ [15]. Otherwise, standard literature values for the mechanical and optical properties of Si, SiO_2, Si_3N_4, Pt, and PZT-5H were used. For the design of Fig. 8.1, 16 V was chosen as the simulation voltage, as it was the voltage for which we demonstrated tuning by a full FSR. For the other designs, a simulation voltage of 30 V was chosen, for a field of $300\,\mathrm{kV\,cm^{-1}}$ consistent with the dielectric strength of high quality PZT films [16, 17, 18].

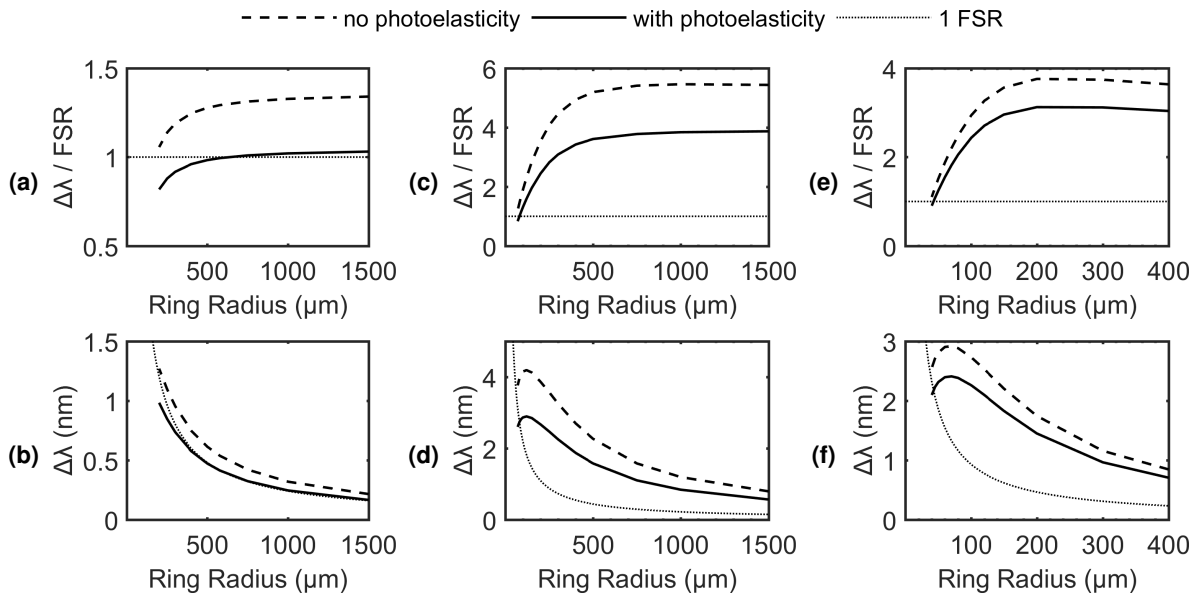

Figure 8.3: **Simulated tuning range versus ring radius for fixed undercut distance and voltage for each design.** Tuning range as (a) a fraction of FSR and (b) in nm for the fabricated single-stripe nitride waveguide design (100 µm undercut, 16 V bias). Tuning range as (c) a fraction of FSR and (d) in nm for the proposed dual-stripe design (67 µm undercut, 30 V bias). Tuning range as (e) a fraction of FSR and (f) in nm for the proposed Si waveguide design (37 µm undercut, 30 V bias). In each case, the tuning penalty due to photoelastic effect is between 15 % to 30 % of the total tuning range. When expressed as a fraction of FSR in (a), (c), and (e), the tuning range is independent of ring radius for large radii. When expressed in absolute terms in (b), (d), and (f), the tuning range tends to improve as ring radius shrinks. Reproduced from [1].

Table 8.1: **Parameters and results for the simulations shown in Fig. 8.3.** For each design, we determine the minimum bend radius tunable by a full FSR. At this minimum bend radius, we also simulate the fundamental mechanical resonance frequency to determine the maximum tuning speed. Reproduced from [1].

Platform	Simulation parameters	Minimum bend radius	Fundamental mechanical resonance
Single-stripe Si_3N_4	100 µm undercut 16 V bias	580 µm	550 kHz at 0 V 550 kHz at 16 V
Dual-stripe Si_3N_4	67 µm undercut 30 V bias	80 µm	500 kHz at 0 V 720 kHz at 30 V
SOI	37 µm undercut 30 V bias	45 µm	780 kHz at 0 V 1100 kHz at 30 V

In Fig. 8.3(a), 8.3(c), 8.3(e), we observe that the ratio of wavelength tuning to FSR is independent of bend radius when the radius is much larger than the undercut distance, consistent with our prediction of constant V_π for large radii. However, even as the radius approaches the undercut distance, the wavelength tuning range continues to improve, as shown in Fig. 8.3(b), 8.3(d), 8.3(f). Tuning efficiency improves as the device shrinks. To quantify the impact of the photoelastic effect, the same simulations have been performed setting photoelastic constants $p_{11} = p_{12} = p_{44} = 0$, and the results displayed by the dashed traces in Fig. 8.3. In all cases, the photoelastic effect represents a tuning penalty ranging from 15 % to 30 % of the total tuning range, represented by the difference between solid and dashed traces in Fig. 8.3. For each design, a minimum bend radius tunable by a full FSR was determined, shown in Table 8.1. For released membranes under net compressive stress, buckling of the membrane may occur [19]. For the minimum bend radius of each design, a full 3D solid mechanics simulation was performed to confirm that the membranes do not buckle for the range of applied voltages, which would negatively

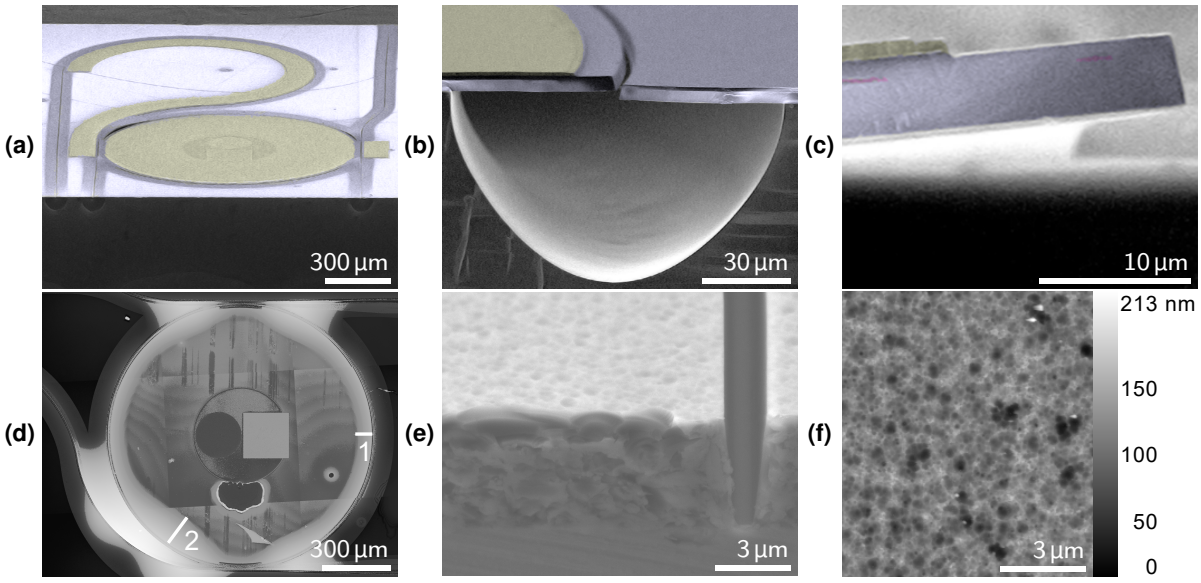

Figure 8.4: **Fabricated device images.** SEM (colorized) images have been tinted: actuator-yellow, SiO_2-blue, Si_3N_4-magenta. (a) SEM image – oblique view. (b) Cleaved ring resonator. (c) Cleaved waveguide core. (d) Height map by confocal microscopy with image stitching. The color scale is non-linear, to emphasize vertical displacement at the actuator surface. The distances marked 1 and 2, 75 µm and 155 µm respectively, indicate the approximate undercut in those regions. (e) SEM image of cladding, left rough by PZT actuator processing, adjacent to an etched trench and diced facet. (f) AFM heightmap of rough upper surface. The rough surface impacts propagation loss, but process optimizations should remedy it. Reproduced from [1].

impact tunability.

To characterize the tuning speed of the structures, we perform eigenfrequency studies within the cylindrically symmetric geometry. From the data tabulated in Table 8.1, we observe that the mechanical resonance shifts to higher frequencies with applied DC bias, an effect we attribute to the stress in the PZT causing a stiffening of the structure. For each design, the resonant frequency of the fundamental vibrational mode is between 500 kHz to 1000 kHz. This represents an upper bound on the highest frequency component present in the driving electrical signal for quasi-static operation. Through direct digital synthesis and low pass RF filtering of the driving signal, we expect a switching time of 1 µs to 10 µs may be achieved.

Fabrication

The fabrication of waveguides begins by forming a 4 µm thick lower cladding by thermal oxidation of a 100 mm diameter prime Si wafer. 175 nm of stoichiometric Si_3N_4 is deposited by low-pressure chemical vapor deposition. The 2.2 µm wide waveguide core is defined by deep ultra-violet lithography and etched by inductively-coupled-plasma (ICP) reactive ion etch (RIE) with $CHF_3/O_2/CF_4$ gases. An upper cladding of SiO_2 is formed by plasma-enhanced chemical vapor deposition (PECVD), and annealed at 1050 °C for seven hours.

The fabrication of the actuator [20] begins by planarizing the top cladding by chemical-mechanical polishing to 1.5 µm thickness. This step is critical to ensuring crack-free deposition of the PZT. To form the actuator, Ti is sputtered and oxidized to form a 35 nm seed layer of TiO_2 [21]. This forms a template to sputter a 100 nm Pt lower electrode. A PZT film with a Zr/Ti ratio of 52/48 is then deposited by chemical solution deposition (CSD) [20, 22, 23] and heated to 700 °C for 2 minutes by rapid thermal annealing in flowing oxygen to crystallize the film. The process is repeated several times to form a 1 µm thick, (001) oriented polycrystalline film, with grain size on the order 100 nm. The actuator is capped by a 100 nm Pt top electrode and patterned in three RIE steps by C_4F_8/Cl_2 gases. The first step etches the top electrode. The second step etches through the PZT and lower electrode to stop on SiO_2. The third step etches through the PZT to access the lower electrode. Next, a contact metallization comprised of 730 nm Au/20 nm Pt/20 nm Ti is deposited by electron beam evaporation and patterned by lift-off.

Finally, deep trenches are etched adjacent to the waveguides through the SiO_2 to access the Si substrate for release using ICP RIE with CHF_3 etch gas. The wafers are diced and the facets polished and coated by ion-beam deposition with a 250 nm layer of SiO_2. In the final step prior to testing and measurement, XeF_2 gas etches the exposed Si

substrate through the deep trenches in order to undercut and release the waveguides.

Experiment

Images of fabricated devices are shown in Fig. 8.4. Until now, we have considered only perfectly radially symmetric geometries. However, a practical ring resonator requires a bus waveguide to couple light into the ring. To achieve this, the release trench along the circumference of the resonator is interrupted, so that a bus waveguide may be run adjacent to the ring waveguide. The bus waveguide itself is also released to avoid leakage of the optical mode into the substrate. Due to intrinsic stress gradients within the oxide cladding and stress mismatch between oxide and the actuator, the released structure curls upwards and the waveguide core rotates, as demonstrated by simulation in Fig. 8.1(c), 8.1(d), and real device in Fig. 8.4(c). The height map in Fig. 8.4(d) reveals that the release distance is not uniform, due to irregular structure of the trenches through which XeF_2 gas etches the silicon substrate isotropically for release. The undercut adjacent to the coupling regions, marked 2 in Fig. 8.4(d), is greater than 155 µm, more than double the distance in regions spatially distant from coupling regions, marked as 1 in Fig. 8.4(d), of about 75 µm.

The static tuning of the TM mode resonance as a function of applied voltage for the best device is shown in Fig. 8.5(a). For the measurement, a tunable laser source was coupled into on-chip waveguides through edge facets, and the response was measured by a photodetector at the through port. Electrodes were contacted by DC probes, and the spectrum was measured at each voltage bias. The device is tuned by a full FSR at 16 V applied bias, consistent with a simulated resonator of 100 µm uniform undercut distance. In this device, however, the undercut, measured indirectly as in Fig. 8.4(d), was greater than 200 µm adjacent the coupling region, and about 86 µm away from the coupling

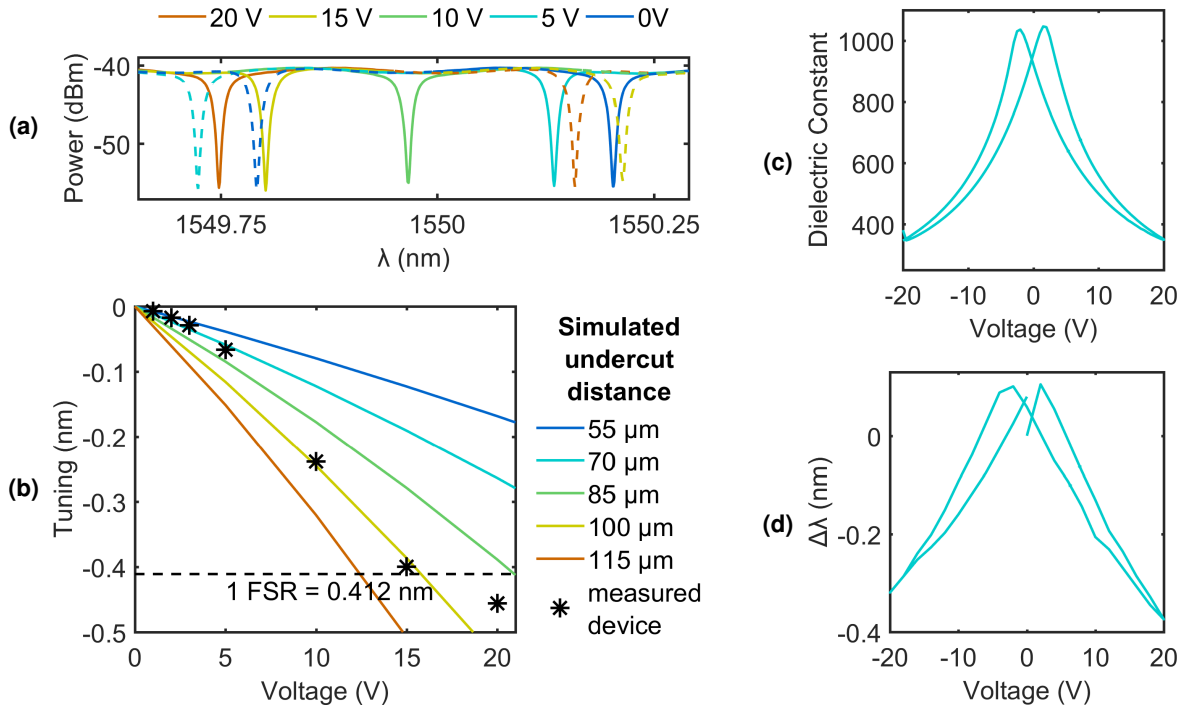

Figure 8.5: **Static tuning across a FSR is demonstrated.** $V_{FSR} = 16\,\mathrm{V}$. (a) Measured TM mode transmission spectra for the same device at various applied voltages. Adjacent notches are dashed to clarify the tuning of a single resonance in solid. (b) Simulated (lines) and measured (data points) tuning of TM mode versus voltage. Nonlinearity in tuning arises due to large mechanical deformation and hysteresis in the PZT. (c) PZT dielectric constant varies with the applied field and displays hysteresis, characteristic of ferroelectrics. Device area is $0.01\,\mathrm{cm}^2$. (d) This hysteresis is observed in the ring resonator tuning as the electric field is reversed. Reproduced from [1].

region. This was the maximum amount of undercut achievable prior to structural failure due to the concentration of compressive stress at sharp features near coupling regions. In the simulated trace of Fig. 8.5(b), we observe that tuning is not perfectly linear. This is due to the rotational component of the deformation shown in Fig. 8.1(c), 8.1(d). The displacement of the cantilevered structure is normal to its surface, and thus as the displacement increases, a larger fraction of the incremental displacement lies in the radial direction. In the real structure however, the nonlinearity is more pronounced. This is due to the ferroelectric nature of PZT, which was not included in the simulation. The characteristic hysteresis of the dielectric constant, measured by the Sawyer-Tower method, is shown in Fig. 8.5(c), and the resultant hysteresis in the device tuning is shown in Fig. 8.5(d).

The leakage current was below 10 nA, limited by equipment sensitivity, for voltages below 5 V. For biases above 5 V to 10 V, we observe a gradually increasing leakage current versus time. Up to 20 V bias, devices remain operational for several minutes during which measurements were taken. At 25 V bias, instantaneous failure was observed. We credit this to abnormally high particulate count due to poor airflow from a PZT sol-gel deposition process optimized for 150 mm wafers rather than 100 mm wafers. This resulted in low dielectric strength and poor yield. For optimized processes, nA leakage currents at long-term sustained bias above 30 V are readily achieved [16, 17, 18].

Following the design of [12] for a high extinction ratio TM mode filter, we expect the high Q to be limited by coupling and coupler losses rather than propagation loss. We measure $Q = 8.6 \times 10^4$ in the TM mode. Lower propagation loss and coupling in the TE mode yield $Q = 1.0 \times 10^6$. Ring resonator round-trip losses (including waveguide losses and coupling losses from add and drop ports) were estimated by fitting ring resonator spectral response to be 0.11 dB to 0.12 dB in the TE mode and 0.25 dB to 0.27 dB in TM mode, corresponding to an upper bound of 0.30 dB cm^{-1} to 0.35 dB cm^{-1} for TE losses,

and 0.65 dB cm^{-1} to 0.75 dB cm^{-1} for TM losses. Absolute measures of waveguide loss are attainable through optical backscatter reflectrometry (OBR) or cutback measurements, however no waveguide spirals of sufficient length for OBR could be measured due to low yield. For an identical released waveguide without any PZT processing, a waveguide loss of 0.12 dB cm^{-1} for the TE mode was measured by OBR, consistent with the results of [12]. We attribute the additional 0.1 dB cm^{-1} to 0.2 dB cm^{-1} loss in the TE mode and 0.5 dB cm^{-1} to 0.6 dB cm^{-1} loss in the TM mode both to coupling losses and extraordinary roughness and deep pitting of the SiO_2 upper cladding surface from C_4F_8/Cl_2 RIE etch used to pattern the PZT actuator. The TM mode is disproportionately impacted due to its lower core confinement and larger mode area, resulting in a larger interaction with the top cladding surface. For the same reason, the TM mode experiences a larger coupling coefficient, as well as larger coupling losses. AFM scan and SEM image of the top surface are shown in Fig. 8.4(e), 8.4(f). The peak-to-peak vertical deviation is greater than 200 nm, while the RMS roughness R_q is 20 nm. An alternative patterning processing using an Argon ion-mill etch to pattern the actuator followed by wet etch removal of an etch stop layer should reduce or eliminate top cladding surface roughness contribution to loss in future fabrication runs.

The small signal frequency domain response of the tuning was characterized by fixing the laser source wavelength to a value 3 dB below maximum transmission, near a resonance notch. A network analyzer supplies electrical input to tune the actuator, and analyzes the resulting electrical output response of the photodetector. The measurements were taken at 0 V DC bias. The device capacitance is 10 nF, the source output impedance is 50 Ω, and there is approximately 4 Ω parasitic resistance. This indicates an RC-limited response beyond 300 kHz. To obtain flat response to higher frequencies, a 10 Ω resistor is placed in parallel with the device to shunt the capacitance, increasing the RC frequency to about 1.3 MHz. The frequency response of the same device as in the

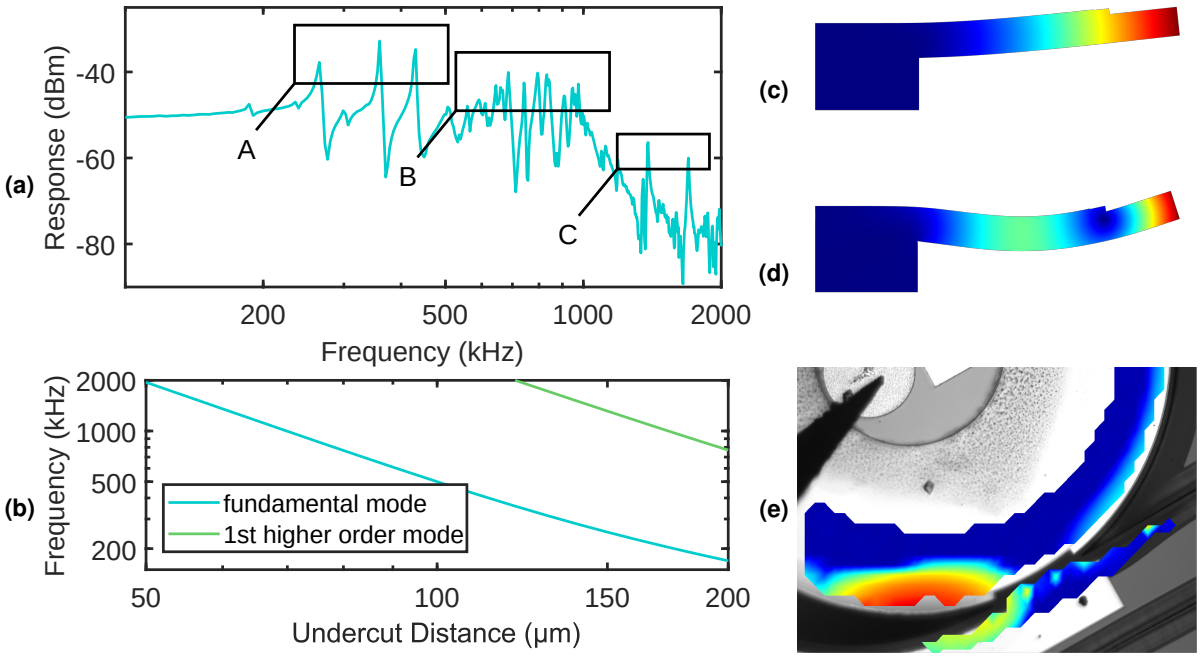

Figure 8.6: **Dynamic device response.** (a) Measured resonator modulation response of the device in Fig. 8.4(d) with regions of interest indicated by A, B, and C. (b) Simulated vibrational eigenmode frequencies versus undercut. Fundamental (c) and first higher order (d) vibrational mode shapes, respectively. Redder colors indicate greater displacement from equilibrium. Simulated eigenfrequencies in (b) provide insight into the real resonances in (a). We ascribe A and C to fundamental and first order resonances of 100 µm to 160 µm undercut areas, respectively. We ascribe B to fundamental vibrations of 80 µm undercut areas. (e) Measurement by laser doppler vibrometry of the lowest frequency resonance. The movement is localized to the region of largest undercut. Reproduced from [1].

heightmap of Fig. 8.4(d) is shown in Fig. 8.6(a). At mechanical resonance, we observe large enhancement of the tuning range. Furthermore, the frequency response exhibits many distinct features, which we ascribe to localized oscillations of the released waveguide membrane with frequency determined by the amount of undercut in the region of oscillation. For example, Fig. 8.6(e) shows the vertical displacement field for the lowest frequency resonance of a ring as measured by laser doppler vibrometry. The movement is localized to just the small region near the directional coupler where the undercut is largest. The relationship between undercut distance and mechanical resonance frequency is given in Fig. 8.6(b), where we model the vibrational eigenfrequencies as a function of undercut distance in a radially symmetric geometry. We ascribe the strong resonance peaks at 265 kHz, 359 kHz, and 430 kHz indicated by A in Fig. 8.6(a) to vibrations in areas adjacent to the coupling regions, where the undercut is 100 µm to 160 µm. For this range of undercut distances, the model predicts fundamental vibrations (with shape as shown in Fig. 8.6(c)) at 200 kHz to 500 kHz. Distinct resonances at 1384 kHz and 1700 kHz correspond to higher order vibrations (in the shape of Fig. 8.6(d)) in the same physical regions. Many competing resonances indicated by B are present in the 600 kHz to 1000 kHz range which we assign to regions away from the directional couplers where the undercut is consistently around 80 µm. In the radial direction, these modes have the shape of the fundamental oscillation depicted in Fig. 8.6(c), but may have a significant wavevector component in the azimuthal direction with slight change in frequency, leading to the presence of many closely spaced resonances. The response falls off rapidly beyond 1 MHz, due to both RC limitations, and roll-off in the mechanical response.

Discussion

V_π denotes the voltage required to induce a π phase shift (rather than 2π for a full FSR). We observe that this condition is met for about 10 V in Fig. 8.6(a) in the TM mode. For the TE mode, whose tuning is within 4 % of the TM mode, we also observe $V_\pi = 10\,\mathrm{V}$. For a 580 µm ring radius and TE waveguide loss of $0.3\,\mathrm{dB\,cm^{-1}}$, we calculate $V_\pi L = 3.6\,\mathrm{V\,cm}$, and $V_\pi L\alpha = 1.1\,\mathrm{V\,dB}$. This value of $V_\pi L$ is larger than values achievable with silicon or III-V phase modulators. However, taking into account optical losses through the $V_\pi L\alpha$ figure of merit, these results demonstrate tuning efficiency at parity with current state-of-the-art phase modulators.

Free carrier plasma dispersion-based modulators in silicon can achieve modulation efficiency below 1 V cm for pn-junction or MOS capacitor devices [24, 25, 26]. However, free carrier absorption limits the propagation loss in these devices to above $10\,\mathrm{dB\,cm^{-1}}$, and $V_\pi L\alpha > 10\,\mathrm{V\,dB}$. Phase modulators based on III-V quantum wells may reach better efficiency, for example the III-V quantum well modulator demonstrated in [27] with $V_\pi L = 0.09\,\mathrm{V\,cm}$, and loss of $20\,\mathrm{dB\,cm^{-1}}$ leads to a figure of merit $V_\pi L\alpha = 1.8\,\mathrm{V\,dB}$. Recently, a III-V/Si MOS capacitor structure has achieved $V_\pi L = 0.09\,\mathrm{V\,cm}$ with $26\,\mathrm{dB\,cm^{-1}}$ loss [28].

Phase tuners using electro-optic polymers have also been demonstrated with extraordinarily low $V_\pi L$ ($< 0.1\,\mathrm{V\,cm}$), at the expense of high waveguide loss ($> 10\,\mathrm{dB\,cm^{-1}}$) [29]. In [30], a $V_\pi L$ of $0.62\,\mathrm{V\,cm}$ with loss of about $10\,\mathrm{dB\,cm^{-1}}$ was demonstrated. In [31], a $V_\pi L = 0.052\,\mathrm{V\,cm}$ was demonstrated, with waveguide loss of $40\,\mathrm{dB\,cm^{-1}}$, for a $V_\pi L\alpha$ of $2.08\,\mathrm{V\,dB}$.

Ferroelectric ceramics with strong electro-optic (Pockels) effect have potential to reduce waveguide losses. By incorporating lithium niobate thin films on silicon, $V_\pi L = 3.8\,\mathrm{V\,cm}$ and $\alpha = 1.2\,\mathrm{dB\,cm^{-1}}$ have been achieved [32], yielding $V_\pi L\alpha = 4.6\,\mathrm{V\,dB}$. In

[33], a thin-film epitaxially grown $BaTiO_3$ modulator on MgO substrate was reported with $V_\pi L = 1.25\,\mathrm{V\,cm}$, and less than $1\,\mathrm{dB\,cm^{-1}}$ loss, for $V_\pi L\alpha = 1.25\,\mathrm{V\,dB}$. More recent work on epitaxially grown $BaTiO_3$ on silicon shows good modulation efficiency ($1.5\,\mathrm{V\,cm}$) but poor propagation loss ($44\,\mathrm{dB\,cm^{-1}}$) [34]. PLZT on sapphire [35] has demonstrated $V_\pi L = 3\,\mathrm{V\,cm}$, and $\alpha = 2.7\,\mathrm{dB\,cm^{-1}}$ for a $V_\pi L\alpha = 8.1\,\mathrm{V\,dB}$. Recent progress using PZT with lanthanide-based seed layer on a silicon substrate show impressive performance ($V_\pi L = 1\,\mathrm{V\,cm}$, $V_\pi L\alpha = 1\,\mathrm{V\,dB}$) however losses ($\alpha \approx 1\,\mathrm{dB\,cm^{-1}}$) remain too high to qualify as ultra-low loss [36].

An interesting approach is the stress-induced Pockels effect in silicon waveguides [37], which could enable low-propagation-loss electro-optic phase tuning. The effect is extremely weak however; to date $V_\pi L = 89\,\mathrm{V\,cm}$ has been reported [38]. AlN is another interesting material platform for integrated photonics as it exhibits both piezoelectricity and Pockels electro-optic effect. In [39], low waveguide propagation loss of $0.6\,\mathrm{dB\,cm^{-1}}$ is reported, however the tuning efficiency is also low, tuning just 15 pm across 30 V applied bias. More recently [40], a tuning efficiency of $V_\pi L = 240\,\mathrm{V\,cm}$ has been reported.

Thermal phase shifters may be tuned by a full FSR down to extremely small device sizes and low voltage, however in this case, it is the power requirement that is prohibitive. In ultra-low-loss Si_3N_4, 200 mW to 500 mW are required per device [4]. In Si, 10 mW to 100 mW of power per device are typical, and 2.3 mW per FSR has been demonstrated with undercut waveguides at the expense of tuning speed (170 µs) [3]. For applications requiring thousands of devices, even single mW of DC power per phase shifter becomes significant, and thermal crosstalk complicates system operation.

Prior to this work, optical MEMS based approaches have been explored by various authors. For example, in [41, 42, 43], ring resonators are tuned by electrostatic actuation of freestanding structures in the evanescent field of the waveguide. MEMS-actuated air-gap directional couplers have been explored to create more dramatically reconfigurable

optical systems [44], including a 50×50 crossbar switch [45]. Notably, in [46], a tunable ring cavity is formed by two fully suspended silicon waveguide sections linked by air-gap directional couplers. By lateral displacement of the waveguide sections relative to one another, an impressive tuning range of 10 nm is achieved. However, techniques such as those described above require complex structures within the mode of the waveguide that tend to increase scattering losses, and their applicability to low-loss waveguide platforms has yet to be demonstrated. In a similar vein, MEMS movable mirror approaches [47, 48, 49, 50] have also been demonstrated, however these approaches require free propagation regions through air that add reflections and pose a challenge for integration into planar light-wave circuits.

Dynamic actuation of the stress field in a waveguide by PZT has also been explored [51, 52, 53, 5, 6], with the potential for lower optical losses than the air-gap-based MEMS approaches described above. Photoelastic modulation in a silicon-nitride-based low-loss platform has been demonstrated [6]. While the effect is weak ($V_\pi L = 50\,\mathrm{V\,cm}$), the waveguide loss is low ($\approx 0.1\,\mathrm{dB\,cm^{-1}}$), leading to a reasonable performance $V_\pi L\alpha = 5\,\mathrm{V\,dB}$. Recently, in [54], an AlN piezoelectric actuator was deposited on a suspended silicon nitride waveguide to form a unimorph cantilever, in a geometry that bears similarity to this work. However, due to an unoptimized geometry and low piezoelectric constants of AlN relative to PZT, the tuning range is just 20 pm under 60 V bias. Though a radial displacement of 1 nm is claimed, the tuning exhibits large polarization dependence, indicating that tuning may be largely due to photoelastic index modulation, rather than modulation of the physical length of the resonator. Thus, even among optical MEMS based approaches, phase tuning is largely performed by perturbing the waveguide effective index. Those works that explore perturbing the cavity size have done so by employing air-gaps, either in the form of free propagation regions [47, 48, 49, 50] or suspended directional couplers [46]. To the best of the authors' knowledge, the in-plane component of

macroscopic deformation in monolithic waveguides has been largely ignored until now.

Despite fabrication challenges which significantly degraded waveguide loss and limited the applied voltage, the figure of merit $V_\pi L\alpha = 1.1\,\mathrm{V\,dB}$ demonstrated in this work is already at parity with the best reported numbers across all technologies. However, in contrast to all approaches considered thus far (apart from thermal tuning), the tuning efficiency, $V_\pi L$, improves as the effective device size is reduced. Performance in the current demonstration was constrained by the intrinsic compressive stress of about $-260\,\mathrm{MPa}$ to $-320\,\mathrm{MPa}$ in thermally grown and deposited SiO_2 layers, leading to mechanical failure for large undercut. This is especially severe in the coupling regions, where asymmetry and sharp corners lead to high concentrations of stress. To bypass this limitation and take advantage of the favorable scaling of the effect with reduced size, we present the two optimized designs shown in Fig. 8.2(a), 8.2(b), discussed earlier. Notably, in the dual-stripe Si_3N_4 based design, the combination of dual silicon nitride ($> 800\,\mathrm{MPa}$ tensile stress) layers within an oxide cladding of comparable thickness serve to balance the overall stress in the structure. For the silicon-on-insulator based design, the silicon itself is stress-free.

With regards to excess waveguide loss caused by the PZT fabrication and release processes, we note that no excess loss was observed in structures without PZT processing, as mentioned earlier. Furthermore, released structures have been demonstrated with quality factors up to 875 million for freestanding resonators, and 200 million with integrated bus waveguides [55, 56]. While XeF_2 gas used for release is known to slowly attack SiO_2 in the presence of Si [57], there is no evidence of roughening of the SiO_2 surface. Thus, if the top-surface SiO_2 can be protected from PZT processing by the method proposed earlier, this phase tuning technique may be applied with zero excess waveguide loss.

The propagation loss for dual stripe Si_3N_4 waveguides was reported in [11] to be $0.08\,\mathrm{dB\,cm^{-1}}$ to $0.09\,\mathrm{dB\,cm^{-1}}$. In the modified design presented here, the core confine-

ment is within a 10 % of the core confinement of the original design. Thus, we expect that scattering loss at the core-cladding interface should be roughly identical in both configurations. For a hypothetical dual stripe design with 0.09 dB cm^{-1} loss, 80 µm bend radius, and tunable by a FSR with 30 V applied bias, or a half-wave voltage of about 20 V, we estimate $V_\pi L = 1\,\mathrm{V\,cm}$ and $V_\pi L\alpha = 0.09\,\mathrm{V\,dB}$. For the silicon-based design with ring radius 45 µm, we estimate a $V_\pi L = 0.57\,\mathrm{V\,cm}$. A conservative estimate of 1 dB cm^{-1} for deeply etched Si waveguides would yield $V_\pi L\alpha = 0.57\,\mathrm{V\,dB}$, however, shallow etched silicon waveguides with sub 1 dB cm^{-1} loss have been demonstrated [58, 59, 60], which could potentially push performance into $V_\pi L\alpha < 0.1\,\mathrm{V\,dB}$ range. Similarly, recently improvements in high-confinement silicon nitride waveguides [61] have yielded $\alpha < 0.01\,\mathrm{dB\,cm^{-1}}$ waveguide loss at similar bend radii. Applying this approach to such low-loss waveguides would allow a further order-of-magnitude improvement in $V_\pi L\alpha$.

Conclusion

We have presented a novel phase tuning approach by geometric deformation with ultra-low power operation and tunability that scales favorably with reduced device size. In a proof-of-concept demonstration, we have already demonstrated performance at parity with state-of-the-art published results, with a clear path towards a further improvement by an order of magnitude. We expect this work to primarily be of interest to the ultra-low-loss community, and especially for the RF photonics community where low propagation loss is critical, and bend radii of 100 µm and above are typical. If our proposed design down to 45 µm bend radius may be experimentally realized, this would enable thousands of devices to be integrated on a single 20 mm by 20 mm die, with applications such as wavelength-selective crossbar switches, and optical phased arrays for LIDAR.

Bibliography

[1] W. Jin, R. G. Polcawich, P. A. Morton, and J. E. Bowers, *Piezoelectrically tuned silicon nitride ring resonator*, *Optics Express* **26** (2018), no. 3 3174–3187.

[2] G. Li, X. Zheng, J. Yao, H. Thacker, I. Shubin, Y. Luo, K. Raj, J. E. Cunningham, and A. V. Krishnamoorthy, *25Gb/s 1V-driving CMOS ring modulator with integrated thermal tuning*, *Opt. Express* **19** (2011), no. 21 20435–20443.

[3] P. Dong, W. Qian, H. Liang, R. Shafiiha, D. Feng, G. Li, J. E. Cunningham, A. V. Krishnamoorthy, and M. Asghari, *Thermally tunable silicon racetrack resonators with ultralow tuning power*, *Opt. Express* **18** (2010), no. 19 20298–20304.

[4] C. G. Roeloffzen, L. Zhuang, C. Taddei, A. Leinse, R. G. Heideman, P. W. van Dijk, R. M. Oldenbeuving, D. A. Marpaung, M. Burla, and K.-J. Boller, *Silicon nitride microwave photonic circuits*, *Opt. Express* **21** (2013), no. 19 22937–22961.

[5] N. Hosseini, R. Dekker, M. Hoekman, M. Dekkers, J. Bos, A. Leinse, and R. Heideman, *Stress-optic modulator in TriPleX platform using a piezoelectric lead zirconate titanate (PZT) thin film*, *Opt. Express* **23** (2015), no. 11 14018–14026.

[6] J. P. Epping, D. Marchenko, A. Leinse, R. Mateman, M. Hoekman, L. Wevers, E. J. Klein, C. G. Roeloffzen, M. Dekkers, and R. G. Heideman, *Ultra-low-power stress-optics modulator for microwave photonics*, in *SPIE OPTO*, pp. 101060F–101060F, International Society for Optics and Photonics, 2017.

[7] L. Zhuang, C. Roeloffzen, R. Heideman, A. Borreman, A. Meijerink, and W. van Etten, *Single-chip ring resonator-based 1×8 optical beam forming network in CMOS-compatible waveguide technology*, *IEEE Photon. Technol. Lett.* **19** (2007), no. 15 1130–1132.

[8] P. A. Morton, J. B. Khurgin, Z. Mizrahi, and S. J. Morton, *Commercially packaged optical true-time-delay devices with record delays of wide bandwidth signals*, in *Conference on Lasers and Electro-Optics*, pp. 1–2, IEEE, 2014.

[9] B. A. Auld, *Acoustic Fields and Waves in Solids*. Wiley, 1973.

[10] D. A. Berlincourt, D. R. Curran, and H. Jaffe, *Piezoelectric and piezomagnetic materials and their function in transducers*, in *Physical Acoustics: Principles and Methods*, vol. 1A, p. 247. Academic Press, New York, 1964.

[11] L. Zhuang, D. Marpaung, M. Burla, W. Beeker, A. Leinse, and C. Roeloffzen, *Low-loss, high-index-contrast Si_3N_4/SiO_2 optical waveguides for optical delay lines in microwave photonics signal processing*, *Opt. Express* **19** (2011), no. 23 23162–23170.

[12] T. Huffman, D. Baney, and D. J. Blumenthal, *High extinction ratio widely tunable low-loss integrated Si_3N_4 third-order filter*, *arXiv preprint arXiv:1708.06344* (2017).

[13] S. Trolier-McKinstry and P. Muralt, *Thin film piezoelectrics for MEMS*, *J. Electroceram.* **12** (2004), no. 1 7–17.

[14] R. Dixon, *Photoelastic properties of selected materials and their relevance for applications to acoustic light modulators and scanners*, *J. Appl. Phys.* **38** (1967), no. 13 5149–5153.

[15] W. Cook, D. Nelson, and K. Vedam, *Piezooptic and Electrooptic Constants*, vol. 30. Springer, 1996.

[16] B. Melnick, C. P. de Araujo, L. McMillan, D. Carver, and J. Scott, *Recent results on switching, fatigue and electrical characterization of sol-gel based PZT capacitors*, *Ferroelectrics* **116** (1991), no. 1 79–93.

[17] H. D. Chen, K. Udayakumar, K. K. Li, C. J. Gaskey, and L. E. Cross, *Dielectric breakdown strength in sol-gel derived PZT thick films*, *Intgr. Ferroelectr.* **15** (1997), no. 1-4 89–98.

[18] R. Moazzami, C. Hu, and W. H. Shepherd, *Electrical characteristics of ferroelectric PZT thin films for DRAM applications*, *IEEE Trans. Electron Devices* **39** (1992), no. 9 2044–2049.

[19] T. Chen, H. Lee, and K. J. Vahala, *Thermal stress in silica-on-silicon disk resonators*, *Appl. Phys. Lett.* **102** (2013), no. 3 031113.

[20] L. M. Sanchez, D. M. Potrepka, G. R. Fox, I. Takeuchi, K. Wang, L. A. Bendersky, and R. G. Polcawich, *Optimization of $PbTiO_3$ seed layers and Pt metallization for PZT-based piezoMEMS actuators*, *J. Mater. Res.* **28** (2013), no. 14 1920–1931.

[21] G. R. Fox, D. M. Potrepka, and R. G. Polcawich, *Dependence of $\{111\}$-textured Pt electrode properties on TiO_2 seed layers formed by thermal oxidation*, *J. Mater. Sci. Mater. Electron.* (2017) 1–15.

[22] K. Budd, S. Dey, and D. Payne, *Sol-gel processing of $PbTiO_3$, $PbZrO_3$, PZT, and PLZT thin films.*, in *British Ceramic Proceedings* (B. Steele, ed.), pp. 107–121, Inst of Ceramics, 1985.

[23] S. K. Dey, K. D. Budd, and D. A. Payne, *Thin-film ferroelectrics of PZT of sol-gel processing*, *IEEE Transactions on Ultrasonics, Ferroelectrics, and Frequency Control* **35** (Jan, 1988) 80–81.

[24] S. S. Azadeh, F. Merget, S. Romero-García, A. Moscoso-Mártir, N. von den Driesch, J. Müller, S. Mantl, D. Buca, and J. Witzens, *Low V_π silicon photonics*

modulators with highly linear epitaxially grown phase shifters, *Opt. Express* **23** (2015), no. 18 23526–23550.

[25] G. T. Reed, G. Z. Mashanovich, F. Y. Gardes, M. Nedeljkovic, Y. Hu, D. J. Thomson, K. Li, P. R. Wilson, S.-W. Chen, and S. S. Hsu, *Recent breakthroughs in carrier depletion based silicon optical modulators*, *Nanophotonics* **3** (2014), no. 4-5 229–245.

[26] M. A. Webster, K. Lakshmikumar, C. Appel, C. Muzio, B. Dama, and K. Shastri, *Low-power MOS-capacitor based silicon photonic modulators and CMOS drivers*, in *Optical Fiber Communication Conference*, pp. W4H–3, Optical Society of America, 2015.

[27] L. Zhang, J. Sinsky, D. Van Thourhout, N. Sauer, L. Stulz, A. Adamiecki, and S. Chandrasekhar, *Low-voltage high-speed travelling wave InGaAsP-InP phase modulator*, *IEEE Photon. Technol. Lett.* **16** (2004), no. 8 1831–1833.

[28] T. Hiraki, T. Aihara, K. Hasebe, K. Takeda, T. Fujii, T. Kakitsuka, T. Tsuchizawa, H. Fukuda, and S. Matsuo, *Heterogeneously integrated III–V/Si MOS capacitor Mach–Zehnder modulator*, *Nat. Photon.* **11** (2017), no. 8 482–485.

[29] J. Liu, G. Xu, F. Liu, I. Kityk, X. Liu, and Z. Zhen, *Recent advances in polymer electro-optic modulators*, *RSC Adv.* **5** (2015), no. 21 15784–15794.

[30] R. Ding, T. Baehr-Jones, W.-J. Kim, A. Spott, M. Fournier, J.-M. Fedeli, S. Huang, J. Luo, A. K.-Y. Jen, L. Dalton, and M. Hochberg, *Sub-volt silicon-organic electro-optic modulator with 500 MHz bandwidth*, *J. Lightw. Technol.* **29** (2011), no. 8 1112–1117.

[31] R. Palmer, S. Koeber, D. L. Elder, M. Woessner, W. Heni, D. Korn,

M. Lauermann, W. Bogaerts, L. Dalton, W. Freude, J. Leuthold, and C. Koos, *High-speed, low drive-voltage silicon-organic hybrid modulator based on a binary-chromophore electro-optic material*, *J. Lightw. Technol.* **32** (2014), no. 16 2726–2734.

[32] A. Rao, A. Patil, J. Chiles, M. Malinowski, S. Novak, K. Richardson, P. Rabiei, and S. Fathpour, *Heterogeneous microring and Mach-Zehnder modulators based on lithium niobate and chalcogenide glasses on silicon*, *Opt. Express* **23** (2015), no. 17 22746–22752.

[33] P. Tang, D. Towner, T. Hamano, A. Meier, and B. Wessels, *Electrooptic modulation up to 40 GHz in a barium titanate thin film waveguide modulator*, *Opt. Express* **12** (2004), no. 24 5962–5967.

[34] C. Xiong, W. H. Pernice, J. H. Ngai, J. W. Reiner, D. Kumah, F. J. Walker, C. H. Ahn, and H. X. Tang, *Active silicon integrated nanophotonics: ferroelectric $BaTiO_3$ devices*, *Nano Lett.* **14** (2014), no. 3 1419–1425.

[35] G. Jin, Y. Zou, V. Fuflyigin, S. Liu, Y. Lu, J. Zhao, and M. Cronin-Golomb, *PLZT film waveguide Mach-Zehnder electrooptic modulator*, *J. Lightw. Technol.* **18** (2000), no. 6 807.

[36] K. Alexander, J. P. George, B. Kuyken, J. Beeckman, and D. Van Thourhout, *Broadband electro-optic modulation using low-loss PZT-on-silicon nitride integrated waveguides*, in *CLEO: Applications and Technology*, pp. JTh5C–7, Optical Society of America, 2017.

[37] R. S. Jacobsen, K. N. Andersen, P. I. Borel, J. Fage-Pedersen, L. H. Frandsen, O. Hansen, M. Kristensen, A. V. Lavrinenko, G. Moulin, H. Ou, C. Peucheret,

B. Zsgiri, and A. Bjarklev, *Strained silicon as a new electro-optic material*, *Nature* **441** (2006), no. 7090 199–202.

[38] B. Chmielak, C. Matheisen, C. Ripperda, J. Bolten, T. Wahlbrink, M. Waldow, and H. Kurz, *Investigation of local strain distribution and linear electro-optic effect in strained silicon waveguides*, *Opt. Express* **21** (2013), no. 21 25324–25332.

[39] C. Xiong, W. H. Pernice, X. Sun, C. Schuck, K. Y. Fong, and H. X. Tang, *Aluminum nitride as a new material for chip-scale optomechanics and nonlinear optics*, *New J. Phys.* **14** (2012), no. 9 095014.

[40] S. Zhu and G.-Q. Lo, *Aluminum nitride electro-optic phase shifter for backend integration on silicon*, *Opt. Express* **24** (2016), no. 12 12501–12506.

[41] G. N. Nielson, D. Seneviratne, F. Lopez-Royo, P. T. Rakich, Y. Avrahami, M. R. Watts, H. A. Haus, H. L. Tuller, and G. Barbastathis, *Integrated wavelength-selective optical MEMS switching using ring resonator filters*, *IEEE Photon. Technol. Lett.* **17** (2005), no. 6 1190–1192.

[42] S. C. Abdulla, L. Kauppinen, M. Dijkstra, M. J. de Boer, E. Berenschot, H. V. Jansen, R. De Ridder, and G. J. Krijnen, *Tuning a racetrack ring resonator by an integrated dielectric MEMS cantilever*, *Optics express* **19** (2011), no. 17 15864–15878.

[43] C. Errando-Herranz, F. Niklaus, G. Stemme, and K. B. Gylfason, *A low-power MEMS tunable photonic ring resonator for reconfigurable optical networks*, in *28th IEEE International Conference on Micro Electro Mechanical Systems*, pp. 53–56, IEEE, 2015.

[44] H. Du, F. S. Chau, and G. Zhou, *Mechanically-tunable photonic devices with on-chip integrated MEMS/NEMS actuators*, *Micromachines* **7** (2016), no. 4 69.

[45] S. Han, T. J. Seok, N. Quack, B.-W. Yoo, and M. C. Wu, *Large-scale silicon photonic switches with movable directional couplers*, *Optica* **2** (2015), no. 4 370–375.

[46] T. Ikeda and K. Hane, *A microelectromechanically tunable microring resonator composed of freestanding silicon photonic waveguide couplers*, *Applied Physics Letters* **102** (2013), no. 22 221113.

[47] M. C. Huang, Y. Zhou, and C. J. Chang-Hasnain, *A nanoelectromechanical tunable laser*, *Nat. Photon.* **2** (2008), no. 3 180–184.

[48] V. Jayaraman, G. Cole, M. Robertson, C. Burgner, D. John, A. Uddin, and A. Cable, *Rapidly swept, ultra-widely-tunable 1060 nm MEMS-VCSELs*, *Electron. Lett.* **48** (2012), no. 21 1331–1333.

[49] X. Zheng, V. Kaman, S. Yuan, Y. Xu, O. Jerphagnon, A. Keating, R. C. Anderson, H. N. Poulsen, B. Liu, J. R. Sechrist, C. Pusarla, R. Helkey, D. J. Blumenthal, and J. E. Bowers, *Three-dimensional MEMS photonic cross-connect switch design and performance*, *IEEE J. Sel. Topics Quantum Electron.* **9** (2003), no. 2 571–578.

[50] M. Datta, M. Pruessner, K. Amarnath, J. McGee, S. Kanakaraju, and R. Ghodssi, *Wavelength-selective integrated optical MEMS filter in InP*, in *18th IEEE International Conference on Micro Electro Mechanical Systems*, pp. 88–91, IEEE, 2005.

[51] K. Tsia, S. Fathpour, and B. Jalali, *Electrical tuning of birefringence in silicon waveguides*, *Appl. Phys. Lett.* **92** (2008), no. 6 061109.

[52] Y. Sebbag, I. Goykhman, B. Desiatov, T. Nachmias, O. Yoshaei, M. Kabla, S. Meltzer, and U. Levy, *Bistability in silicon microring resonator based on strain induced by a piezoelectric lead zirconate titanate thin film*, *Appl. Phys. Lett.* **100** (2012), no. 14 141107.

[53] S. Donati, L. Barbieri, and G. Martini, *Piezoelectric actuation of silica-on-silicon waveguide devices*, *IEEE Photon. Technol. Lett.* **10** (1998), no. 10 1428–1430.

[54] B. Dong, H. Tian, M. Zervas, T. J. Kippenberg, and S. A. Bhave, *Port: a piezoelectric optical resonance tuner*, in *31st IEEE International Conference on Micro Electro Mechanical Systems*, IEEE, 2018.

[55] H. Lee, T. Chen, J. Li, K. Y. Yang, S. Jeon, O. Painter, and K. J. Vahala, *Chemically etched ultrahigh-Q wedge-resonator on a silicon chip*, *Nat. Photon.* **6** (2012), no. 6 369–373.

[56] K. Y. Yang, D. Y. Oh, S. H. Lee, Q.-F. Yang, X. Yi, and K. Vahala, *Integrated ultra-high-Q optical resonator*, *arXiv preprint arXiv:1702.05076* (2017).

[57] J.-F. Veyan, M. Halls, S. Rangan, D. Aureau, X.-M. Yan, and Y. Chabal, *XeF_2-induced removal of SiO_2 near Si surfaces at 300 K: An unexpected proximity effect.*, *J. Appl. Phys.* **108** (2010), no. 11 114914.

[58] P. Dong, W. Qian, S. Liao, H. Liang, C.-C. Kung, N.-N. Feng, R. Shafiiha, J. Fong, D. Feng, A. V. Krishnamoorthy, and M. Asghari, *Low loss shallow-ridge silicon waveguides*, *Opt. Express* **18** (2010), no. 14 14474–14479.

[59] G. Li, J. Yao, H. Thacker, A. Mekis, X. Zheng, I. Shubin, Y. Luo, J.-H. Lee, K. Raj, J. E. Cunningham, and A. V. Krishnamoorthy, *Ultralow-loss, high-density*

SOI optical waveguide routing for macrochip interconnects, *Opt. Express* **20** (2012), no. 11 12035–12039.

[60] S. K. Selvaraja, G. Winroth, S. Locorotondo, G. Murdoch, A. Milenin, C. Delvaux, P. Ong, S. Pathak, W. Xie, G. Sterckx, G. Lepage, D. V. Thourhout, W. Bogaerts, J. V. Campenhout, and P. Absil, *193nm immersion lithography for high performance silicon photonic circuits*, in *Proc. of SPIE Vol*, vol. 9052, pp. 90520F–1, 2014.

[61] X. Ji, F. A. Barbosa, S. P. Roberts, A. Dutt, J. Cardenas, Y. Okawachi, A. Bryant, A. L. Gaeta, and M. Lipson, *Ultra-low-loss on-chip resonators with sub-milliwatt parametric oscillation threshold*, *Optica* **4** (2017), no. 6 619–624.

Chapter 9

Summary and outlook

After decades of development, integrated photonics has become a practical technology with applications in communications, sensing, and computation. Using the benefits of scalable, low cost manufacturing inherited from electronic integration, integrated photonics has provided low-cost, compact, and efficient solutions to problems for which bulk-optic-based or fiber-optic-based systems would be infeasible. Contrary to integrated electronic circuits, however, the transition from bulk optics and fiber optics to integrated photonics often requires a sacrifice in performance, as integrated waveguides often exhibit significantly higher propagation loss.

In this thesis, significant improvements to propagation loss in an ultra-low-loss silicon nitride waveguide platform were realized through the transition from a university, research-oriented clean-room to a commercial, CMOS foundry. As a result, propagation loss in integrated waveguides as low as 0.1 dB/m were observed, leading to the demonstration of resonators with Q factors as high as 260 M, and record high finesse among integrated devices. The relatively compact, mm-scale footprint of these devices enabled corresponding innovations in device design, such that meter-scale waveguides could form coiled resonators occupying less than 1 cm^2 area, novel resonator structures with im-

proved modal selectivity could be engineered to enable a single-mode Raman laser, and anywhere from tens to hundreds of devices could occupy a single reticle. Furthermore, novel stitching structures were designed to enable large-scale optical systems to scale beyond the single-reticle limit, with excess loss of just 0.0004 dB/stitch.

These novel capabilities enabled the demonstration of ultra-low-noise integrated lasers with frequency-noise performance exceeding that of a commercial, high-performance fiber laser. Furthermore, the performance of the platform was also shown to be sufficient to enable ready access to various nonlinear phenomena, with demonstrations of Brillouin gain, a Raman laser, and an integrated, ultra-low noise, Kerr-effect frequency comb with turn-key operation.

In this thesis, a pathway to more complete, heterogeneous integration was also proposed, in which direct wafer bonding or deposition of disparate materials could endow ultra-low loss silicon nitride waveguides with additional capabilities. A low-temperature, hydrogen-free, deposited silicon dioxide film was developed to enable back-end heterogeneous-integration of III-V gain materials while retaining low waveguide loss. An approach to introducing piezoelectric material on suspended silicon nitride waveguides was also presented, by which ultra-low-loss integrated photonic circuits could be reconfigured without the energy inefficiency of thermal tuning. These approaches could eventually lead to complete optical systems, including low-loss resonant cavities, efficient tuning, modulators, photodetectors, and gain material, on a single substrate.

Building on these results, numerous directions for future research are potentially fruitful. With regard to fabrication process improvements, a thorough understanding of the precise sources of scattering loss, whether originating from the sidewall in the silicon nitride etch process, the top surface in the silicon nitride deposition process, or the bulk materials themselves, may lead to further reduction in propagation loss. Process improvements in the heterogeneous integration process presented in Chapter 7 could en-

able extremely low frequency noise performance on a single chip. Further development incorporating piezoelectric or electro-optic materials while retaining ultra-low loss could enable efficient, large-scale, reconfigurable photonic systems with high performance. Innovations in device design could also enable novel capabilities within this platform. For example, use of gratings [1], higher-order modes [2], and multiple resonators [3, 4, 5, 6] has already been explored by other authors to engineer nonlinear phenomena, as discussed in Chapter 5. Finally, demonstrations of this ultra-low-loss integrated photonic platform to real-world applications are also of interest. Coherent communications [7, 8], LIDAR [9], and optical-atomic-clocks [10] for precision metrology are applications for which the low-noise integrated lasers and frequency combs demonstrated herein are already applicable, improving the noise, cost, and portability of such systems.

Bibliography

[1] S.-P. Yu, D. C. Cole, H. Jung, G. T. Moille, K. Srinivasan, and S. B. Papp, *Spontaneous pulse formation in edgeless photonic crystal resonators*, *Nature Photonics* **15** (2021), no. 6 461–467.

[2] H. Wang, Y.-K. Lu, L. Wu, D. Y. Oh, B. Shen, S. H. Lee, and K. Vahala, *Dirac solitons in optical microresonators*, *Light: Science & Applications* **9** (2020), no. 1 1–15.

[3] Y. Hu, M. Yu, B. Buscaino, N. Sinclair, D. Zhu, R. Cheng, A. Shams-Ansari, L. Shao, M. Zhang, J. M. Kahn, *et. al.*, *High-efficiency and broadband electro-optic frequency combs enabled by coupled micro-resonators*, *arXiv preprint arXiv:2111.14743* (2021).

[4] A. Tikan, J. Riemensberger, K. Komagata, S. Hönl, M. Churaev, C. Skehan,

H. Guo, R. N. Wang, J. Liu, P. Seidler, *et. al.*, *Emergent nonlinear phenomena in a driven dissipative photonic dimer*, *Nature Physics* **17** (2021), no. 5 604–610.

[5] K. Komagata, A. Tikan, A. Tusnin, J. Riemensberger, M. Churaev, H. Guo, and T. J. Kippenberg, *Dissipative kerr solitons in a photonic dimer on both sides of exceptional point*, *arXiv preprint arXiv:2101.09237* (2021).

[6] S. Mittal, G. Moille, K. Srinivasan, Y. K. Chembo, and M. Hafezi, *Topological frequency combs and nested temporal solitons*, *arXiv preprint arXiv:2101.02229* (2021).

[7] B. Corcoran, M. Tan, X. Xu, A. Boes, J. Wu, T. G. Nguyen, S. T. Chu, B. E. Little, R. Morandotti, A. Mitchell, *et. al.*, *Ultra-dense optical data transmission over standard fibre with a single chip source*, *Nat. Commun.* **11** (2020), no. 1 1–7.

[8] A. Fülöp, M. Mazur, A. Lorences-Riesgo, Ó. B. Helgason, P.-H. Wang, Y. Xuan, D. E. Leaird, M. Qi, P. A. Andrekson, A. M. Weiner, *et. al.*, *High-order coherent communications using mode-locked dark-pulse Kerr combs from microresonators*, *Nat. Commun.* **9** (2018), no. 1 1–8.

[9] J. Liu, H. Tian, E. Lucas, A. S. Raja, G. Lihachev, R. N. Wang, J. He, T. Liu, M. H. Anderson, W. Weng, *et. al.*, *Monolithic piezoelectric control of soliton microcombs*, *Nature* **583** (2020), no. 7816 385–390.

[10] Z. L. Newman, V. Maurice, T. Drake, J. R. Stone, T. C. Briles, D. T. Spencer, C. Fredrick, Q. Li, D. Westly, B. R. Ilic, *et. al.*, *Architecture for the photonic integration of an optical atomic clock*, *Optica* **6** (2019), no. 5 680–685.

Appendix A

Silicon-on-insulator photonic integration

This chapter discusses the extension of the results achieved in silicon nitride waveguides to silicon-on-insulator waveguides. In particular, the further improvement of propagation loss in silicon-on-insulator waveguides is discussed with respect to improving the performance of narrow-linewidth lasers, similar to Chapter 4. If a similar level of loss could eventually be achieved, a more straightforward demonstration of Hertz-linewidth lasers on a single chip could be achieved by heterogeneous integration with silicon alone, obviating the need for ultra-low loss silicon nitride. Additionally, the PZT-on-silicon platform proposed in Chapter 8 is extended to the fabrication of an acousto-optic modulator based on a guided acoustic slab modes, known as flexure waves.

A.1 Ultra-low-loss silicon-on-insulator waveguides

Recent optimizations in silicon-on-insulator waveguide geometry have enabled heterogeneously integrated lasers to be directly coupled to high-Q factor resonators on the same

chip [1, 2, 3]. This section presents the result of process development to further reduce propagation loss in ultra-low loss silicon waveguides. The primary differences between this fabrication process and previous efforts on the same platform [1] involve photoresist reflow, and a combination of dry and wet etch patterning of a SiO_2 hardmask, prior to silicon etching.

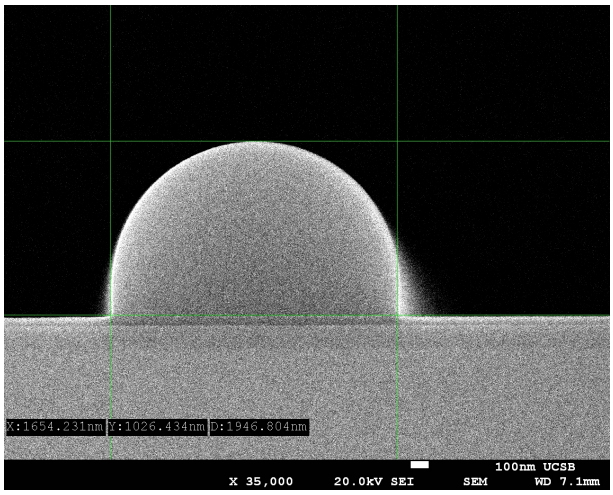

Figure A.1: **Reflowed photoresist profile.** Scanning electron microscope image of a reflowed photoresist profile.

The fabrication process begins with a 100 mm diameter silicon-on-insulator wafer featuring 500 nm thick silicon device layer and 1000 nm buried oxide, which is compatible with heterogeneous III-V/Si integration [3]. A 180 nm silicon dioxide hardmask is deposited on the surface by plasma-enhanced chemical vapor deposition at 300 °C. To pattern the hardmask, a backside anti-reflection coating (Brewer Science DUV42P) a 0.8 µm thickness postive DUV photoresist layer (Rohm and Haas UV6) are applied to the surface, and patterned by 248 nm DUV stepper lithography. Following photoresist patterning, a thermal reflow is applied by baking the sample at 155 °C for 3 minutes using a hotplate with backside vacuum. An example of a reflowed photoresist cross-section is shown in Figure A.1. The reflow of the photoresist, which is driven by surface tension, results in differing cross-sectional profiles for different pattern size, such that wider

structures (pattern width much larger than photoresist thickness) may end up with a less vertical sidewall, and a narrower pattern than the original mask dimension, while narrow structures (pattern width less than photoresist thickness) may feature outward bulge of the photoresist sidewall, and wider pattern than the original mask dimension.

The backside anti-reflection coating is etched by O_2 plasma using reactive-ion etching (RIE), and the hardmask is subsequently dry-etched using a $CHF_3/O_2/CF_4$ gas chemistry using an inductively-coupled plasma reactive ion etch (ICP-RIE). The hardmask is dry-etched to a depth of approximately 155 nm, at which point the photoresist mask is stripped using a combination of solvents, O_2 plasma, and piranha solution (H_2SO_4, H_2O_2 and H_2O. The remaining 25 nm of hardmask is subsequently removed by wet etching in a buffered HF solution (Transene Buffer-HF-Improved), at 1:99 dilution, to complete the hardmask patterning process.

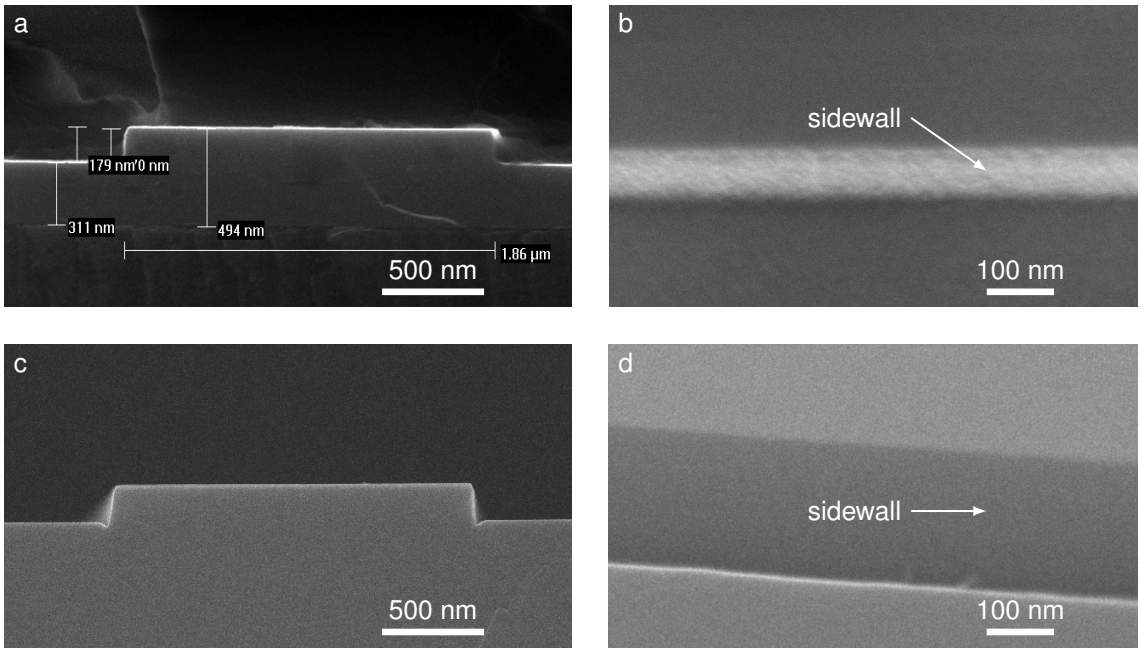

Figure A.2: **Images of etch profile for two silicon etches.** (a) Scanning electrom microscope (SEM) cross-section of $C_4F_8/SF_6/CF_4$-based etch. (b) Oblique view of $C_4F_8/SF_6/CF_4$ etched sidewall, viewed from an angle approximately 30° from surface normal. (c) SEM cross-section of Cl_2-based etch. (d) Oblique view of Cl_2 etched sidewall, viewered from an approximately 60° angle from surface normal.

In the experiment, a silicon ICP-RIE etch chemistry featuring $C_4F_8/SF_6/CF_4$ chemistry was compared to another etch, featuring Cl_2 chemistry. The etch profiles are compared in Figure A.2. Both samples were etched to a depth of approximately 190 nm. The Cl_2-based etch shows evidence of micro-trenching at the sidewall, visible in Figure A.2c, whereas the $C_4F_8/SF_6/CF_4$ etch shown in Figure A.2a does not. The surface of the sidewall in the $C_4F_8/SF_6/CF_4$ etch, shown in Figure A.2b, appears to feature small bumps, while the sidewall of the Cl_2 etch in Figure A.2d seems smoother. Nonetheless, both etch chemistries resulted in identical waveguide propagation loss.

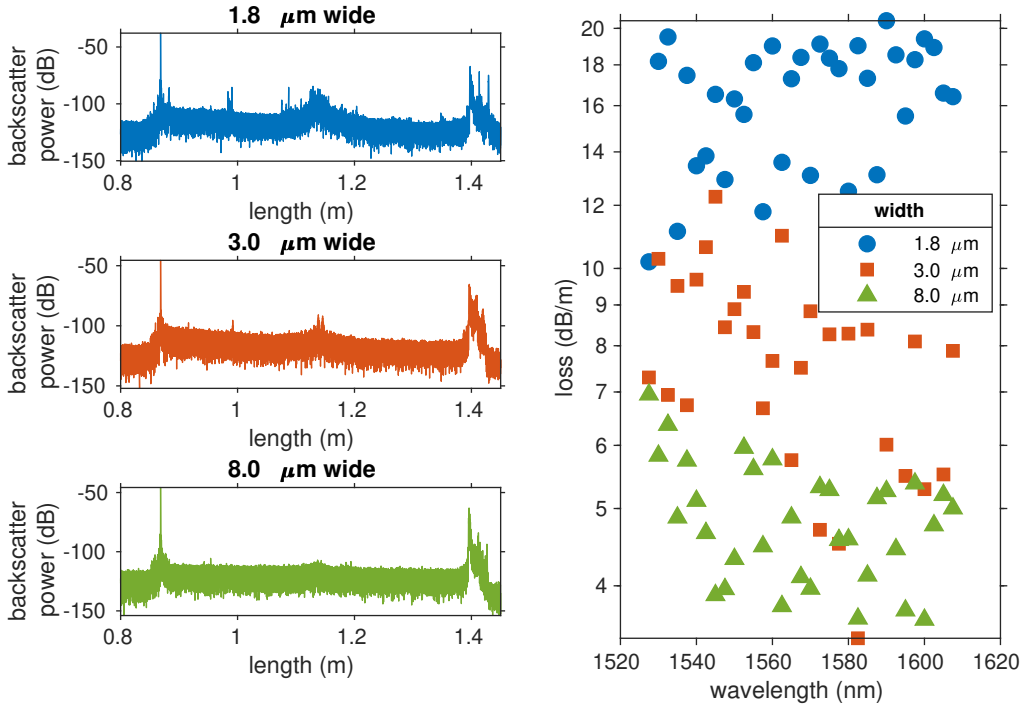

Figure A.3: **Optical frequency domain reflectometry (OFDR) loss analysis of silicon-on-insulator waveguides.** The left panels show the raw OFDR traces used to extract propagation loss. The right panel shows the extraced loss from each trace, as a function of wavelength. The propagation loss decreases for increasing waveguide width, as would be expected for propagation loss limited by scattering loss from the waveguide sidewall roughness.

The propagation loss measurement of waveguides patterned using the Cl_2-based etch is presented in Figure A.3, for selected partially-etched waveguide widths, with device

layer thickness of 500 nm, and an etch depth of 180 nm. All of the waveguide geometries considered support multiple transverse modes. The loss was extracted using optical frequency domain reflectometry [4] to fit a linear model to the waveguide backscatter. Excess scattering is observed at the center of the waveguide in the left panels of Figure A.3, and is attributed to an un-optimized s-bend at the center of the spiraled waveguide, causing coupling to higher-order modes and excess sidewall scattering due to the reduced bending radius within the s-bend. The center part of each trace is excluded from the linear fit. The resultant loss for the three widths of waveguide is plotted as a function of wavelength in the right panel of Figure A.3. Notably, though the etch depth of 180 nm is more than three times the 56 nm etch depth used in [1], the loss is almost identical, with as low as 4 dB/m to 5 dB/m measured in the 8 µm waveguide. The lithographic pattern used in this experiment was also identical to that used in [1]. Thus, realizing an equivalent loss in spite of a significantly greater etch depth illustrates the improvement in sidewall roughness achieved with this improved process. If this experiment had been repeated with 56 nm etch depth, a propagation loss below 2 dB/m may be feasible.

If such low waveguide loss could be realized, large-mode volume, spiraled resonators similar to those demonstrated in Chapter 4, might be realized within a silicon-on-insulator platform, enabling both the suppression of thermo-refractive noise and two-photon absorption. Such devices could be used to overcome the performance limitations of recent III-V on silicon heterogeneous-integrated lasers [3, 2], and simultaneously achieve a high power and ultra-narrow linewidth laser source on a single chip.

A.2 Flexural waveguide acousto-optic modulator

In this section, the concept and design for a silicon-photonic acousto-optic modulator are presented. The device is based on the suspended, PZT-on-silicon waveguide platform

initially proposed in Chapter 8. A silicon device layer, with the underlying buried oxide (BOX) removed, forms a suspended membrane. For acoustic waves, free surfaces form perfectly reflecting boundaries, such that suspended membranes may form acoustic slab waveguides, analogously to how total-internal reflection between two optical interface can form an optical slab waveguide. Such acoustic slab modes are known as Lamb waves. Here, a structure is proposed provide lateral acoustic confinement to a specific class of Lamb wave, known as a flexure wave, and in such a way that the acoustic mode may be driven electrically. The same structure may also be engineered to accommodate an optical waveguide, such that acoustic and optical modes co-propagate to form an efficient acousto-optic modulator.

To understand how lateral confinement of a Lamb mode may be achieved, the general dispersion relation of Lamb waves may be understood using the Rayleigh-Lamb equations [5]. These equations are solved, and the dispersion relations for the lowest-few order Lamb modes are plotted in Figure A.4a for a 1 µm thickness silicon dioxide membrane. The lowest order antisymmetric mode is notable for having a lower phase velocity than both the bulk longitudinal wave velocity, V_l, and the bulk shear wave velocity, V_s. For sufficiently large propagation constant, β, the lowest order symmetric and antisymmetric modes asymptotically approach the same phase velocity, which is lower than the bulk shear wave velocity, V_s. In this regime, these modes are localized to the surfaces of the slab, and are known as Rayleigh waves. Conversely, at low propagation constant, the lowest order antisymmetric mode is strongly dispersive, and in this regime is known as a flexural wave.

In Figure A.4b, the dispersion of the lowest-order Lamb wave is compared for a 1 µm and 2 µm slab. For any given frequency, ω, the 1 µm slab exhibits a higher propagation constant, that is, lower phase velocity, than then 2 µm slab. This suggests that if a 1 µm slab were bordered by 2 µm slabs, this lowest-order mode might be guided within the

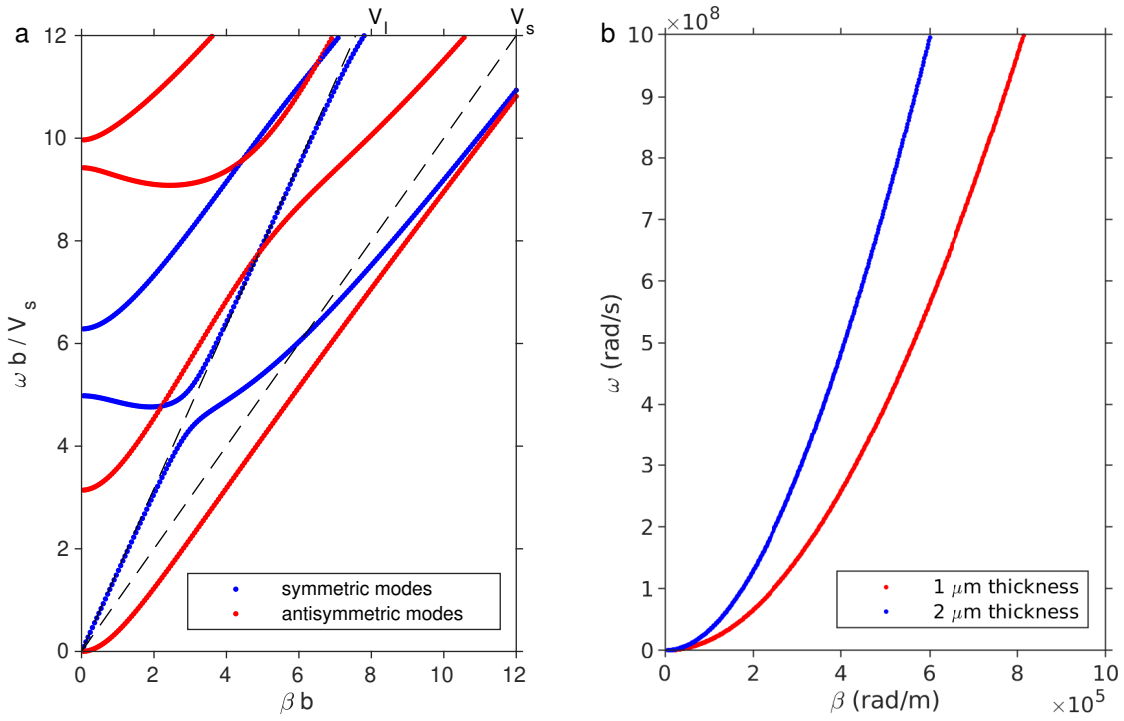

Figure A.4: **Lamb wave dispersion.** (a) Dispersion diagram for lamb wave acoustic modes in a 1 µm thickness silicon dioxide slab, having normalized the propagation constant and frequency to the slab thickness, b, and acoustic shear wave velocity, V_s. The (anti)symmetric modes are plotted in (blue) red, while the dispersion of bulk acoustic waves with longitudinal (V_l) and shear (V_s) displacement are plotted with dashed lines, for comparison. (b) Comparison of the lowest-order Lamb wave dispersion for 1 µm and 2 µm thickness silicon dioxide slabs. The propagation constant is higher in the thinner slab for any given frequency, which enables an acoustic wave to be guided within a thinner membrane bordered by thicker membranes.

1 µm slab, and decay evanescently in the adjacent, thicker slab. Such guided flexure waves are shown in Figure A.5a,b.

If Figure A.5, the simulated structure consists of a 1 µm PZT-on-Pt actuator, deposited on a silicon dioxide on silicon layer. The PZT membrane is then removed at the center of the structure, and the remaining thinner layer, consisting of a silicon dioxide/silicon bimorph, forms the center of the flexural waveguide. Prior to any PZT deposition, the silicon dioxide/silicon membrane itself would be formed by etching a 500 nm silicon-on-insulator device layer to form a silicon optical rib waveguide. A silicon dioxide layer would be deposited on the silicon, and planarized by chemical-mechanical polishing prior to PZT actuator deposition. The silicon waveguide core would be positioned at the central node of the antisymmetric, higher order flexure wave shown in Figure A.5b.

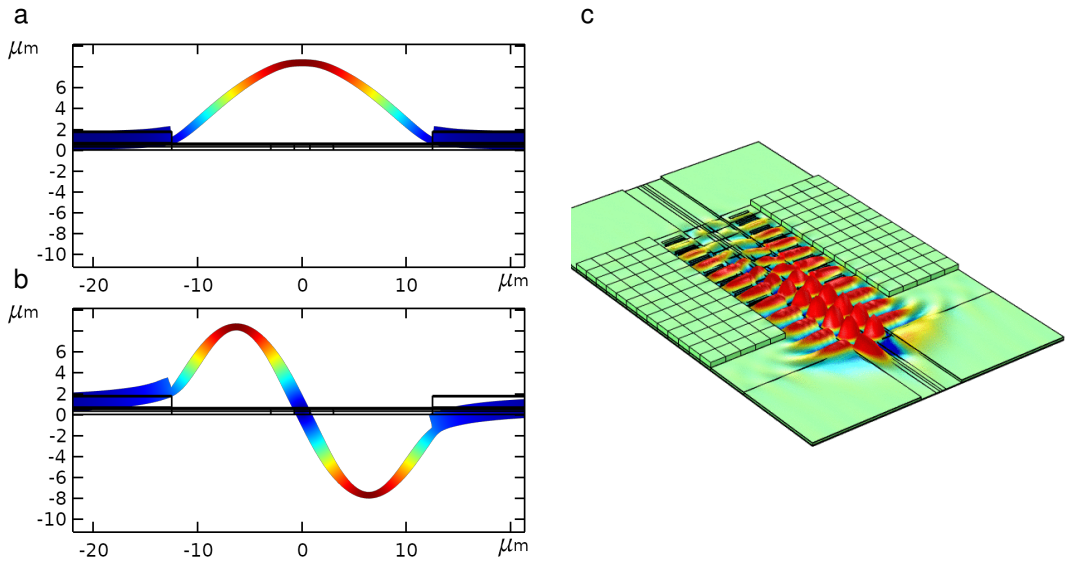

Figure A.5: **Guided flexure wave.** (a) Simulated lowest order guided flexure wave with 11 µm wavelength, and (b) first higher-order mode flexure wave with 12 µm wavelength, at 88 MHz frequency. Total displacement is indicated by the color. (c) Three-dimensional simulation of electrical excitation of the flexural wave by means of electrodes placed on the PZT surface. The vertical displacement is indicated by the color.

In order to achieve acousto-optic modulation, the acoustic propagation vector should

be selected to match the propagation vector difference between the fundamental TE and TM mode in the optical waveguide [6]. In this case, an acoustic wave with a wavelength of approximately 12 µm and frequency around 88 MHz is capable of matching the propagation vectors. The antisymmetric flexural wave, shown in Figure A.5b, effectively rotates the waveguide core, and is predicted to provide a modulation index of unity for single mm-scale modulation lengths and single nm-scale peak displacement, accounting for both stress-optic coupling and moving boundary effects [7]. Under operation, such a device would rotate the polarization between TE and TM, while simultaneously providing either a positive or negative 88 MHz frequency shift, depending on whether the optical and acoustic waves were co-propagating or counter-propagating. To excite the antisymmetric flexural wave, electrodes may be placed at quarter-wave intervals on the PZT film, within the evanescent tails of the flexural wave, enabling the acoustic wave to be driven along the full length of the acousto-optic interaction region. In Figure A.5c, a fully three-dimensional frequency-domain simulation demonstrates that the desired acoustic wave may be efficiently excited by this technique. In this simulation, an additional silicon dioxide layer has been deposited onto the PZT film outside the extent of the driving electrodes. This additional layer provides stronger confinement of the acoustic energy to the acousto-optic region, and in a physical device would also accommodate electrical routing to the electrodes.

Bibliography

[1] M. A. Tran, D. Huang, T. Komljenovic, J. Peters, A. Malik, and J. E. Bowers, *Ultra-low-loss silicon waveguides for heterogeneously integrated silicon/III-V photonics*, *Applied Sciences* **8** (2018), no. 7 1139.

[2] D. Huang, M. A. Tran, J. Guo, J. Peters, T. Komljenovic, A. Malik, P. A. Morton,

and J. E. Bowers, *High-power sub-kHz linewidth lasers fully integrated on silicon*, *Optica* **6** (2019), no. 6 745–752.

[3] M. A. Tran, D. Huang, and J. E. Bowers, *Tutorial on narrow linewidth tunable semiconductor lasers using Si/III-V heterogeneous integration*, *APL photonics* **4** (2019), no. 11 111101.

[4] B. J. Soller, D. K. Gifford, M. S. Wolfe, and M. E. Froggatt, *High resolution optical frequency domain reflectometry for characterization of components and assemblies*, *Optics express* **13** (2005), no. 2 666–674.

[5] B. A. Auld, *Acoustic fields and waves in solids*. 1973.

[6] B. J. Eggleton, C. G. Poulton, P. T. Rakich, M. J. Steel, and G. Bahl, *Brillouin integrated photonics*, *Nature Photonics* **13** (2019), no. 10 664–677.

[7] S. G. Johnson, M. Ibanescu, M. Skorobogatiy, O. Weisberg, J. Joannopoulos, and Y. Fink, *Perturbation theory for maxwell's equations with shifting material boundaries*, *Physical review E* **65** (2002), no. 6 066611.